A Contribution to the Computation of the Impedance in Acceleration Resonators

Ein Beitrag zur Berechnung der Impedanz in Beschleunigungsresonatoren
Zur Erlangung des akademischen Grades Doktor-Ingenieur (Dr.-Ing.)
genehmigte Dissertation von Dipl.-Ing. Cong Liu aus Shanghai, China
Mai 2016 — Darmstadt — D 17

TECHNISCHE
UNIVERSITÄT
DARMSTADT

Fachbereich Elektrotechnik und Informationstechnik
Institut für Theorie Elektromagnetischer Felder (TEMF)

A Contribution to the Computation of the Impedance in Acceleration Resonators
Ein Beitrag zur Berechnung der Impedanz in Beschleunigungsresonatoren

Genehmigte Dissertation von Dipl.-Ing. Cong Liu aus Shanghai, China

1. Gutachten: Prof. Dr.-Ing. Thomas Weiland
2. Gutachten: Prof. Dr.-Ing. Harald Klingbeil

Tag der Einreichung: 09. Februar 2016
Tag der Prüfung: 25. April 2016

Darmstadt — D 17

Bitte zitieren Sie dieses Dokument als:
URN: urn:nbn:de:tuda-tuprints-54510
URL: http://tuprints.ulb.tu-darmstadt.de/5451

Kurzfassung

Der Schwerpunkt dieser Arbeit liegt auf der numerischen Berechnung der Impedanzen von Beschleunigern (supraleitende Kavitäten) sowie Beschleunigerkomponenten. Zu diesem Zweck wurde zunächst ein geeigneter Löser auf Grundlage der Finiten Elemente Methode (FEM) entwickelt, um die breitbandigen Impedanzen von Beschleunigerkomponenten zu berechnen. Zusätzlich wurden unterschiedliche numerische Ansätze zur Berechnung der schmalbandigen Impedanzen für supraleitende Hochfrequenzkavitäten (HF-Kavitäten) verfolgt. Davon wurde ein Überblick zu berechneten Ergebnissen gegeben und ein Vergleich zwischen den unterschiedlichen Ansätzen durchgeführt.

Während der Konstruktion der supraleitenden HF-Kavitäten und Beschleunigerkomponenten ist eine herausfordernde und schwierige Aufgabe die Bestimmung der Impedanzen für die Beschleunigungsstrukturen mit Hilfe geeigneter Computersimulationen. Die Impedanz beschreibt die elektromagnetische Wechselwirkung zwischen dem Teilchenstrahl und den Beschleunigungsstrukturen. Sie kann die Intensität der Teilchenstrahlen beeinträchtigen. Für eine supraleitende HF-Kavität mit Wellenleiter (Strahlrohre und Koppler) entspricht die schmalbandige Impedanz den Eigenmoden der Kavität. Die schmalbandige Impedanz, die auch Shuntimpedanz genannt wird, ist abhängig von der Eigenfrequenz und Verteilung der elektromagnetischen Felder der Eigenmoden. Andererseits kann die breitbandige Impedanz als Maß für den Grad der Wechselwirkung des Wellenleiters mit dem Teilchenstrahl bei einer beliebigen Frequenz und Geschwindigkeit des Strahls herangezogen werden. Von der breitbandigen- und schmalbandigen Impedanz können detaillierte Kenntnisse der Impedanz für die Beschleunigungsstrukturen bekannt gegeben werden.

Zur Berechnung der breitbandigen longitudinalen Raumladungsimpedanz wurde ein Löser zur Berechnung dreidimensionaler elektromagnetischer Felder auf Grundlage der FEM im Frequenzbereich entwickelt.

Zur Berechnung der schmalbandigen Impedanz für supraleitende HF-Kavitäten verfolgen wir unterschiedliche Ansätze. Zunächst wurde eine Eigenmodenanalyse basierend auf Finite Integration Technique (FIT) und ein paralleler, reellwertiger FEM Eigenwertlöser basierend auf symmetrischen, gekrümmten Tetraeder-Elementen für eine supraleitende Proton Linac (SPL) Kavität eingesetzt. Danach wurde ein paralleler, komplexwertiger FEM Eigenwertlöser basierend auf gekrümmten Tetraeder-Elementen für die TESLA 1,3 GHz Beschleunigungskavität

und die dritte harmonische supraleitende 3,9 GHz Beschleunigungskavität angewandt.

Abstract

This thesis is focusing on the numerical computation of the impedance in acceleration resonators and corresponding components. For this purpose, a dedicated solver based on the Finite Element Method (FEM) has been developed to compute the broadband impedance in accelerating components. In addition, various numerical approaches have been used to calculate the narrow-band impedance in superconducting radio frequency (RF) cavities. From that an overview of the calculated results as well as the comparisons between the applied numerical approaches is provided.

During the design phase of superconducting RF accelerating cavities and components, a challenging and difficult task is the determination of the impedance inside the accelerators with the help of proper computer simulations. Impedance describes the electromagnetic interaction between the particle beam and the accelerators. It can affect the stability of the particle beam. For a superconducting RF accelerating cavity with waveguides (beam pipes and couplers), the narrow-band impedance, which is also called shunt impedance, corresponds to the eigenmodes of the cavity. It depends on the eigenfrequencies and its electromagnetic field distribution of the eigenmodes inside the cavity. On the other hand, the broadband impedance describes the interaction of the particle beam in the waveguides with its environment at arbitrary frequency and beam velocity. With the narrow-band and broadband impedance the detailed knowledges of the impedance for the accelerators can be given completely.

In order to calculate the broadband longitudinal space charge impedance for acceleration components, a three-dimensional (3D) solver based on the FEM in frequency domain has been developed.

To calculate the narrow-band impedance for superconducting RF cavities, we used various numerical approaches. Firstly, the eigenmode solver based on Finite Integration Technique (FIT) and a parallel real-valued FEM (CEM3Dr) eigenmode solver based on symmetric curvilinear tetrahedrons are applied to the Superconducting Proton Linac (SPL) cavity. Afterwards, a parallel complex-valued FEM (CEM3Dc) eigenmode solver based on curvilinear tetrahedrons is applied to the TESLA 1.3 GHz and the third harmonic 3.9 GHz superconducting cavities.

Contents

1 Introduction

1.1 Motivation

It is well-known that particle accelerators can provide various opportunities for the fundamental research in a variety of fields, such as nuclear, atomic, anti-matter and plasma physics as well as biology and bio-medical science. Numerical simulation techniques are nowadays the powerful tools to support the development and design of particle accelerators. They cannot only ease the design and testing process during the design phase but provide also the detailed information that cannot be obtained by measurements. Therefore, numerical simulation techniques ensure a successful and economic operation of the particle accelerators. A typical accelerating resonator is called radio frequency (RF) cavity, it retrains electromagnetic fields in the microwave region of the spectrum [1]. Obtaining the knowledges of the eigenmodes, which are excited when the particle beam is transversing a RF cavity, is a very important and essential job because the higher-order eigenmodes can lead to particle beam instabilities. For this purpose, the highly precise eigenfrequencies as well as the electromagnetic field distribution of the eigenmodes are required to compute the shunt impedance (narrow-band impedance) of the eigenmodes properly. In this thesis, we applied various numerical approaches to calculate the eigenfrequencies and the corresponding shunt impedance of the eigenmodes for different acceleration resonators.

Additionally, the broadband impedance, which describes the electromagnetic interaction between the particle beam and the accelerating components (e.g. beam pipes and couplers) at a very wide frequency range, also have to be researched carefully. For this purpose, a dedicated solver based on the Finite Element Method (FEM) has been developed for the computation of the longitudinal space charge low frequencies impedances.

1.1.1 Superconducting Proton Linac (SPL) Cavity

The Superconducting Proton Linac (SPL) cavity [2] operating at 704.4 MHz is mainly designed and conducted by CERN (European Organization for Nuclear Research) for increasing the interest of high average current electron and high intensity proton beams. It is a part of the planned injector upgrade of the Large Hadron Collider (LHC) comprising of two families: $\beta = 0.65$ and $\beta = 1$, where β represents the relativistic velocity. The SPL cavity is used to accelerate the ion beam from 160 MeV to 5 GeV and serves as a driver for neutrino facilities and radioactive beam facilities. It is made of a five-cell resonator with beam pipes as well as an input coupler (see Fig. 5.1), which is used to feed the RF electric fields for accelerating the particle beam. Moreover, the higher-order modes (HOM) couplers must be taken into account during the design phase. But during my research of the SPL cavity, the precise layout of the HOM couplers was still under study and not yet known. For this reason, the HOM couplers are neglected in this thesis. In this thesis, the eigenmodes as well as their characteristic values are calculated with various numerical approaches to give an overview of the influence of the higher-order modes in the SPL cavity.

1.1.2 TESLA 1.3 GHz Accelerating Cavity

The TESLA 1.3 GHz accelerating cavity [3] is applied as part of the linear electron-positron collider and is based on a nine-cell superconducting niobium cavity (see Fig. 1.1) with a designed accelerating gradient of $\mathbf{E}_{acc} \geq 25$ MV/m at a designed quality factor $Q \geq 5 \cdot 10^9$. The fundamental mode $TM_{010,}, \pi$ is a 1.3 GHz mode, which is applied to the acceleration of the particle beam. In this thesis, each TESLA 1.3 GHz nine-cell cavity is equipped with a coaxial RF input coupler, which transfers energy from the radio frequency source to the particle beam, and two HOM couplers, which are installed to effectively suppress parasitic modes. Under consideration of the energy transfer in such dissipative superconducting cavities, a complex-valued eigenmode solver is applied to determine the characteristic values of the eigenmodes in this thesis.

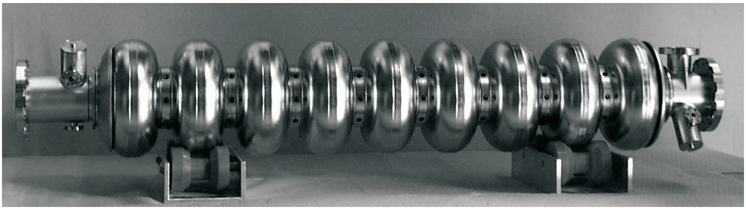

Figure 1.1: A TESLA superconducting 1.3 GHz nine-cell cavity [3].

1.1.3 The third harmonic 3.9 GHz Superconducting Cavity

At DESY the free electron laser FLASH [4] [5] [6] uses ultra-short electron bunches to generate high brilliance coherent light pulses. It is designed and developed for photon science and various particle physics studies. For the design of the FLASH 3rd harmonic section (ACC39), the third harmonic 3.9 GHz superconducting cavity is used to linearize the longitudinal phase-space properties for the bunch compression and is operating at 3.9 GHz. It has a similar geometry as the 1.3 GHz TESLA cavity and is composed of a nine-cell resonator with beam pipes as well as an input coupler. In addition, two HOM couplers are installed on each side of the connecting beam pipes. In this thesis, we use a complex-valued eigenmode solver to determine the characteristic values of the eigenmodes for the third harmonic superconducting cavity.

1.2 Numerical Methods

Due to the fact that the analytical solution of the electromagnetic problems from accelerating physics are not available, we can find the approximate numerical solution by using either the Finite Integration Technique (FIT) [7] or the Finite Element Method (FEM) [8]. The both methods are frequently used numerical techniques for large scale computations in accelerating resonators and components.

The FIT, which will be introduced in section 3.1, can be applied for solving the electromagnetic problem in time and frequency domain. The eigenvalue problem can be solved in frequency domain by using the eigenmode solver contained in CST Microwave Studio® [9] with the hexahedral discretization mesh. On the other hand, the FEM, introduced in section 3.2, can be also applied to the eigenvalue problem. At the Institut für Theorie Elektromagnetischer Felder (TEMF) , eigenmode solvers based on real- and complex-valued FEM analysis are available. Both eigenmode solvers use tetrahedral grids and higher-order curvilinear elements to increase the demand for high precision modeling of the elliptical acceleration structures. Meanwhile, both eigenmode solvers use a high degree of parallelization provided with a distributed memory architecture using Message Passing Interface (MPI) parallelization strategy, so that the field simulation can be dramatically accelerated. Moreover, the complex-valued eigenmode solver (CEM3Dc) considers the energy transfer between the acceleration resonator and its components, e.g. input, HOM couplers and beam pipes. This approach uses one computation for each individual eigenmode. Therefore, the robust parallel complex-valued eigenmode solver can be applied for solving the eigenvalue problems properly. Additionally, in this thesis a dedicated solver based on FEM has been developed to calculate the broadband impedance for the accelerating components in frequency domain.

1.3 Overview

The thesis is structured as follows:

Firstly, some fundamental concepts of the classical electrodynamics and particle accelerators will briefly be presented in chapter 2. That chapter focuses on the continuous Maxwell's equations as well as the concepts of the wake fields and impedances for particle accelerators.

Afterwards, the spatial discretization of Maxwell's equations by using the FIT and FEM will be introduced in chapter 3.

In chapter 4, an approach to compute the broadband impedance in accelerating components will be reviewed. The approach is based on a finite element formulation of the electromagnetic problem. There, the mathematical modeling of the Maxwell's equations as well as the proper formulation of the boundary conditions will be described. After that, the implementation details for this method will be summarized. Lastly, a benchmark example will be presented.

Chapter 5 investigates the computation of the narrow-band impedances for accelerating resonators. There, the field simulation in a lossless SPL cavity is carried out with perfect electric boundary conditions by using the FIT and FEM. After that, the field simulation for the lossy TESLA 1.3 GHz accelerating cavity and the lossy third harmonic 3.9 GHz superconducting cavity is performed with a port boundary condition by using the complex-valued FEM eigenmode solver. Moreover, some post-processing work will be demonstrated. Additionally, in order to verify and validate the obtained numerical results, the comparisons of the results from diverse eigenmode solvers will be given.

Finally, the thesis is closed with a summary and an outlook in chapter 6.

2 Continuous Electrodynamic

In the first two parts of this chapter, the Maxwell's equations and the constitutive equations are introduced. Then we introduce the concepts of wake fields and impedances because they are one of the main factors which can affect the stability of the particle beam.

2.1 Maxwell's Equations

The Maxwell's equations form the foundation of the classical electromagnetic phenomena [10]. They are published by the Scottish physicist and mathematician James Clerk Maxwell. The Maxwell's equations in differential form are given by:

$$\begin{aligned}
\nabla \times \mathbf{E}(\mathbf{r},t) &= -\frac{\partial \mathbf{B}}{\partial t}(\mathbf{r},t) && (2.1)\\
\nabla \times \mathbf{H}(\mathbf{r},t) &= \frac{\partial \mathbf{D}}{\partial t}(\mathbf{r},t) + \mathbf{J}(\mathbf{r},t) && (2.2)\\
\nabla \cdot \mathbf{D}(\mathbf{r},t) &= \rho(\mathbf{r},t) && (2.3)\\
\nabla \cdot \mathbf{B}(\mathbf{r},t) = 0 & && (2.4)
\end{aligned}$$

where **E** represents the electric field strength, **H** magnetic field strength, **D** electric displacement flux density. The magnetic flux density is denoted by **B**, the electric current density by **J**, the electric charge density by ρ. The vector **r** denotes the spatial parameter and scalar t the time dependency. The electric current density **J** consists of a conductive part $\mathbf{J}_\kappa$, a convective part $\mathbf{J}_c$ and the impressed current density $\mathbf{J}_i$ [11]. The equations (2.1) and (2.2), known as Faraday's law and Ampere's law, respectively, describe the interactions between the electric and magnetic field. The other two equations (2.3) and (2.4) are called Gauss's law and Gauss's law of magnetic flux density.

The Maxwell's equations in integral form for non-moving media can be expressed with [12]

$$\int_{\partial A} \mathbf{E}(\mathbf{r},t)\cdot d\mathbf{s} = -\int_{A} \frac{\partial \mathbf{B}(\mathbf{r},t)}{\partial t}\cdot d\mathbf{A} \qquad \forall A \subset \mathbb{R}^3, \tag{2.5}$$

$$\int_{\partial A} \mathbf{H}(\mathbf{r},t)\cdot d\mathbf{s} = \int_{A} \left(\frac{\partial \mathbf{D}(\mathbf{r},t)}{\partial t} + \mathbf{J}(\mathbf{r},t)\right)\cdot d\mathbf{A} \qquad \forall A \subset \mathbb{R}^3, \tag{2.6}$$

$$\int_{\partial V} \mathbf{D}(\mathbf{r},t)\cdot d\mathbf{A} = \int_{V} \rho(\mathbf{r},t)dV \qquad \forall V \subseteq \mathbb{R}^3, \tag{2.7}$$

$$\int_{\partial V} \mathbf{B}(\mathbf{r},t)\cdot d\mathbf{A} = 0 \qquad \forall V \subseteq \mathbb{R}^3. \tag{2.8}$$

In order to solve the Maxwell's equations properly, the knowledge of the electromagnetic field at the material interfaces is required. The boundary conditions at the interface between the medium 1 and medium 2 read:

$$\mathbf{n}\times(\mathbf{E}_2-\mathbf{E}_1) = 0 \tag{2.9}$$

$$\mathbf{n}\cdot(\mathbf{D}_2-\mathbf{D}_1) = \sigma \tag{2.10}$$

$$\mathbf{n}\times(\mathbf{H}_2-\mathbf{H}_1) = \mathbf{J}_F \tag{2.11}$$

$$\mathbf{n}\cdot(\mathbf{B}_2-\mathbf{B}_1) = 0 \tag{2.12}$$

where $\mathbf{n}$ is the unit vector normal to the interface, σ the surface charge density and $\mathbf{J}_F$ the surface current density. The equations (2.9) and (2.12) state that the tangential electric field and the normal component of the magnetic flux density is always continuous at the interface, while the equation (2.10) shows that the normal component of the electric flux density is not continuous if there are surface charges at the interface. Analogously, the equation (2.11) states that the tangential magnetic field strength is discontinuous in case that the surface current density is not zero at the interface.

In addition, the constitutive equations connect the electromagnetic fields and fluxes. In the case of the linear, frequency-independent, isotropic, non-dispersive and non-permanent materials, the constitutive equations are given by

$$\mathbf{D} = \epsilon\mathbf{E} = \epsilon_0\epsilon_r\mathbf{E} \tag{2.13}$$

$$\mathbf{B} = \mu\mathbf{H} = \mu_0\mu_r\mathbf{H} \tag{2.14}$$

$$\mathbf{J}_\kappa = \kappa\mathbf{E} \tag{2.15}$$

where ϵ, μ, ϵ_r and μ_r state the permittivity, permeability, relative permittivity and relative permeability of the material, respectively. The constants $\epsilon_0 = 8.854187 \cdot 10^{-12}$ As/Vm and $\mu_0 = 4\pi \cdot 10^{-7}$ Vs/Am are the permittivity and permeability of vacuum, respectively. The equation (2.15) is known as Ohm's law, which describes the relationship between the conductive current density $\mathbf{J}_\kappa$ and the electric field strength $\mathbf{E}$, where κ denotes the electric conductivity.

2.2 Wake Fields and Wake Potential

Assuming that, if a point-like charge q is moving in free space at a velocity $\boldsymbol{v}$ close to the speed of light c_0, it will excite scattered electromagnetic fields [13]. Because of the Lorentz contraction, the excited field distribution looks like a thin disk (see Fig. 2.1a) [14], which is vertical to the direction of motion and has an opening angle $1/\gamma$, where γ is known as Lorentz factor and can be given by

$$\gamma = \frac{1}{\sqrt{1-\beta^2}} \quad \text{with } \beta = \frac{\boldsymbol{v}}{c_0} \tag{2.16}$$

where β is the relativistic velocity [14].

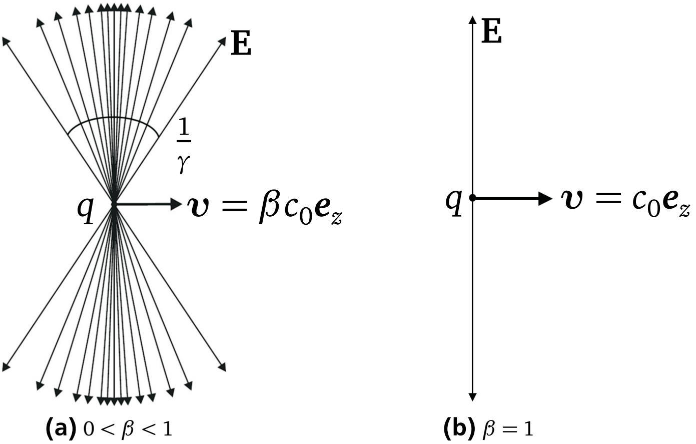

(a) $0 < \beta < 1$ **(b)** $\beta = 1$

Figure 2.1: The electric field $\mathbf{E}$ of a point-like electric charge (a) in relativistic motion, and (b) in the ultra-relativistic limit.[14].

In the limit case of $\beta \rightarrow 1$, the electromagnetic field of a point-like charge can be given by:

$$E_r = \frac{q}{2\pi\epsilon_0 r}\delta(z - c_0 t); \;\; H_\varphi = \frac{qc_0}{2\pi r}\delta(z - c_0 t) \tag{2.17}$$

where $\delta(z-c_0t)$ represents a δ function distribution. The electric field distribution is shown in Fig. 2.1b. The equation (2.16) together with Fig. 2.1b shows that the electric field **E** of a point charge is restricted to a plane perpendicular to the direction of motion at the position z=c_0t. The electromagnetic fields are zero ahead and behind the charge. If there is a test charge either preceding or following the point charge q, there is no interactions between both charges [13]. But if the charge q_1 is moving with speed c_0 through a cavity with beam pipes (see Fig. 2.2), the electromagnetic fields will appear behind the point charge [15]. These electromagnetic fields are known as wake fields and have an influence on the test charge q_2.

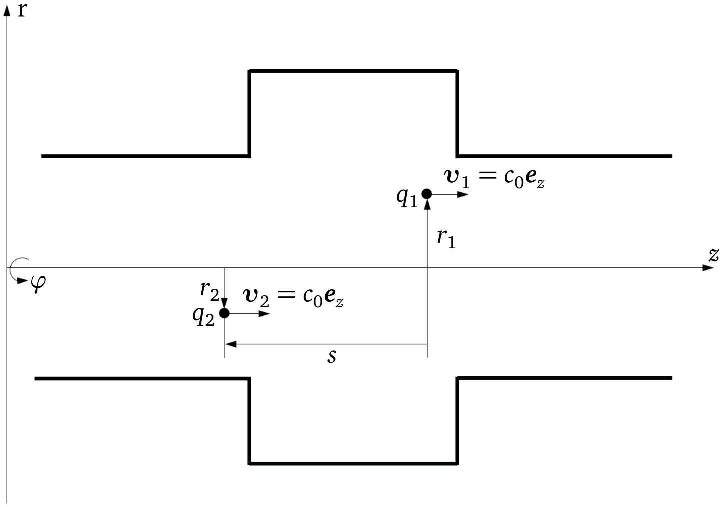

Figure 2.2: Two point charges traversing a cavity. q_1 with an offset r_1 is followed by a test charge q_2 with an offset r_2 at a distance s.

Considering the example in Fig. 2.2, the test charge q_2 is following the point charge q_1 at a distance s. Both charges are traversing the cavity with the speed of the light c_0. The total electromagnetic force on the test charge q_2 is known as Lorentz force and can be given by Lorentz force equation [16]

$$\mathbf{F} = q_2(\mathbf{E} + \boldsymbol{v}_2 \times \mathbf{B}) \tag{2.18}$$

where the electric fields **E** and magnetic fields **B** are excited by the point charge q_1. Let us now consider a particle bunch with total charge q_1 transversing the cavity, the wake potential $\boldsymbol{W}$ is defined by [17]

$$\boldsymbol{W}(r_1, s) = \frac{1}{q_1}\int_{-\infty}^{\infty}(\mathbf{E}(r_1, z, t) + \boldsymbol{v}_1 \times \mathbf{B}(r_1, z, t))dz \tag{2.19}$$

$$t = \frac{s + z}{c_0} \tag{2.20}$$

where the distance s must be positive in the opposite direction of $\boldsymbol{v}_1$ due to the principle of causality [18]. Since the vector $c_0\boldsymbol{e}_z \times \mathbf{B}$ is always perpendicular to the longitudinal coordinate z, the wake potential $\boldsymbol{W}(s)$ can be decomposed into two components: the longitudinal wake potential

$$W_{||}(r_1, s) = \frac{1}{q_1}\int_{-\infty}^{\infty}\mathbf{E}_z(r_1, z, (s+z)/c_0)dz \tag{2.21}$$

and the transverse wake potential [19]. We can use equation (2.21) to calculate the longitudinal wake potential. By applying the Panofsky-Wenzel theorem [13] [20] [21]

$$\frac{\partial}{\partial s}\boldsymbol{W}_{\perp}(r, s) = -\nabla_{\perp}W_{||}(r, s) \tag{2.22}$$

the transverse wake potential can be obtained by integrating the traverse gradient of the longitudinal wake potential

$$\boldsymbol{W}_{\perp}(r, s) = -\nabla_{\perp}\int_{-\infty}^{s}W_{||}(r, s')ds'. \tag{2.23}$$

2.3 Impedances

As stated in section 2.2, the wake potential characterizes the interaction of the particle beam and its surrounding environment in time domain. The description of such an interaction in frequency domain can be called the impedance or coupling impedance [22] [23]. It can given by the Fourier transform of the wake potential

$$Z(r,\ \omega) = \frac{1}{c_0}\int_{-\infty}^{\infty} W(r,\ s) e^{-j\frac{\omega s}{c_0}} ds. \tag{2.24}$$

The impedance is one of the main factors which can affect the stability of the particle beam. It can be separated into the longitudinal and transverse parts. For the resonant cavity with beam pipes, the indication of the usefulness for the impedance is that it often involves a number of sharply defined frequencies [22] or a broad and smooth spectrum [24]. The sharply defined frequencies below the cut-off frequency of the beam pipe correspond to the eigenmodes of the cavity, because the corresponding long range wake fields are trapped by the cavity after the particle beam has left, the corresponding impedance dominates the impedance for the cavity and is called narrow-band impedance or shunt impedance. On the other hand, above the cut-off frequency of the beam pipe the short range wake fields can escape from the cavity and spread in the beam pipe. In addition, the wake fields can be generated by a particle beam traversing the beam pipe with velocity v. The corresponding impedance forms a broad and smooth spectrum and is called broadband impedance [25]. The electromagnetic interaction of a particle beam in the accelerator with its environment can be described by the narrow- and broadband impedances completely. For this reason, impedances should be studied properly during the design phase of accelerating resonators and components. The numerical approaches to determine the narrow-band and broadband impedance will be introduced in detail in the next chapters.

2.3.1 Broadband Impedance

The broadband impedance describes the coupling interaction between the particle beam and the accelerating components. It can be separated into the longitudinal and transverse parts. In this thesis, the transverse broadband impedance will not be discussed and studied. As stated in [26] and [27], there are two important kinds of longitudinal coupling impedances: the space charge and the resistive wall impedances. Since we consider only perfectly conductive structures in this thesis, the resistive wall impedance from a structure with finite conductivity, which is related to the skin depth on the conducting structure [28], will not be taken into account. The space charge impedance is purely imaginary and its definition will be given in chapter 4.

2.3.2 Loss Parameter

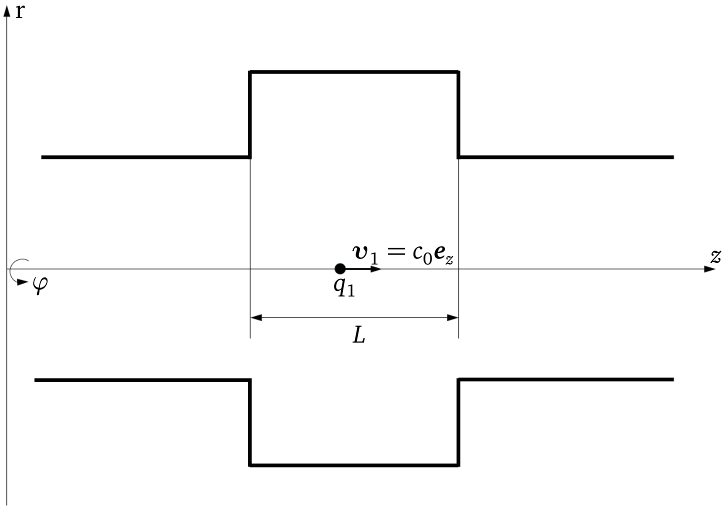

Figure 2.3: A point charge q_1 traversing a resonant cavity with length L.

In order to characterize the interaction between the particle beam and the cavity eigenmodes, we define the loss parameter. Considering a point charge traversing the cavity along the z-axis with the speed of light c_0 (see Fig. 2.3), the longitudinal complex voltage induced by the eigenmode n along the trajectory of the charge can be given by

$$V_{||} = \int_0^L \mathrm{Ez}_n(z) e^{j \frac{\omega_n z}{c_0}} dz \tag{2.25}$$

where L is the length of the cavity. The total energy stored in the eigenmode n, i.e. energy unit, is defined as

$$U_n = \frac{\epsilon_0}{2}\int_V |\mathbf{E}_n|^2 dV. \tag{2.26}$$

Now the loss parameter k_n of the mode n can be calculated by

$$k_n = \frac{|V_{||}|^2}{4U_n}. \tag{2.27}$$

Beside the loss parameter for the cavity eigenmode, there are other loss parameters, which describe the interaction of the particle beam and its environment, e.g. the loss into the beam pipe and parasitic loss [13]. For the design of a resonator cavity, we focus on the eigenmode effects, i.e. the loss to fundamental and higher oder modes in this thesis.

2.3.3 Quality Factor

Another important figure of merit for accelerating resonators is the quality factor Q, which describes the power dissipation of the cavity mode and is given by [17] [29] [30]

$$Q = 2\pi\frac{U_n}{\triangle U_n} = \frac{\omega_n U_n}{P} \tag{2.28}$$

where U_n is the stored energy, $\triangle U_n$ the dissipated energy per cycle, ω_n the angular frequency of the eigenmode n and P the total power loss. The power loss of eigenmode can be the wall loss due to the finite surface resistivity R_{sur} of the cavity walls. The total dissipated power P_s into the wall of the cavity can be given by a surface integral

$$P_s = \frac{1}{2}R_{surf}\int_{\partial V} |\mathbf{H}_\mathrm{t}|^2 \, dA \tag{2.29}$$

where $\mathbf{H}_\mathrm{t}$ is the tangential magnetic field to the cavity surface. For the superconducting cavity, the surface resistivity R_{surf} is composed of the BCS (Bardeen, Cooper, Schrieffer) term R_{BCS}, which depends on temperature and frequency. In addition, impurities, frozen-in magnetic flux or lattice distortions can cause the residual resistance R_{res} [31].

Another kind of the power loss of the eigenmode is the dissipated power into the external waveguides for acceleration resonators (e.g. input coupler, HOM couplers and beam pipes). The definition and description of the power loss P_{ext} will be given in chapter 5. Thus, we find for Q

$$Q = \frac{\omega_n U_n}{P} = \frac{\omega_n U_n}{P_s + P_{ext}} \tag{2.30}$$

$$\frac{1}{Q} = \frac{P_s + P_{ext}}{\omega_n U_n} = \frac{1}{Q_s} + \frac{1}{Q_{ext}}. \tag{2.31}$$

As stated before, in this thesis we focus only on perfectly conductive accelerating resonators and components. Therefore, the wall loss of the cavity P_s is vanishing. Thus, the equation (2.30) can be rewritten as

$$Q = \frac{\omega_n U_n}{P} = \frac{\omega_n U_n}{P_{ext}}. \tag{2.32}$$

2.3.4 Narrow-band Impedance

The third important quantity used to characterize the losses of the eigenmode in the cavity is the narrow-band impedance, which is also called shunt impedance R. The longitudinal shunt impedance of the monopole mode is defined by

$$R_{||} = \frac{4k_n Q}{\omega_n} = \frac{|V_{||}|^2 Q}{U_n \omega_n} = \frac{|V_{||}|^2}{P} \tag{2.33}$$

$$R_{||} = \frac{2k_n Q}{\omega_n} = \frac{1}{2}\frac{|V_{||}|^2 Q}{U_n \omega_n} = \frac{1}{2}\frac{|V_{||}|^2}{P} \tag{2.34}$$

where equation (2.33) is the US form and (2.34) the electrical English form [13]. In this thesis, the electrical English form (2.34) is applied for the computation of the shunt impedance. Both equations state that the narrow-band impedance has the same form as the description of the resistance in circuit theory and is dependent on the wall loss and external waveguides loss for the cavity with finite conductivity and waveguides. In addition, $R_{||}$ is dependent on the frequency of the eigenmode. Ideally, we want a large shunt impedance for the accelerating mode. On the other hand, a small shunt impedance for the higher-order modes (HOMs) is required so that the influences from the HOMs on the stability of particle beam is minimized.

Note that the normalized longitudinal narrow-band impedance can be given by [32]

$$\frac{R_{||}}{Q} = \frac{2k_n}{\omega_n} = \frac{1}{2}\frac{|V_{||}|^2}{U_n\omega_n} \tag{2.35}$$

which obviously depends on the frequency of the eigenmode. The eigenfrequency and the ratio $|V_{||}|^2/U$ scale inversely with linear dimensions of the cavity. Therefore, the normalized longitudinal shunt impedance $R_{||}/Q$ is independent of the cavity size, it depends only on the shape of the cavity [31]. Beside the longitudinal shunt impedance for the monopole mode, we define the transverse shunt impedance for the HOMs in the cavity. According to the Panofsky-Wenzel theorem, the transverse voltage can be calculated by the longitudinal voltage with offset r

$$V_{\perp}^{m} = \frac{\int_0^L \mathrm{Ez}_n(r,\ z)e^{j\frac{\omega_n z}{c_0}}\,dz}{r^{2m}} = \frac{V_L^{(m)}(r)}{r^{2m}} \tag{2.36}$$

where $m = 1, 2, 3$ refer to the dipole, quadrupole and sextuple modes, respectively. With the stored energy U_n, the transverse shunt impedance as well as the normalized transverse shunt impedance in electrical English form can be given:

$$R_{\perp} = \frac{1}{2}\frac{|V_{\perp}^{(m)}|^2}{U_n\omega_n}Q = \frac{1}{2}\frac{1}{r^{2m}}\frac{|V_L^{(m)}|^2}{U_n\omega_n}Q \tag{2.37}$$

$$\frac{R_{\perp}}{Q} = \frac{1}{2}\frac{|V_{\perp}^{(m)}|^2}{U_n\omega_n} = \frac{1}{2}\frac{1}{r^{2m}}\frac{|V_L^{(m)}|^2}{U_n\omega_n}. \tag{2.38}$$

The equations (2.34), (2.35), (2.37) and (2.38) are used to calculate the narrow-band impedances for the resonant cavity in this thesis. Theoretically, application of perfect electric conductive (PEC) boundary conditions on the waveguides of the perfectly conductive cavity leads to the vanishing power loss P and the infinite shunt impedance $R_{||}$ and $R_{\perp}$. For this reason, in section 5.1 we calculate the normalized shunt impedance $R_{||}/Q$ and $R_{\perp}/Q$ of the eigenmodes with (2.35) and (2.38). In section 5.2, by using port boundary conditions on the couplers and beam pipes of the cavity, the power loss of the eigenmodes P and the corresponding quality factor Q can be computed. Therefore, we use the equations (2.34), (2.35), (2.37) and (2.38) to calculate the shunt impedance and the normalized shunt impedance of the eigenmodes for the resonant cavity, respectively.

3 Discrete Electrodynamics

Apart from a few special cases, it is very hard to find an analytical solution to the Maxwell's equations. Nevertheless, an approximate numerical solution to the discretized Maxwell's equations can be found. Therefore, the continuous computational domain of interest $\Omega \subset (\mathbb{R}^1, \mathbb{R}^2, \mathbb{R}^3)$ is decomposed into a finite set of discrete elements. In this way, a set of spatial elements, which defines a topological structure in space, is named as computational grid G. The basic geometrical elements such as rectangles or triangles in the two-dimensional (2D) as well as hexahedrons or tetrahedrons in the three dimensional (3D) domain are applied. Afterwards, with the help of numerical methods the approximate numerical solution can be obtained from the discrete Maxwell's equation. The study of the electromagnetic fields dealing with the numerical solution of Maxwell's equations is known as Computational Electromagnetics (CEM). From the frequently used numerical techniques for discretization of the integral or differential equations, the Finite Integration Technique (FIT) and the Finite Element Method (FEM) are used in this dissertation for large scale computation of electromagnetic fields in the accelerators. In this chapter, both methods are introduced in section 3.1 and 3.2.

3.1 Finite Integration Technique

The Finite Integration Technique (FIT), which was developed by Thomas Weiland in 1977, is a spatial discretization approach to work out the electromagnetic field problem numerically [7] [33] [34]. With FIT a discrete formulation of the Maxwell's equations in integral form can be obtained. Currently, this technique can be applied in a wide range of the electromagnetic field problems, e.g. electro- and magnetostatics, stationary current problems as well as low- and high-frequency problems [13].

3.1.1 Spatial Discretization

The analyzed accelerators can be discretized with a hexahedral grid. Fig. 3.1a and 3.1b represent brick-shaped hexahedral and rectangle computational grid, respectively. It is noticed that the FIT can be applied by all types of coordinate meshes [35] [36].

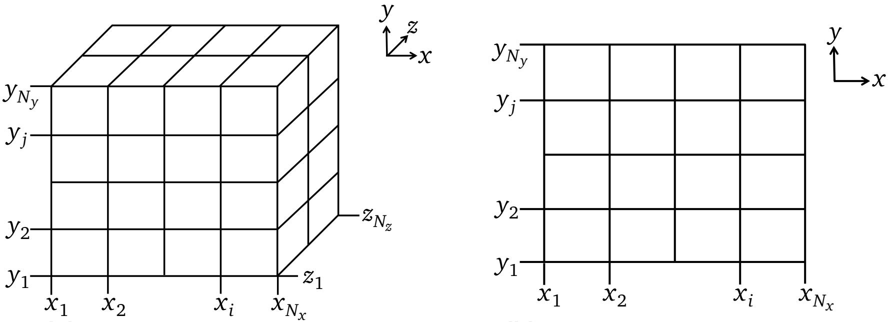

(a) 3D grid in Cartesian coordinates **(b)** 2D grid in Cartesian coordinates

Figure 3.1: Example for the discretization of a structure with equidistant grids: (a) Cartesian 3D grid. (b) Cartesian 2D grid.

The mesh cells in three dimensional computational domain $\mathbb{R}^3$ refer to the elementary volumes V_n with $n = 1, 2, ..., N_V$, which are bounded with mesh facets A_n, $n = 1, 2, ..., N_A$, where each facet has four mesh edges L_n, $n = 1, 2, ..., N_L$ and four mesh points $P_n(i, j, k)$, $n = 1, 2, ..., N_P$. Fig. 3.1a states that the grid consists of N_x, N_y and N_z grid lines in each direction of the Cartesian coordinate system [14]. A grid node $P(i, j, k)$ can be given in the Cartesian coordinate system by

$$\begin{aligned} P(i,\ j,\ k)\ =\ (x_i,\ y_j,\ z_k);\quad & x_1 < x_2 < \ldots < x_i < \ldots < x_{N_x} \\ & y_1 < y_2 < \ldots < y_j < \ldots < y_{N_y} \\ & z_1 < z_2 < \ldots < z_k < \ldots < z_{N_z}. \end{aligned} \tag{3.1}$$

Fig. 3.2 shows how the nodes, edges and facets of the mesh cells are oriented and numbered. The edge element $L_x(i, j, k)$ denotes the edge between the points $P(i, j, k)$ and $P(i+1, j, k)$, $L_y(i, j, k)$ the edge between $P(i, j, k)$ and $P(i, j+1, k)$, $L_z(i, j, k)$ the edge between $P(i, j, k)$ and $P(i, j, k+1)$. The face in y-direction with the nodes $P(i, j, k)$, $P(i+1, j, k)$, $P(i+1, j, k+1)$ and $P(i, j, k+1)$ is defined as $A_y(i, j, k)$. In this way, the other two facets $A_x(i, j, k)$ and $A_z(i, j, k)$ can be defined as well. It should be noted that there is no principal rule to orient and number the entries, but this orientation and numbering method can make the FIT algorithm more efficient.

According to the principle of FIT algorithm, a primary grid G and a dual grid $\widetilde{G}$ are required to discretize the integral form of the Maxwell's equations [8]. Fig. 3.2 states how to construct a dual grid $\widetilde{G}$. All entries of the dual grid are marked with the symbol $\sim$. Similar to the primary grid G, a dual grid $\widetilde{G}$ involves: dual points $\widetilde{P}$, dual edges $\widetilde{L}$, dual facets $\widetilde{A}$ and dual volumes $\widetilde{V}$. The dual grid is constructed in the following way: the grid nodes $\widetilde{P}$ of the grid $\widetilde{G}$ stand at the centers of the primary grids G (see Fig. 3.2). Therefore, each primary cell G contains exactly one dual grid point and vice versa [37]. The orientations of the dual edges are congruous with those of the primary edges. Moreover, each primary facet is cut by exactly one dual edge in the center of this facet, while each primary edge is cut by exactly one dual facet in the center of this edge. The dual grids have the same index as the primary grids, e.g. the dual edge $\widetilde{L}(i,j,k)$ denotes edge between the dual nodes $\widetilde{P}(i,j,k)$ and $\widetilde{P}(i+1,j,k)$.

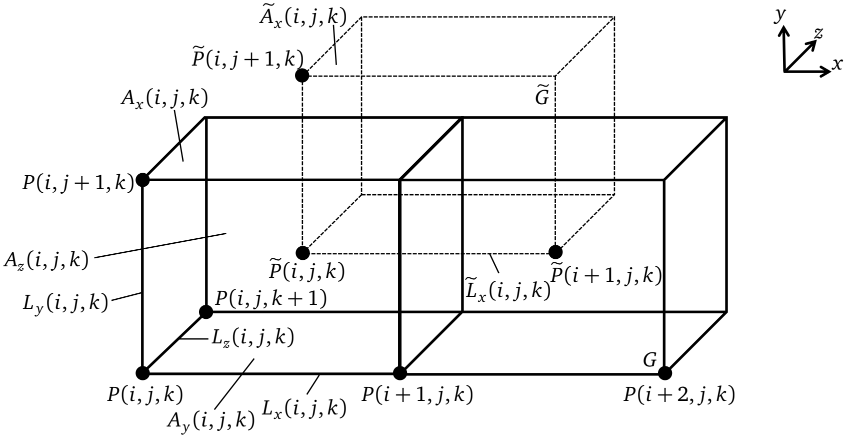

Figure 3.2: Example for a primary and dual 3D grid in Cartesian coordinate system.

3.1.2 The Maxwell's Grid Equations

According to the FIT principles, the closed line integrals from the continuous Maxwell's equitations (2.5) and (2.6) can be decomposed into the integrals along the edges of the grids, while the closed surface integrals from (2.7) and (2.8) are split into the integrals over the surfaces of the grids [38].

In the grid system, the discrete electric edge voltage $\widehat{e}_p(i,j,k)$ with $p \in \{x,y,z\}$ can be obtained by integrating the electric field strength $\mathbf{E}$ along the edge $L_p(i,j,k)$ of the primary grid G [37] [39], where $p \in \{x,y,z\}$

$$\widehat{e}_p(i,j,k) = \int_{L_p(i,j,k)} \mathbf{E} \cdot d\mathbf{s}. \tag{3.2}$$

Meanwhile, the discrete magnetic flux $\widehat{\widehat{b}}_p(i,j,k)$ can be acquired by integrating the magnetic flux density $\mathbf{B}$ over a facet $A_p(i,j,k)$ of the primary grid

$$\widehat{\widehat{b}}_p(i,j,k) \;=\; \int_{A_p(i,j,k)} \mathbf{B}\cdot d\mathbf{A} \tag{3.3}$$

Application of the Faraday's law (2.5) as well as the integrals (3.2) (3.3) to the grid surface $A_z(i,j,k)$ in Fig. 3.3 leads to

$$\widehat{e}_x(i,j,k) \;+\; \widehat{e}_y(i+1,j,k) \;-\; \widehat{e}_x(i,j+1,k) \;-\; \widehat{e}_y(i,j,k) \;=\; -\frac{d}{dt}\widehat{\widehat{b}}_z(i,j,k) \tag{3.4}$$

where the four electric voltages on the left side of (3.4) denote the four edge voltages of the grid facet $A_z(i,j,k)$, while $\widehat{\widehat{b}}_z(i,j,k)$ the magnetic flux through the grid facet $A_z(i,j,k)$.

Analogously, by repeating the same procedure for all other primary facets, the discrete form of the Faraday's law (2.5) can be obtained

$$\mathbf{C}\,\widehat{\mathbf{e}} \;=\; -\frac{d}{dt}\widehat{\widehat{\mathbf{b}}} \tag{3.5}$$

herein, all the electric voltages and the magnetic fluxes are collected in the vectors $\widehat{\mathbf{e}}$ and $\widehat{\widehat{\mathbf{b}}}$, respectively. The topological matrix $\mathbf{C}$, which is sparse and singular, plays usually the role of the continuous curl operation $\nabla\times$ of the primary grid G. All the entries of the matrix $\mathbf{C}$ are composed of -1, 0 and 1.

In an analogous manner, by applying the Gauss's law of the magnetic flux density (2.8) to the volume $V(i,j,k)$ of the primary grid G in Fig. 3.4 and using the integral (3.3), the closed surface integral can be achieved by

$$\begin{aligned} \widehat{\widehat{b}}_x(i,j,k) \;-\; \widehat{\widehat{b}}_x(i+1,j,k) \;+\; \widehat{\widehat{b}}_y(i,j,k) \;-\; \widehat{\widehat{b}}_y(i,j+1,k) \\ +\; \widehat{\widehat{b}}_z(i,j,k) \;-\; \widehat{\widehat{b}}_z(i,j,k+1) \;=\; 0 \end{aligned} \tag{3.6}$$

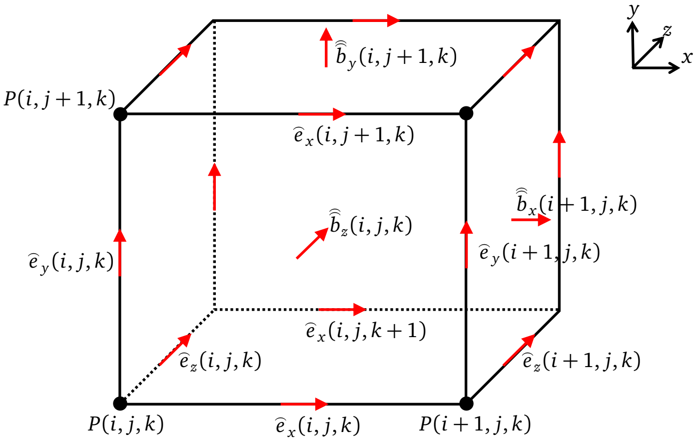

Figure 3.3: A primary grid in Cartesian coordinate system with the allocation of the electric voltages $\widehat{e}$ on the edges of this grid and the magnetic flux $\widehat{\widehat{b}}$ through the facets of this grid.

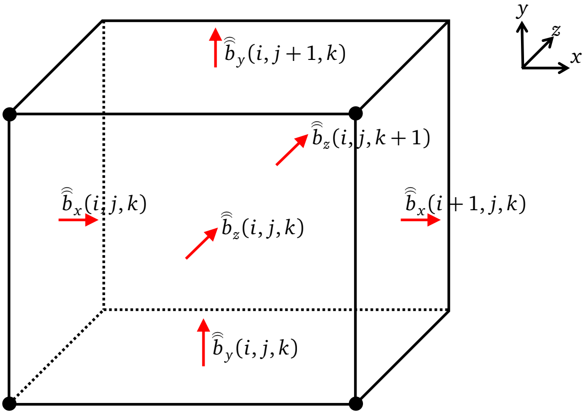

Figure 3.4: A primary grid in Cartesian coordinate system with the allocation of the magnetic flux $\widehat{\widehat{b}}$ on the facets of this grid.

Repeating the same procedure for the entire primary grid G results in the discrete form for Gauss's law of the magnetic flux density

$$\mathbf{S}\,\hat{\hat{\mathbf{b}}} = 0 \tag{3.7}$$

where the sparse topological matrix $\mathbf{S}$ is the continuous divergence operator $\nabla\cdot$ of the primary grid G.

As mentioned before, the primary (electric) grids are applied to accomplish the discretization of the Maxwell's equations (2.5) and (2.8). On the other hand, the dual (magnetic) grids are exploited for discretization of the Ampere's law (2.6) and the Gauss's law (2.7) [38]. Accordingly, the magnetic voltages $\hat{h}_p(i,j,k)$ with $p \in \{x,y,z\}$ are allocated at the edges $\tilde{L}_p(i,j,k)$ of the dual grid $\tilde{G}$, while the electric flux densities $\hat{\hat{d}}_p(i,j,k)$ with $p \in \{x,y,z\}$ at the facets $\tilde{A}_p(i,j,k)$ of the dual grid $\tilde{G}$. In an analogous manner, the discrete forms of the remaining Maxwell's equations (2.6) and (2.7) can be achieved

$$\tilde{\mathbf{C}}\,\hat{\mathbf{h}} = \frac{d}{dt}\hat{\hat{\mathbf{d}}} + \hat{\hat{\mathbf{j}}} \tag{3.8}$$

$$\tilde{\mathbf{S}}\,\hat{\hat{\mathbf{d}}} = \mathbf{q} \tag{3.9}$$

where the incidence matrices $\tilde{\mathbf{C}}$ and $\tilde{\mathbf{S}}$ are interpreted as the discrete curl operator $\nabla\times$ and the discrete divergence operator $\nabla\cdot$ corresponding to the dual grid $\tilde{G}$, receptively. Similar to the matrices $\mathbf{C}$ and $\mathbf{S}$, all the entries of the matrices $\tilde{\mathbf{C}}$ and $\tilde{\mathbf{S}}$ are composed of -1, 0 and 1. The vectors $\hat{\mathbf{h}}$ and $\hat{\hat{\mathbf{d}}}$ collect the magnetic voltages and the electric flux densities, respectively. The vector $\hat{\hat{\mathbf{j}}}$ represents the currents, while the vector $\mathbf{q}$ denotes the electric charges inside a dual grid cell. The equations (3.5), (3.7), (3.8) together with (3.9) are called the Maxwell's grid equations (MGE) [40]. It should be noticed that the four Maxwell's grid equations are the exact representations of the continuous Maxwell's equations.

A important property of these matrices is the connection between the matrices $\mathbf{C}$ and $\tilde{\mathbf{C}}$. It can be expressed by [41]

$$\tilde{\mathbf{C}} = \mathbf{C}^{\mathrm{T}} \tag{3.10}$$

Furthermore, the solution of the Maxwell's equations has to fulfill the well-known analysis relation

$$\nabla\cdot(\nabla\times\mathbf{a}) = 0 \tag{3.11}$$

where **a** are the vectors. Consequently, the relation between the discrete divergence and curl operator for the grids G and $\widetilde{G}$ can be given by

$$\mathbf{S}\mathbf{C} = 0 \tag{3.12}$$

$$\widetilde{\mathbf{S}}\widetilde{\mathbf{C}} = 0 \tag{3.13}$$

3.1.3 Material Matrices

So far, the discretization of the Maxwell's equations by using the FIT has been performed with no error. But the inaccuracy will appear in the discretization of constitutive equations (2.13) - (2.15), in case the material properties are taken into account. For the linear, frequency-independent, isotropic and non-dispersive materials the discrete forms of the equations (2.13) - (2.15) read

$$\widehat{\widehat{\mathbf{d}}} = \mathbf{M}_\epsilon \widehat{\mathbf{e}} \tag{3.14}$$

$$\widehat{\widehat{\mathbf{b}}} = \mathbf{M}_\mu \widehat{\mathbf{h}} \tag{3.15}$$

$$\widehat{\widehat{\mathbf{j}}}_\kappa = \mathbf{M}_\kappa \widehat{\mathbf{e}} \tag{3.16}$$

where $\mathbf{M}_\epsilon$, $\mathbf{M}_\mu$ and $\mathbf{M}_\kappa$ denote the permittivity matrix, the permeability matrix and the conductivity matrix, respectively. $\widehat{\widehat{\mathbf{j}}}_\kappa$ is the vector of the conductive current.

Therefore, the Maxwell's grid equations together with the discrete constitutive equations can be given with

$$\mathbf{C}\,\widehat{\mathbf{e}} = -\frac{d}{dt}\mathbf{M}_\mu \widehat{\mathbf{h}} \tag{3.17}$$

$$\widetilde{\mathbf{C}}\,\widehat{\mathbf{h}} = \frac{d}{dt}\mathbf{M}_\epsilon \widehat{\mathbf{e}} + \widehat{\widehat{\mathbf{j}}} \tag{3.18}$$

$$\widetilde{\mathbf{S}}\,\mathbf{M}_\epsilon \widehat{\mathbf{e}} = \mathbf{q} \tag{3.19}$$

$$\mathbf{S}\,\mathbf{M}_\mu \widehat{\mathbf{h}} = 0 \tag{3.20}$$

3.1.4 Boundary Condition

In order to solve the discrete Maxwell's equations, the boundary conditions must be taken into account. For instance, the Dirichlet and Neumann boundary condition are the two typical boundary conditions for the loss-free structures, e.g. the superconducting cavity in section 5.1. The Dirichlet boundary condition sets the field solution to specific values on the boundary, while the Neumann boundary condition fixes the normal derivative of the fields at the boundary to a defined value [14]. For the accelerators with PEC surrounding, the PEC boundary conditions are implemented by using the Dirichlet boundary condition, which can result in a zero electric edge voltage on the edge of the PEC boundary as well as a zero tangential electric field component at the PEC boundary. Since all the accelerating resonators and components within this thesis are perfect electric conductive, the PEC boundary conditions, i.e. the Dirichlet boundary conditions are applied.

3.1.5 Curl-Curl Eigenvalue Equation

For the time harmonic electromagnetic fields, the time derivative operator $\frac{d}{dt}$ can be replaced by the factor $\jmath\omega$ [42]. Thus, the time derivative operator comes to be a multiplication of the complex amplitude with the factor $\jmath\omega$. Moreover, the perfect electric conductive accelerating structures with no additional sources lead to a zero electric current density $\mathbf{J}$ in (2.6) and a zero electric charge density ρ in (2.7). Consequently, the Maxwell's grid equations become the complex equations in frequency domain and can be read

$$\mathbf{C}\,\underline{\widehat{\mathbf{e}}} = -\jmath\omega\,\underline{\widehat{\widehat{\mathbf{b}}}} \tag{3.21}$$

$$\widetilde{\mathbf{C}}\,\underline{\widehat{\mathbf{h}}} = \jmath\omega\,\underline{\widehat{\widehat{\mathbf{d}}}} \tag{3.22}$$

$$\widetilde{\mathbf{S}}\,\underline{\widehat{\widehat{\mathbf{d}}}} = 0 \tag{3.23}$$

$$\mathbf{S}\,\underline{\widehat{\widehat{\mathbf{b}}}} = 0 \tag{3.24}$$

where the unknown discrete vectors $\underline{\widehat{\mathbf{e}}}$, $\underline{\widehat{\widehat{\mathbf{b}}}}$, $\underline{\widehat{\mathbf{h}}}$ as well as $\underline{\widehat{\widehat{\mathbf{d}}}}$ have the complex amplitudes and are named as discrete phasors.

In this thesis, only the case of the perfect conductive, linear, frequency-independent, isotropic and non-dispersive material ($\sigma = 0$, ϵ, $\mu \in \mathbb{R}$) is considered for the FIT. Moreover, the computational space is source free. Combination of the first two grid Maxwell's equations (3.21)-(3.22) and application of the discretized material equations (3.14)-(3.15) leads to the discrete FIT eigenvalue formulation

$$\mathbf{M}_{\epsilon}^{-1}\widetilde{\mathbf{C}}\mathbf{M}_{\mu}^{-1}\mathbf{C}\underline{\widehat{\mathbf{e}}} = \omega^2\,\underline{\widehat{\mathbf{e}}} \tag{3.25}$$

$$\mathbf{A} = \mathbf{M}_{\epsilon}^{-1}\widetilde{\mathbf{C}}\mathbf{M}_{\mu}^{-1}\mathbf{C} \tag{3.26}$$

where the system matrix **A** is asymmetric. This equation can be called discrete curl-curl equation due to two applications of the discrete curl operator. The eigenvalues of the system matrix **A** are the square of the resonance frequencies ω_i, while the solutions of the equation (3.25) are the non-trivial eigenvectors $e_i \neq 0$, which correspond to the fields of the eigenmodes in the accelerators.

If the material matrices $\mathbf{M}_\epsilon^{-1}$ and $\mathbf{M}_\mu^{-1}$ are both symmetric and positive definite, $\mathbf{M}_\epsilon^{-1}$ and $\mathbf{M}_\mu^{-1}$ can be decomposed as

$$\mathbf{M}_\epsilon^{-1} = \mathbf{M}_\epsilon^{-\frac{1}{2}}\mathbf{M}_\epsilon^{-\frac{1}{2}} \tag{3.27}$$

$$\mathbf{M}_\mu^{-1} = \mathbf{M}_\mu^{-\frac{1}{2}}\mathbf{M}_\mu^{-\frac{1}{2}} \tag{3.28}$$

Insertion of the equations (3.10), (3.27) and (3.28) into the matrix **A** results in the following formulation [43]

$$\mathbf{A} = \mathbf{M}_\epsilon^{-1}\widetilde{\mathbf{C}}\mathbf{M}_\mu^{-1}\mathbf{C} = \mathbf{M}_\epsilon^{-\frac{1}{2}}(\mathbf{M}_\mu^{-\frac{1}{2}}\mathbf{C}\mathbf{M}_\epsilon^{-\frac{1}{2}})^{\mathrm{T}}(\mathbf{M}_\mu^{-\frac{1}{2}}\mathbf{C}\mathbf{M}_\epsilon^{-\frac{1}{2}})\mathbf{M}_\epsilon^{\frac{1}{2}} \tag{3.29}$$

with the transformations

$$\mathbf{A}' = (\mathbf{M}_\mu^{-\frac{1}{2}}\mathbf{C}\mathbf{M}_\epsilon^{-\frac{1}{2}})^{\mathrm{T}}(\mathbf{M}_\mu^{-\frac{1}{2}}\mathbf{C}\mathbf{M}_\epsilon^{-\frac{1}{2}}) \tag{3.30}$$

$$\underline{\widehat{\mathbf{e}}}' = \mathbf{M}_\epsilon^{\frac{1}{2}}\underline{\widehat{\mathbf{e}}} \tag{3.31}$$

The equation (3.25) can be rewritten as

$$\mathbf{A}'\underline{\widehat{\mathbf{e}}}' = \omega^2\underline{\widehat{\mathbf{e}}}' \tag{3.32}$$

where the matrix $\mathbf{A}'$ is real and symmetric. It should be noted that the eigenvalues of the matrix $\mathbf{A}'$ are identical to the eigenvalues of **A** [44].

3.2 Finite Element Method

The Finite Element Method (FEM) is a standard numerical tool to find approximate solutions for partial differential equations in many scientific fields, e.g. electromagnetics, mechanics and fluid dynamics. It is a powerful numerical technique for dealing with the problems involving complex geometries and inhomogeneous media. The problem to be solved in the spatial domain Ω by FEM can be put under the following formulations

$$F\,u(x,\ t) = b(x,\ t) \tag{3.33}$$

$$f_s(u,\ t) = h(x,\ t) \quad \text{on the boundary } \partial\Omega \tag{3.34}$$

herein, F denotes an operator, u is the unknown function that must be numerically determined, and b stands for the source. Moreover, x is the generic point of the spatial domain Ω, while t is the time variable. If the problem is frequency dependent, the time variable t can be replaced by the frequency f. The equation (3.34) describes the boundary conditions on the boundary $\partial\Omega$ of the domain.

Basically, the FEM analysis for an electromagnetic problem includes four steps [45]:

- Discretization of the geometry (solution domain)
- Approximation of the solution (selection of the basis functions)
- Approximation of the equation (the Maxwell's equations)
- Solution of the system of equations

The basic idea of the FEM method is to divide the continuous solution domain (real geometry) into a finite number of sub-domains in which the unknown solutions can be approximated by basis functions with unknown coefficients. On next step a system of the equations (Maxwell's equations) can be approximated according to a specific method (Ritz method or Galerkin's approach). Finally, the solution of the problem is achieved by solving the obtained system of the equations numerically. In the following subsections an overview of the four steps will be shortly introduced.

3.2.1 Domain Discretization

At the first step, the real geometry is divided into small cells or elements. This step is probably the most important in the finite element analysis, because it can affect the computation time, the requirement of the hardware as well as the accuracy of the obtained numerical results. In principle, any type of geometric elements can be applied for FEM. Fig. 3.5 shows the typical basic finite elements. In one-dimensional domain, a straight line can be the type of the mesh (Fig. 3.5a). For a two-dimensional domain, the typical mesh elements are the rectangles and triangles (Fig. 3.5b), while the elements are usually hexahedral bricks and tetrahedrons in a three dimensional domain (Fig. 3.5c). The rectangles and hexahedrons can be simply generated from an algorithmic point of view and are suited for discretization of the rectangular and hexahedral regions. But in order to represent the structures with curved boundaries, e.g. the elliptical superconducting cavity, precisely, a large number of rectangular or hexahedral mesh cells, which can lead to more computation time, is required to avoid a geometry approximation error (see Fig. 3.6a) [46].

On the other hand, application of the triangles and tetrahedrons allows a good representation of the curved structures (see Fig. 3.6b). However, the generation of the triangular and tetrahedral meshes, especially the curvilinear tetrahedrons, requires a much large effort. In this thesis the hexahedral and tetrahedral meshes have been applied to the approximations of the accelerating resonators with curved boundaries.

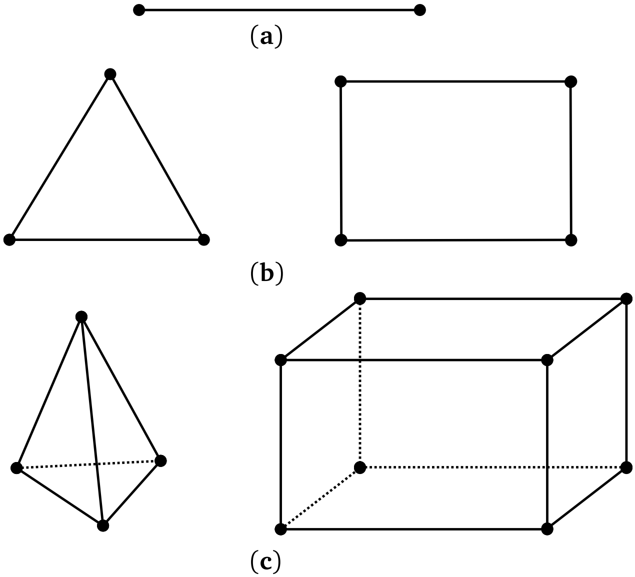

Figure 3.5: Typical basic finite elements. (a) One-dimensional. (b) Two-dimensional. (c) Three-dimensional.

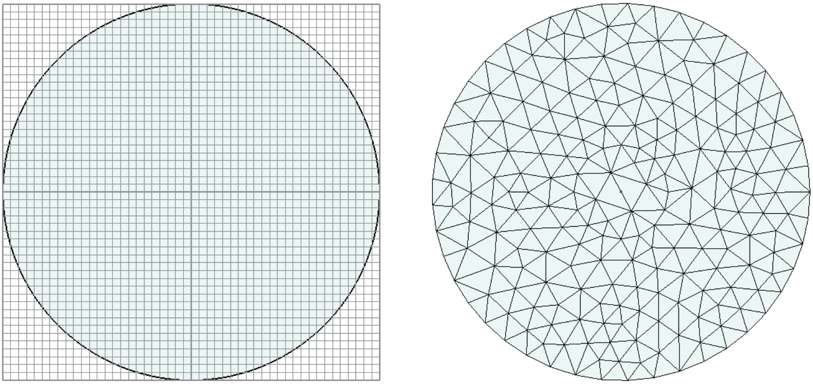

(a) Hexahedral mesh grid in Cartesian coordinates

(b) Tetrahedral mesh grid in Cartesian coordinates

Figure 3.6: Cross section of hexahedral and tetrahedral mesh in a plane normal to the longitudinal axis of the resonator.

3.2.2 Solution Approximation

The second step of the FEM analysis is the selection of the basis functions to approximate the unknown solutions. Namely, the solution to be sought is described as a linear combination of a finite number of the basis functions

$$u(\mathbf{r}) = \sum_{j=1}^{n} a_j \boldsymbol{w}_j(\mathbf{r}), \tag{3.35}$$

where a_j denotes the unknown coefficient of the linear combination, $\boldsymbol{w}_j$ the basis function. $\mathbf{r}$ is a point in the problem domain Ω. The basis function $\boldsymbol{w}_j$ is usually a polynomial of first (linear), second (quadratic) or higher-order [45]. The usage of the higher-order polynomials can increase the accuracy of the obtained numerical results. On the other side, the higher-order polynomials result in a complicated formulations and a demanding computation task. In this thesis the basis functions up to the second order are used to maintain the high approximation of the elliptical curved superconducting cavity [47].

Selecting the type of the basis functions is dependent on the type of the problem. The type of the basis functions is either the scalar or the vectorial basis functions. The scalar basis functions, which are defined as nodal functions, are allocated on nodes (scalar potential), while another type of scalar basis functions named as volume functions stands for the quantities integrated on volumes, for instance the electric charge. On the other side, one type of the vectorial basis functions, which are defined as edge functions, is allocated on edges (field intensities), while another type of the vectorial basis functions is the face function, which stands for the quantities integrated on surfaces, such as magnetic flux densities [46]. Considering a mesh with N nodes, E edges, F facets and T tetrahedrons, the geometry elements of the mesh where the basis functions can be defined are [44]:

- nodes, which are not oriented entities
- edges, which are oriented by the order of the nodes (Nédélec edge element)
- faces, which are also oriented by the order of the nodes (Raviart-Thomas face element)
- volumes, which are not oriented entities.

In the following, the first order nodal and edge functions are described shortly, because they are applied to the implementation in chapter 4.

3.2.2.1 Nodal Functions

Let us consider a triangle with the nodes 1, 2 and 3 (Fig. 3.7a). The first order (linear) basis function N_1 allocated on node 1 can be expressed by

$$N_1(x,\ y) = a_1 x + b_1 y + c_1 \tag{3.36}$$

for an arbitrary point (x, y) in the triangle. The nodal function N_1 must have the value of 1 at its own node 1 and the value of zero for the other two remaining nodes within the element [48]

$$\begin{aligned} N_1(x_1,\ y_1) &= 1 \\ N_1(x_2,\ y_2) &= 0 \\ N_1(x_3,\ y_3) &= 0 \end{aligned} \tag{3.37}$$

Analogously, the other two nodal functions N_2 and N_3 have the same property.

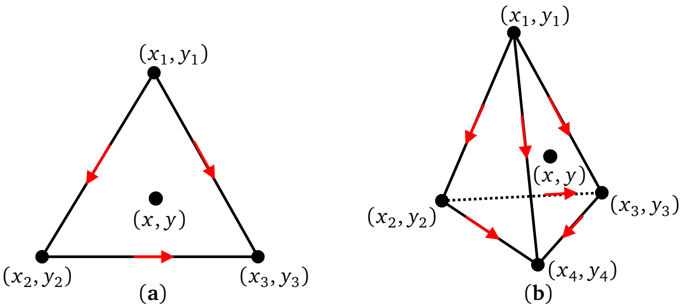

Figure 3.7: Generic (global) mesh elements. (a) Triangle in a 2D mesh. (b) Tetrahedron in a 3D mesh.

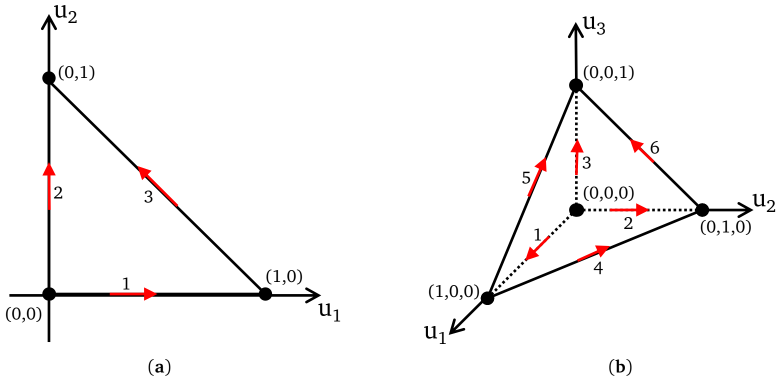

Figure 3.8: Reference mesh elements with the linear oriented edge elements. (a) 2D reference triangle in Cartesian coordinate system. (b) 3D reference tetrahedron in Cartesian coordinate system.

Another important property of the linear nodal functions can be given by

$$\sum_{i=1}^{3} N_i = 1 \tag{3.38}$$

It is obvious that once two nodal functions are known, the third one can be determined by (3.38). The coefficients in equation (3.36) can be determined by solving the system of the equations (3.37).

For the standard reference triangle (Fig. 3.8a), the three linear nodal functions can be expressed by

$$\widehat{N}_1(\mathrm{u}_1,\ \mathrm{u}_2) = 1 - \mathrm{u}_1 - \mathrm{u}_2 \tag{3.39}$$

$$\widehat{N}_2(\mathrm{u}_1,\ \mathrm{u}_2) = \mathrm{u}_1 \tag{3.40}$$

$$\widehat{N}_3(\mathrm{u}_1,\ \mathrm{u}_2) = \mathrm{u}_2 \tag{3.41}$$

Analogously, on a tetrahedron with the nodes 1, 2, 3 and 4 (Fig. 3.7b), the first order nodal function N_i allocated on node i with $i = 1, 2, 3, 4$ can be read

$$N_i(x,\ y,\ z) = a_i x + b_i y + c_i z + d_i \tag{3.42}$$

at an arbitrary point (x, y, z) within the tetrahedron. The 3D nodal functions N_i must be equal 1 at the node i and zero for the other three nodes within the element and have the following property

$$\sum_{i=1}^{4} N_i = 1 \tag{3.43}$$

The relation (3.43) shows that the four nodal functions are not independent, one of them can be determined by the other three functions. For the standard reference tetrahedron (Fig. 3.8b), the four linear nodal functions can read

$$\widehat{N}_1(\mathrm{u}_1,\ \mathrm{u}_2,\ \mathrm{u}_3) = 1 - \mathrm{u}_1 - \mathrm{u}_2 - \mathrm{u}_3 \tag{3.44}$$

$$\widehat{N}_2(\mathrm{u}_1,\ \mathrm{u}_2,\ \mathrm{u}_3) = \mathrm{u}_1 \tag{3.45}$$

$$\widehat{N}_3(\mathrm{u}_1,\ \mathrm{u}_2,\ \mathrm{u}_3) = \mathrm{u}_2 \tag{3.46}$$

$$\widehat{N}_4(\mathrm{u}_1,\ \mathrm{u}_2,\ \mathrm{u}_3) = \mathrm{u}_3 \tag{3.47}$$

Afterwards, the global nodal functions N_i defined on the generic triangle or tetrahedron as well as its gradient operator ∇N_i can be determined from the reference nodal functions $\widehat{N}_i$ and its gradient operator $\nabla \widehat{N}_i$ by using Piola transformation, respectively [49]. The corresponding transformation will be introduced in chapter 4.

The higher-order basis nodal functions, such as application of second order polynomials, can be used to increase the accuracy of the numerical results without generation of a fine mesh. The higher-order basis nodal functions can be derived by different procedures, for instance, Lagrange family [50] and have been already presented in many scientific literatures.

3.2.2.2 Edge Functions

The vectorial basis functions are required to appropriately represent the unknown vector fields, such as electric field strength **E**. One type of the vectorial basis functions is the edge function, which is allocated on the edges of the triangle and tetrahedron (the red arrows in Fig. 3.7 and Fig. 3.8). The edge functions have tangential continuity. This means that the tangential components of the edge functions are continuous at the shared edge of two tetrahedrons, whereas the normal components could be discontinuous. The advantage of the edge function is its ability to avoid the nonphysical solution, such as spurious or ghost modes, for the eigenvalue problems [46]. Each edge basis function can be only allocated on its "own" edge.

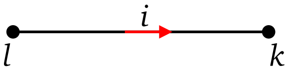

Figure 3.9: Oriented edge i

It means that, the integral of the edge function on its own edge must be 1 and it should be zero on all other edges of the tetrahedron. In chapter 4 of this thesis, we use the linear Nédélec edge elements to represent the edge basis functions for the implementation [51] [52]. The first order Nédélec edge function $\boldsymbol{w}_i$ mapped on the nodes l and k (Fig. 3.9) can be obtained from the nodal functions by

$$\boldsymbol{w}_i = N_k \nabla N_l - N_l \nabla N_k \tag{3.48}$$

Analogous to the nodal functions, the three 2D linear edge functions for the standard reference triangle (Fig. 3.8a) can be given by

$$\widehat{\boldsymbol{w}}_1 = \begin{pmatrix} 1 - \mathrm{u}_2 \\ \mathrm{u}_1 \end{pmatrix} \tag{3.49}$$

$$\widehat{\boldsymbol{w}}_2 = \begin{pmatrix} \mathrm{u}_2 \\ 1 - \mathrm{u}_1 \end{pmatrix} \tag{3.50}$$

$$\widehat{\boldsymbol{w}}_3 = \begin{pmatrix} -\mathrm{u}_2 \\ \mathrm{u}_1 \end{pmatrix} \tag{3.51}$$

The six 3D linear edge functions for the standard reference tetrahedron (Fig. 3.8b) can read

$$\widehat{\boldsymbol{w}}_1 = \begin{pmatrix} 1 - \mathrm{u}_2 - \mathrm{u}_3 \\ \mathrm{u}_1 \\ \mathrm{u}_1 \end{pmatrix} \tag{3.52}$$

$$\widehat{\boldsymbol{w}}_2 = \begin{pmatrix} \mathrm{u}_2 \\ 1 - \mathrm{u}_1 - \mathrm{u}_3 \\ \mathrm{u}_2 \end{pmatrix} \tag{3.53}$$

$$\widehat{\boldsymbol{w}}_3 = \begin{pmatrix} \mathrm{u}_3 \\ \mathrm{u}_3 \\ 1 - \mathrm{u}_1 - \mathrm{u}_2 \end{pmatrix} \tag{3.54}$$

$$\widehat{\boldsymbol{w}}_4 = \begin{pmatrix} -\mathrm{u}_2 \\ \mathrm{u}_1 \\ 0 \end{pmatrix} \tag{3.55}$$

$$\widehat{\boldsymbol{w}}_5 = \begin{pmatrix} -\mathrm{u}_3 \\ 0 \\ \mathrm{u}_1 \end{pmatrix} \tag{3.56}$$

$$\widehat{\boldsymbol{w}}_6 = \begin{pmatrix} 0 \\ -\mathrm{u}_3 \\ \mathrm{u}_2 \end{pmatrix} \tag{3.57}$$

Afterwards, by applying the Piola transformation the global edge functions $\boldsymbol{w}_i$ and the curl-operator $\nabla \times \boldsymbol{w}_i$ can be calculated from the reference edge functions $\widehat{\boldsymbol{w}}_i$ and the curl-operator $\nabla \times \widehat{\boldsymbol{w}}_i$, respectively [53] [54]. The corresponding details will be introduced in chapter 4. Certainly, there are higher-order edge elements, which can increase the accuracy of the numerical solution. But on the other side, higher-order edge elements can lead to a much more demanding computational job. In chapter 5, the higher-order Nédélec edge elements are applied to the Computational Electromagnetics 3D solver (CEM3D), which has been developed by Dr. Wolfgang Ackermann from TEMF and is used to solve the large-scale eigenvalue problems for the superconducting cavities [47] [55].

3.2.3 Equation Approximation

The third step of the FEM is to discretize the Maxwell's equations. For this purpose various approaches, such as Rayleigh-Ritz method or Weighed Residual method, are used [56]. The Rayleigh-Ritz method is a direct variational method. However, this method has its limitation and can be only applied to solve some specific issues [46] [57]. Therefore, the Weighted Residual method is used. Compared with the Rayleigh-Ritz method, this method is more general and has a wide application.

Let us consider the operator equation

$$LT = g \tag{3.58}$$

where L denotes an operator and T is the unknown function. The exact solution to the equation (3.58) can be approximated as a linear combination of the basis functions $\boldsymbol{w}_j$

$$\widetilde{T} = \sum_{j=1}^{n} a_j \boldsymbol{w}_j, \tag{3.59}$$

where a_j are the unknown coefficients, $\widetilde{T}$ is the approximate solution. The residual of the equation (3.58) can be defined as

$$R = L\widetilde{T} - g \tag{3.60}$$

In general, the residual will be zero for the exact solution. However, the residual is normally nonzero for an approximate solution. For the Weighed Residual method, the weighting functions u_i are chosen in order that the residual is zero in average on the whole computational domain Ω. The average is defined as the integral on the domain Ω of the weighted residual, i.e.

$$\int_{\Omega} R\, u_i \, dV = 0, \quad i = 1, 2, ..., n \tag{3.61}$$

where the weighting residual u_i can be also called testing function. The equation (3.61) can lead to a system of n equations, which can be cast into a matrix form. From that the unknown coefficients a_j can be obtained [46] [56].

The different weighting functions lead to various variants of the method [56]:

- The Collocation method: the Dirac delta function is chosen as the weighting function.
- The Least Squares method: the residual function is selected as the weighting function.

- The Galerkin's method: the basis function is selected as the weighting function, i.e. $u_i = \boldsymbol{w}_i$.

The Galerkin's method is a widely used approach and applied to the implementation in chapter 4. The approximation of the Maxwell's equations with the Galerkin's method will be stated in the next chapters.

3.2.3.1 Boundary Conditions

In order to obtain the final form of the system of the equations, the proper boundary conditions have to be imposed. As mentioned before, two famous kinds of boundary conditions, i.e. the Dirichlet and Neumann boundary conditions, can be applied in case that the energy exchange with the surrounding does not occur. In fact, for the accelerators the energy dissipation can appear with the help of dedicated higher-order mode (HOM) couplers, the power coupler as well as the beam pipes. Therefore, the port boundary conditions [47] can be applied to those dissipative accelerators. In the next chapters the port boundary conditions will be introduced in more details.

3.2.4 Solution of the System of Equations

The final step of the FEM analysis is to solve the system of the equations. This step is very time-consuming in a FEM analysis, for instance, the analysis for the large-scale eigenvalue problems. In general, the resultant systems of equations are very large and sparse. Therefore, an iterative method is used to solve them. However, the convergence rate of such method is strongly affected by the condition number of the system matrix [58] [59]. For instance, the system of the curl-curl elliptic equations could have a large condition number, which can lead to a very slow convergence rate of the iterative method and even inaccurate numerical solutions. For this reason, specific approaches are developed to speed up the convergence and to obtain accurate numerical solutions [36] [44].

Once the system of the equations is solved, the quantities of interest, such as the electric field strength **E** and impedances, can be determined. The achieved results can be shown in form of curve- and scatter-plots, which are more interpretable and meaningful.

4 Computation of the Broadband Impedance in Accelerating Components

As explained in chapter 2, the broadband impedance describes the electromagnetic interaction of the particle beam with its surrounding environment inside the accelerating components in frequency domain [60]. On the basis of the Finite Element Method (FEM), a numerical approach for the three dimensional (3D) computation of the longitudinal space charge impedances in frequency domain has been developed. This numerical approach is applicable at a very wide frequency range, particularly at low and medium frequencies where the time domain methods such as Finite Differences Time Domain (FDTD) become inapplicable [61]. In this section, the definition of the longitudinal broadband space charge impedance is introduced at first. Afterwards, section 4.2 will describe how the Maxwell's equations are discretized to perform the 3D FEM computation. In addition, the formulation of the applied boundary conditions will be stated. Finally, a simple application together with the limitation of this type of solver will be presented.

4.1 Broadband Impedances

Assuming that the particle beam in a form of a disc with radius a and an uniform surface charge density σ is traveling through a resonant cavity with cylindrical beam pipes with constant velocity $\boldsymbol{v} = \beta c_0 \boldsymbol{e_z}$. In this section, a coherent dipole oscillation is neglected. Then, the charge density σ is approximated in cylindrical coordinates (ϱ, φ) as follows [62],

$$\sigma(\varrho, \varphi) = \frac{q}{\pi a^2}(\Theta(a - \varrho)) \tag{4.1}$$

where q is the total charge of the particle beam, and Θ denotes the Heaviside step function [61]. The current density in time domain can then be given by

$$\mathbf{J} = \sigma \boldsymbol{v} \delta(z - vt) \tag{4.2}$$

where δ is the Dirac distribution. Performing a Fourier transformation of (4.2), the current density in frequency domain can be read as

$$\underline{\mathbf{J}} = \sigma e^{-\jmath\omega z/\beta c_0}\boldsymbol{e}_z. \tag{4.3}$$

Then, the longitudinal beam coupling (broadband) impedance can be given by [28]

$$\underline{Z}_{||}(\omega) = -\frac{l}{q^2}\int_{beam} \underline{\mathbf{E}}\cdot\underline{\mathbf{J}}^* dV \tag{4.4}$$

where l is the length of the resonant cavity with cylindrical beam pipe. The task is to solve the Maxwell's equations subject to the excitation given by equation (4.3) in frequency domain to determine the electric field strength **E**. Afterwards, the broadband impedance can be computed by (4.4).

4.2 Mathematical Modeling

The Maxwell's equations in frequency domain for linear isotropic materials can be given by (4.5) - (4.10) [48],

$$\nabla\times\underline{\mathbf{H}} = \underline{\mathbf{J}} + \jmath\omega\underline{\mathbf{D}} \tag{4.5}$$

$$\nabla\times\underline{\mathbf{E}} = -\jmath\omega\underline{\mathbf{B}} \tag{4.6}$$

$$\underline{\mathbf{D}} = \epsilon\underline{\mathbf{E}} = \epsilon_0\epsilon_r\underline{\mathbf{E}} \tag{4.7}$$

$$\underline{\mathbf{B}} = \mu\underline{\mathbf{H}} = \mu_0\mu_r\underline{\mathbf{H}} \tag{4.8}$$

$$\nabla\cdot\underline{\mathbf{D}} = \rho \tag{4.9}$$

$$\nabla\cdot\underline{\mathbf{B}} = 0 \tag{4.10}$$

where the excitation source $\underline{\mathbf{J}}$ in (4.5) is defined by (4.3) together with (4.1). The materials used in this chapter are linear, frequency-independent and isotropic definite.

Combing the first two Maxwell's equations (4.5) and (4.6), by using the linear isotropic material equation (4.7) and (4.8) the second order form in terms of the electric field strength can be read as

$$\nabla\times\nu\nabla\times\underline{\mathbf{E}} - \omega^2\epsilon\underline{\mathbf{E}} = -\jmath\omega\underline{\mathbf{J}} \tag{4.11}$$

where $\nu = \mu^{-1}$ is the reluctivity and real valued due to the considered zero-loss magnetic materials.

Because of the ability to model the required tangential continuity, we use the well-known Nédélec edge elements to discretize the continuous equation (4.11) [53] [63] [64] [65]. Since the lowest order Nédélec edge elements are divergence-free [66], the electric field strength $\underline{\mathbf{E}}$ in (4.11) is calculated separately by a Helmholtz split [67]

$$\underline{\mathbf{E}} = \underline{\mathbf{E}}_{\text{curl}} + \underline{\mathbf{E}}_{\text{div}} \tag{4.12}$$

where $\underline{\mathbf{E}}_{\text{curl}}$ processes the property $\nabla \cdot (\epsilon \underline{\mathbf{E}}_{\text{curl}}) = 0$ and $\underline{\mathbf{E}}_{\text{div}}$ represents the curl-free part, i.e. $\nabla \times \underline{\mathbf{E}}_{\text{div}} = 0$. Combining the equations (4.1), (4.3) and applying Gauss's law, we can obtain the Poisson equation

$$\nabla \cdot \epsilon \nabla \underline{\Phi} = -\frac{1}{\beta c_0} \cdot \sigma e^{-\jmath \omega z / \beta c_0} \tag{4.13}$$

to determine the complex potential $\underline{\Phi}$. Once the potential $\underline{\Phi}$ is known, the divergence part of $\underline{\mathbf{E}}$ can be calculated according to

$$\underline{\mathbf{E}}_{\text{div}} = -\nabla \underline{\Phi}. \tag{4.14}$$

Insertion of (4.12) into the formulation (4.11) leads to

$$\nabla \times \nu \nabla \times \underline{\mathbf{E}}_{\text{curl}} - \omega^2 \epsilon \underline{\mathbf{E}}_{\text{curl}} = -\jmath \omega \underline{\mathbf{J}} + \omega^2 \epsilon \underline{\mathbf{E}}_{\text{div}} =: \underline{\mathbf{R}} \tag{4.15}$$

with a divergence-free right hand side i.e. $\nabla \cdot (-\jmath \omega \underline{\mathbf{J}} + \omega^2 \epsilon \underline{\mathbf{E}}_{\text{div}}) = 0$.

4.2.1 Poisson Solver

The continuous distribution of the electric scalar potential $\underline{\Phi}$ defined in (4.13) can be approximated by 3D scalar nodal elements according to [56]

$$\underline{\Phi}(x, y, z) = \sum_{j=1}^{m} c_j N_j^{3D}(x, y, z) \tag{4.16}$$

with the scalar weighting coefficients c_j and the scalar-valued basis functions N_j^{3D}. Insertion of (4.16) into the formulation (4.13) and application of the standard Galerkin's procedure leads to the 3D discrete Poisson formulation

$$\sum_{j=1}^{m} c_j \left(S_{ij}^{3D} - B_{\epsilon,ij} \right) = \int_V \rho N_i^{3D} dV \tag{4.17}$$

with the boundary term $B_{\epsilon,ij}$,

$$B_{\epsilon,ij} = \int_{\partial V} N_j^{3D} \epsilon \frac{\partial N_i^{3D}}{\partial \mathbf{n}} dA = \int_{\partial V} N_j^{3D} \epsilon (\nabla N_i^{3D} \mathbf{n}) dA \tag{4.18}$$

which must be calculated on the surface of the structure. The vector $\mathbf{n}$ denotes the unit surface normal vector.
The $S_{ij}, i, j = 1, ..., m$ is known as the FEM stiffness matrix [68]. The stiffness matrix components

$$S_{ij}^{3D} = \int_V \nabla N_i^{3D} \epsilon \cdot \nabla N_j^{3D} dV \tag{4.19}$$

can be computed with the help of numerical integration by Gauss quadrature rules [69]. The equations (4.19) must be evaluated for each element within the computational domain V. Each individual integration from an element indicated by superscript k can be calculated with

$$S_{ij}^{3D,k} = \int_{V_0} \nabla N_i^{3D} \epsilon \cdot \nabla N_j^{3D} |J_{3D}| dV \tag{4.20}$$

where V_0 is a unit tetrahedron. The appearing matrix J_{3D} represents the Jacobian of the geometrical transformation and $|J_{3D}|$ denotes its determinant. For planar tetrahedrons, the Jacobian matrix can be easily computed according to

$$J_{3D} = \begin{bmatrix} x_2 - x_1 & x_3 - x_1 & x_4 - x_1 \\ y_2 - y_1 & y_3 - y_1 & y_4 - y_1 \\ z_2 - z_1 & z_3 - z_1 & z_4 - z_1 \end{bmatrix} \tag{4.21}$$

where (x_1, y_1, z_1), (x_2, y_2, z_2), (x_3, y_3, z_3) and (x_4, y_4, z_4) refer to the coordinates of the four vertices [70].

The 3D scalar-valued basis functions N_i^{3D} and their gradients ∇N_i^{3D} can be expressed from an unit reference element with the fixed local basis functions $\widehat{N}_i^{3D}$ [71] [72] by the Piola transformations

$$N_i^{3D} = \widehat{N}_i^{3D} \tag{4.22}$$

$$\nabla N_i^{3D} = (J_{3D}^{-1})^{\mathrm{T}} \cdot \nabla \widehat{N}_i^{3D} \tag{4.23}$$

Based on a given discretized structure the entire system of the equations (4.17) can be assembled according to (4.18) - (4.23).

$$\left[\ \boldsymbol{S}^{\mathbf{3D}} + \boldsymbol{B}_{\epsilon}\ \right] \left[\ \boldsymbol{c}\ \right] = \left[\ \boldsymbol{\rho}\ \right] \tag{4.24}$$

with the bold small letter $\boldsymbol{c}$ denoting the desired vector of weighting coefficients. We apply the inhomogeneous Dirichlet boundary condition to formulate the boundary term $\boldsymbol{B}_{\epsilon}$ [73] [74]. After solving (4.24), the curl-free electric field strength $\underline{\mathbf{E}}_{\mathrm{div}}$ can be determined by (4.14).

4.2.2 Curl-Curl Solver

In a next step, the application of the Galerkin's test procedure [75] to (4.15) results in

$$\int_V (\nabla \times \nu(\nabla \times \underline{\mathbf{E}}_{\mathrm{curl}}) - \omega^2 \epsilon \underline{\mathbf{E}}_{\mathrm{curl}}) \cdot \boldsymbol{w}_i^{3D} dV = \int_V \underline{\mathbf{R}} \cdot \boldsymbol{w}_i^{3D} dV \tag{4.25}$$

where $\boldsymbol{w}_i^{3D}$ represents the real-valued vectorial test function. While the current work concentrates on first-order elements, higher-order elements can be used as well. We use a well-known expansion formula to transform the left hand side of (4.26) [76]

$$\nabla \cdot (\mathbf{a} \times \mathbf{b}) = \mathbf{b} \cdot \nabla \times \mathbf{a} - \mathbf{a} \cdot \nabla \times \mathbf{b} \tag{4.26}$$

where $\mathbf{a}$ and $\mathbf{b}$ are given vectors. Consequently, we can obtain:

$$\nabla \times \nu(\nabla \times \underline{\mathrm{E}}) \cdot \boldsymbol{w}_i^{3D} = \nabla \cdot (\nu(\nabla \times \underline{\mathrm{E}}) \times \boldsymbol{w}_i^{3D}) + (\nu \nabla \times \underline{\mathrm{E}}) \cdot (\nabla \times \boldsymbol{w}_i^{3D}). \tag{4.27}$$

By applying the Ostrogradsky's theorem (4.28)

$$\int_V \nabla \cdot \mathbf{a} \, dV = \int_{\partial V} \mathbf{a} \cdot \mathbf{n} \, dA. \tag{4.28}$$

Equation (4.25) can be rewritten as

$$\int_V \nu(\nabla \times \underline{\mathbf{E}}_{\text{curl}}) \cdot (\nabla \times \boldsymbol{w}_i^{3D}) \, dV + \int_{\partial V} \nu(\nabla \times \underline{\mathbf{E}}_{\text{curl}}) \times \boldsymbol{w}_i^{3D} \cdot \mathbf{n} \, dA - \omega^2 \int_V \epsilon \underline{\mathbf{E}}_{\text{curl}} \cdot \boldsymbol{w}_i^{3D} \, dV = \int_V \underline{\mathbf{R}} \cdot \boldsymbol{w}_i^{3D} \, dV \tag{4.29}$$

where the surface integral $\int_{\partial V} \nu(\nabla \times \underline{\mathbf{E}}_{\text{curl}}) \times \boldsymbol{w}_i^{3D} \cdot \mathbf{n} \, dA$ refers to the boundary condition. A proper formulation of the boundary condition is essential for the impedance computation in the accelerators.

The unknown electric field strength specified in (4.29) is discretized by Nédélec type vector basis functions [51] [52] according to

$$\underline{\mathbf{E}}_{\text{curl}}(x, y, z) = \sum_{i=j}^{m} \alpha_j \boldsymbol{w}_j^{3D}(x, y, z) \tag{4.30}$$

where α_j are the complex-valued weighting coefficients [49]. Inserting (4.30) into the weak FEM equation (4.29) leads to

$$\begin{aligned} &\int_V \nu(\nabla \times (\sum_{j=1}^{m} \alpha_j \boldsymbol{w}_j^{3D})) \cdot (\nabla \times \boldsymbol{w}_i^{3D}) \, dV - \omega^2 \int_V \epsilon (\sum_{j=1}^{m} \alpha_j \boldsymbol{w}_j^{3D}) \cdot \boldsymbol{w}_i^{3D} \, dV \\ &+ \int_{\partial V} \nu(\nabla \times \underline{\mathbf{E}}_{\text{curl}}) \times \boldsymbol{w}_i^{3D} \cdot \mathbf{n} \, dA = \int_V \underline{\mathbf{R}} \cdot \boldsymbol{w}_i^{3D} \, dV, \quad i,\ j = 1 \ldots m. \end{aligned} \tag{4.31}$$

Since the coefficients α_j are constant coefficients, they can be taken out of the integrals over V and ∂V [44]

$$\begin{aligned} &\sum_{j=1}^{m} \alpha_j \left(\int_V \nu(\nabla \times \boldsymbol{w}_i^{3D}) \cdot (\nabla \times \boldsymbol{w}_j^{3D}) \, dV - \omega^2 \int_V \epsilon \boldsymbol{w}_i^{3D} \cdot \boldsymbol{w}_j^{3D} \, dV \right) \\ &= \int_V \underline{\mathbf{R}} \cdot \boldsymbol{w}_i^{3D} \, dV - \int_{\partial V} \nu(\nabla \times \underline{\mathbf{E}}_{\text{curl}}) \times \boldsymbol{w}_i^{3D} \cdot \mathbf{n} \, dA, \quad i,\ j = 1 \ldots m. \end{aligned} \tag{4.32}$$

Finally, (4.32) represents a system of equations of the form,

$$\sum_{j=1}^{m} \alpha_j (A_{ij} - \omega^2 B_{ij}) = b_i, \quad i,\ j = 1...m \tag{4.33}$$

with the matrix coefficients

$$A_{ij} = \int_V \nu(\nabla \times \boldsymbol{w}_i^{3D}) \cdot (\nabla \times \boldsymbol{w}_j^{3D}) dV \tag{4.34}$$

$$B_{ij} = \int_V \epsilon \boldsymbol{w}_i^{3D} \cdot \boldsymbol{w}_j^{3D} dV \tag{4.35}$$

and the vector components

$$b_i = \int_V \underline{\mathbf{R}} \cdot \boldsymbol{w}_i^{3D}\, dV - \int_{\partial V} \nu(\nabla \times \underline{\mathbf{E}}_{\mathrm{curl}}) \times \boldsymbol{w}_i^{3D} \cdot \mathbf{n}\, dA,\ i = 1...m. \tag{4.36}$$

The matrix $A_{ij},\ i,j = 1,...,m$ is known as the FEM stiffness matrix and $B_{ij},\ i,j = 1,...,m$ is called the FEM mass matrix [68]. Both matrices are sparsely populated. The 3D vector valued basis functions $\boldsymbol{w}_i^{3D}$ and their rotations $\nabla \times \boldsymbol{w}_i^{3D}$ can be expressed from an unit reference element with the fixed local basis functions $\widehat{\boldsymbol{w}}_i^{3D}$ [70] [72] [77] [55] by the transformations

$$\boldsymbol{w}_i^{3D} = (J_{3D}^{-1})^{\mathrm{T}} \cdot \widehat{\boldsymbol{w}}_i^{3D} \tag{4.37}$$

$$\nabla \times \boldsymbol{w}_i^{3D} = \frac{J_{3D}}{|J_{3D}|} \cdot (\nabla \times \widehat{\boldsymbol{w}}_i^{3D}). \tag{4.38}$$

The entire system of the equations (4.33) can be assembled according to (4.30) - (4.38).

$$\begin{bmatrix} \boldsymbol{A} + \boldsymbol{B} \end{bmatrix} \begin{bmatrix} \boldsymbol{\alpha} \end{bmatrix} = \begin{bmatrix} \boldsymbol{b} \end{bmatrix} \tag{4.39}$$

with the bold letter $\boldsymbol{\alpha}$ denoting the initially unknown weighting coefficient vector. The system of equations (4.39) is created and solved within the MATLAB environment [78]. The obtained divergence-free electric flux density $\underline{\mathbf{D}}_{\mathrm{curl}}$ together with the curl-free electric field strength $\underline{\mathbf{E}}_{\mathrm{div}}$ are used in (4.12) to compute the longitudinal beam coupling impedance according to (4.4).

4.2.3 Boundary Conditions

Considering now the particle beam passing through a cavity with attached cylindrical beam pipes (see Fig. 4.1). Because of the infinite dimension of the beam pipes, the idealized boundary conditions (perfect magnetic conductive (PMC) material and perfect electric conductive (PEC) material) alone are not sufficient to model the entire structure. The electromagnetic field distribution in both beam pipe planes should be computed properly. Otherwise, artificial charges which can lead to an incorrect representation of the boundary conditions will appear. As already stated before, below the cut-off frequency of the beam pipe, the wake fields excited by the particle beam in the beam pipe contribute to the electromagnetic field distributions on the boundary planes. Above the cut-off frequency of the beam pipes, the eigenmodes in the cavity can travel through the beam pipes. Therefore, the wake fields excited by the particle beam as well as the beam pipe modes contribute to the formulation of the boundary conditions. In this thesis, we concentrate on the case when the frequency of the particle beam is below the cut-off frequency of the beam pipe. If the boundary plane is located far away from the cavity, all beam-pipe modes are sufficiently damped and only the fields excited by the particle beam in the beam pipe have to be taken into account at the boundary plane.

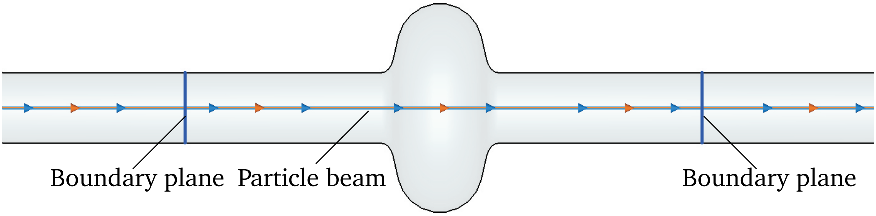

Figure 4.1: A particle beam traversing a cavity with cylindrical beam pipes.

The field distribution of the particle beam in the boundary plane can be determined with the help of a particle beam traversing a cylindrical beam pipe with infinite length. We regard a 2D cut-plane normal to the trajectory of the particle beam as the boundary (port plane) of the beam pipe (see Fig. 4.2). The electromagnetic field distribution on this cut-plane can be applied to define the boundary condition for the 3D solver, such that the appearance of artificial charges on the port planes can be avoided. For this purpose, a two dimensional (2D) FEM solver has been developed to formulate proper boundary conditions for the 3D case.

The electric field distribution in the port plane is given by the solution of the equation (4.11). In the 2D computational domain, the electric potential and tan-

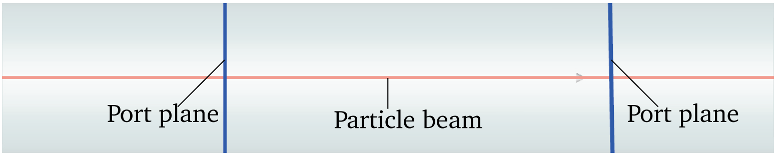

Figure 4.2: A particle beam traversing a cylindrical beam pipe with infinite length.

gential electric strength $\underline{\mathbf{E}}_t$, i.e. $\mathbf{n} \times \underline{\mathbf{E}}$ vanish on the boundary ∂A of the perfect conductive structure (see Fig. 4.3). Thus, the Dirichlet boundary condition i.e. $\Phi = 0$ is applied to the boundary of the structure [79].

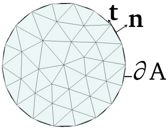

Figure 4.3: 2D computational domain for the 2D FEM solver.

Arising from the equation (4.3), the longitudinal partial derivative operator ∂_z can be replaced by the operator $-\jmath\omega/\beta c_0$ for the computation on a 2D cut-plane in an infinitely long structure. Therefore, the electric field strength $\underline{\mathbf{E}}$ can be split into transverse and longitudinal components [80],

$$\underline{\mathbf{E}} = \begin{pmatrix} \mathbf{E}_\perp \\ \mathrm{E}_z \end{pmatrix} \tag{4.40}$$

where $\mathbf{E}_\perp$ is the transverse electric field and E_z represents the longitudinal component of $\underline{\mathbf{E}}$. For a proper approximation of the electric field strength, the well-known 2D Nédélec edge elements are used for the transverse vector $\mathbf{E}_\perp$, while the 2D nodal elements are used to describe the longitudinal component of E_z [56]. Due to the divergence-free lowest order Nédélec edge elements, the electric field strength $\underline{\mathbf{E}}$ in (4.40) can be calculated separately by Helmholtz split (4.12) and (4.14) [67]. By inserting (4.14) into Gauss's law, the Poisson equation (4.13) with the Dirichlet boundary condition, i.e. $\Phi = 0$ on ∂A, is obtained. Afterwards, the curl-curl equation (4.15) with the Dirichlet boundary condition, i.e. $\mathbf{n} \times \underline{\mathbf{E}} = 0$ on ∂A, in 2D computational domain can be derived. After solving the system of equations, the obtained electric field strength $\underline{\mathbf{E}}$ is used to formulate the boundary conditions for the 3D computation.

4.2.3.1 Poisson Solver

The scalar potential $\underline{\Psi}$ on a 2D cut-plane in Fig. 4.3 can be expressed in the cylindrical coordinate system

$$\underline{\Psi}(\varrho,\ \varphi,\ z)\ =\ \underline{\Phi}(\varrho,\ \varphi)e^{-\jmath\omega z/\beta c_0} \tag{4.41}$$

where ϱ is the radial coordinate, φ the azimuth angle, and z the longitudinal coordinate. Obviously, the potential $\underline{\Psi}$ is independent of azimuth angle φ for a rotationally symmetric structure. For linear isotropic materials, equation (4.14) can be expressed in cylindrical coordinates as

$$\frac{1}{\varrho}\frac{\partial}{\partial\varrho}\left(\varrho\frac{\partial\underline{\Psi}}{\partial\varrho}\right)+\frac{1}{\varrho^2}\frac{\partial^2\underline{\Psi}}{\partial\varphi^2}+\frac{\partial^2\underline{\Psi}}{\partial z^2}\ =\ -\frac{\rho}{\epsilon}e^{-\jmath\omega z/\beta c_0} \tag{4.42}$$

with $\rho=\frac{1}{\beta c_0}\sigma$. Insertion of (4.41) into (4.42) leads to ordinary differential equation

$$\frac{\partial^2\underline{\Phi}}{\partial\varrho^2}+\frac{1}{\varrho}\frac{\partial\underline{\Phi}}{\partial\varrho}-\frac{\omega^2}{\beta^2c_0^2}\underline{\Phi}\ =\ -\frac{\rho}{\epsilon} \tag{4.43}$$

The scalar potential $\underline{\Phi}$ can be approximated

$$\underline{\Phi}(x,y)\ =\ \sum_{j=1}^{m}c_jN_j^{2D}(x,y) \tag{4.44}$$

by using nodal elements with the weighting coefficients c_j and the 2D scalar-valued basis functions N_j^{2D}. Insertion of (4.44) into the formulation (4.43) and application of the standard Galerkin's procedure together with the Dirichlet boundary condition leads to the discrete Poisson formulation

$$\sum_{j=1}^{m}c_j\left(S_{ij}^{2D}\ +\ M_{ij}^{2D}\right)\ =\ \int_A\frac{\rho}{\epsilon}N_i^{2D}dA \tag{4.45}$$

with a vanishing boundary term. The stiffness and mass matrices

$$S_{ij}^{2D}\ =\ \int_A\nabla N_i^{2D}\cdot\nabla N_j^{2D}dA \tag{4.46}$$

$$M_{ij}^{2D} = -\frac{\omega^2}{\beta^2 c_0^2} \int_A N_i^{2D} N_j^{2D} dA \tag{4.47}$$

have to be computed within the 2D computational domain A with the help of integration by using 2D Gauss quadrature rules [69].

The 2D-scalar valued basis functions N_i^{2D} as well as the gradients ∇N_i^{2D} can be expressed from an unit reference element with the known local basis functions $\widehat{N}_i^{2D}$ [70] [71] [72] by the transformations

$$N_i^{2D} = \widehat{N}_i^{2D} \tag{4.48}$$

$$\nabla N_i^{2D} = (J_{2D}^{-1})^{\mathrm{T}} \cdot \nabla \widehat{N}_i^{2D} \tag{4.49}$$

The entire system of the equations (4.45) can be assembled according to (4.46) - (4.49) and result in

$$\left[\; \boldsymbol{S}^{2D} + \boldsymbol{M}^{2D} \; \right] \left[\; \boldsymbol{c} \; \right] = \left[\; \frac{\underline{\rho}}{\epsilon} \; \right] \tag{4.50}$$

with the bold small letter **c** denoting the weighting coefficient vector.

After solving the linear equation (4.50), the electric potential $\underline{\Psi}$ can be obtained by (4.41) and will be used as the Dirichlet boundary condition to formulate the boundary term $B_{\epsilon,ij}$ in the 3D Poisson equation (4.17). Additionally, the curl-free electric field strength $\underline{\mathbf{E}}_{\mathrm{div}}$ can be calculated by (4.14). The partial derivative operator ∂z can be replaced by the operator $-\jmath\omega/\beta c_0$, such that the entire operator ∇ can be expressed as $\nabla = (\partial x,\ \partial y,\ -\jmath\omega/\beta c_0)^{\mathrm{T}}$.

4.2.3.2 Curl-Curl Solver

Let us firstly consider the curl-operator acting on a field, which can be spitted in longitudinal and transverse components. An elegant formulation of this curl-operator can be given by the following matrix operator equation [81]

$$\nabla \times \underline{\mathbf{E}} = \left(\begin{array}{cc|c} 0 & -\partial z & \partial y \\ \partial z & 0 & -\partial x \\ \hline -\partial y & \partial x & 0 \end{array} \right) \left(\begin{array}{c} \mathbf{E}_{\perp} \\ \mathrm{E}_z \end{array} \right) = \left(\begin{array}{cc} \jmath\hat{Z} & \hat{A} \\ \hat{B} & 0 \end{array} \right) \left(\begin{array}{c} \mathbf{E}_{\perp} \\ \mathrm{E}_z \end{array} \right) \tag{4.51}$$

where $\hat{A} = (\partial y,\ -\partial x)^{\mathrm{T}}$ and $\hat{B} = (-\partial y,\ \partial x)$ denote the two-dimensional scalar and vector operator, respectively. Obviously they have the following relationship [82]

$$\hat{A} = -\hat{B}^{\mathrm{T}} \tag{4.52}$$

The operator $\hat{Z}$ has the form

$$\hat{Z} = \begin{pmatrix} 0 & \frac{\omega}{\beta c_0} \\ -\frac{\omega}{\beta c_0} & 0 \end{pmatrix} \tag{4.53}$$

$$\text{with} \quad \hat{\mathrm{Z}}^2 = \begin{pmatrix} -\frac{\omega^2}{\beta^2 c_0^2} & 0 \\ 0 & -\frac{\omega^2}{\beta^2 c_0^2} \end{pmatrix} = -\frac{\omega^2}{\beta^2 c_0^2}\hat{\mathrm{I}} \tag{4.54}$$

where $\hat{\mathrm{I}}$ is the unit matrix of size 2. Then, the first curl-curl term on the left side of (4.15) can be rewritten as

$$\nabla \times \nu \nabla \times \underline{\mathbf{E}}_{\text{curl}} = \begin{pmatrix} \hat{A}\nu\hat{B} - \nu\hat{Z}^2 & \jmath\hat{Z}\nu\hat{A} \\ \jmath\hat{B}\nu\hat{Z} & \hat{B}\nu\hat{A} \end{pmatrix} \begin{pmatrix} \mathbf{E}_\perp \\ \mathrm{E}_z \end{pmatrix} \tag{4.55}$$

Herein, the vector-valued basis functions $\boldsymbol{w}_i^{2D}$ are applied for an approximation of the transverse electric field $\mathbf{E}_\perp$, while the scalar-valued basis functions N_i^{2D} are used to approximate the longitudinal electric field component in the form.

$$\mathbf{E}_\perp(x,y) = \sum_{j=1}^{m} e_j^\perp \boldsymbol{w}_j^{2D}(x,y) \tag{4.56}$$

$$\mathrm{E}_z(\mathrm{x},\mathrm{y}) = \sum_{j=1}^{m} e_j^z N_j^{2D}(x,y) \tag{4.57}$$

where $e_j^\perp$ and e_j^z are the scalar weighting coefficients. Insertion of (4.56) and (4.57) into the formulation (4.55) and application of the standard Galerkin's procedure leads to the discrete curl-curl formulation in the 2D computational domain,

$$\left[\ \boldsymbol{S}_{\text{curlcurl}}^{2D} + \boldsymbol{M}_{\text{curlcurl}}^{2D}\ \right]\left[\ \boldsymbol{e}_{\text{curlcurl}}\ \right] = \left[\ \mathbf{R}^{2D}\ \right] \tag{4.58}$$

with the solution vector

$$\boldsymbol{e}_{\text{curlcurl}} = \begin{pmatrix} \boldsymbol{e}^\perp \\ \boldsymbol{e}^z \end{pmatrix} \tag{4.59}$$

where $\boldsymbol{e}^\perp$ and $\boldsymbol{e}^z$ denote the weighting coefficient vectors for the vector and scalar basis functions, respectively. According to (4.55), the stiffness matrix $\boldsymbol{S}_{\text{curlcurl}}^{2D}$ can be decomposed as

$$\boldsymbol{S}^{2D}_{\text{curlcurl}} = \begin{pmatrix} \boldsymbol{S}_{\perp\perp} & \boldsymbol{S}_{\mathrm{Z}\perp} \\ \boldsymbol{S}_{\perp\mathrm{Z}} & \boldsymbol{S}_{\mathrm{ZZ}} \end{pmatrix} \tag{4.60}$$

where the individual terms can be written as

$$\begin{aligned}
(S_{\perp\perp})_{ij} &= \int_A \left[(\hat{A}\nu\hat{B}\boldsymbol{w}_i^{2D})\cdot\boldsymbol{w}_j^{2D} - (\nu\hat{Z}^2\boldsymbol{w}_i^{2D})\cdot\boldsymbol{w}_j^{2D} \right] dA && (4.61)\\
(S_{\mathrm{Z}\perp})_{ij} &= \int_A (\hat{Z}\nu\hat{A}N_i^{2D})\cdot\boldsymbol{w}_j^{2D}\, dA && (4.62)\\
(S_{\perp\mathrm{Z}})_{ij} &= \int_A (\hat{B}\nu\hat{Z}\boldsymbol{w}_i^{2D})N_j^{2D}\, dA && (4.63)\\
(S_{\mathrm{ZZ}})_{ij} &= \int_A (\hat{B}\nu\hat{A}N_i^{2D})N_j^{2D}\, dA. && (4.64)
\end{aligned}$$

We use the following identity [54]

$$\int_A (\hat{B}\boldsymbol{u})\psi\, dA = \int_A (\hat{A}\psi)\boldsymbol{u}\, dA + \int_{\partial A} (\boldsymbol{u}\cdot\mathbf{t})\psi\, ds \tag{4.65}$$

with functions ψ: A $\rightarrow$ $\mathbb{R}$, $\boldsymbol{u}$: A $\rightarrow$ $\mathbb{R}^2$ and a tangential unit vector $\mathbf{t}$ on the boundary to transform the second order operators $\hat{A}\nu\hat{B}$, $\hat{B}\nu\hat{A}$ and the divergence operator $\hat{B}\nu\hat{Z}$. They can be rewritten as

$$\begin{aligned}
\int_A (\hat{A}\nu\hat{B}\boldsymbol{w}_i^{2D})\cdot\boldsymbol{w}_j^{2D}\, dA &= \int_A (\nu\hat{B}\boldsymbol{w}_i^{2D})(\hat{B}\boldsymbol{w}_j^{2D})\, dA - \int_{\partial A} (\nu\hat{B}\boldsymbol{w}_i^{2D}\cdot\mathbf{t})\boldsymbol{w}_j^{2D}\, ds && (4.66)\\
\int_A (\hat{B}\nu\hat{A}N_i^{2D})N_j^{2D}\, dA &= \int_A (\nu\hat{A}N_i^{2D})(\hat{A}N_j^{2D})\, dA + \int_{\partial A} (\nu\hat{A}N_i^{2D}\cdot\mathbf{t})N_j^{2D}\, ds && (4.67)\\
\int_A (\hat{B}\nu\hat{Z}\boldsymbol{w}_i^{2D})N_j^{2D}\, dA &= \int_A (\nu\hat{Z}\boldsymbol{w}_i^{2D})(\hat{A}N_j^{2D})\, dA + \int_{\partial A} (\nu\hat{Z}\boldsymbol{w}_i^{2D}\cdot\mathbf{t})N_j^{2D}\, ds && (4.68)
\end{aligned}$$

with vanishing boundary terms in case of PEC boundary condition. Afterwards, equations (4.61), (4.63) and (4.64) can be formulated as

$$(S_{\perp\perp})_{ij} = \int_A \left[(\nu\hat{B}\boldsymbol{w}_i^{2D})(\hat{B}\boldsymbol{w}_j^{2D}) - (\nu\hat{Z}^2\boldsymbol{w}_i^{2D})\cdot\boldsymbol{w}_j^{2D} \right] dA \tag{4.69}$$

$$
\begin{aligned}
(S_{\perp \mathrm{Z}})_{ij} &= \int_A (\nu \hat{Z} \boldsymbol{w}_i^{2D}) \cdot (\hat{A} N_j^{2D}) dA & (4.70)\\
(S_{\mathrm{ZZ}})_{ij} &= \int_A (\nu \hat{A} N_i^{2D}) \cdot (\hat{A} N_j^{2D}) dA. & (4.71)
\end{aligned}
$$

The mass matrix $\boldsymbol{M}_{\mathrm{curlcurl}}^{2D}$ can be decomposed as

$$
\boldsymbol{M}_{\mathrm{curlcurl}} = \begin{pmatrix} \boldsymbol{M}_{\perp\perp} & 0 \\ 0 & \boldsymbol{M}_{\mathrm{ZZ}} \end{pmatrix} \tag{4.72}
$$

where the contributing read

$$
\begin{aligned}
(M_{\perp\perp})_{ij} &= -\omega^2 \int_A \epsilon \boldsymbol{w}_i^{2D} \cdot \boldsymbol{w}_j^{2D} dA & (4.73)\\
(M_{\mathrm{ZZ}})_{ij} &= -\omega^2 \int_A \epsilon N_i^{2D} N_j^{2D} dA. & (4.74)
\end{aligned}
$$

The vector for the source $\mathbf{R}_{\mathrm{curlcurl}}$ can be given with

$$
\mathbf{R}^{2D} = \begin{pmatrix} \mathbf{R}_{\perp} \\ \mathbf{R}_{\mathrm{Z}} \end{pmatrix} \tag{4.75}
$$

where the vector terms can be written as

$$
\begin{aligned}
(R_{\perp})_i &= \int_A \left(\jmath \omega \mathbf{J}_{\perp} - \omega^2 \epsilon \mathbf{E}_{\mathrm{div},\perp} \right) \cdot \boldsymbol{w}_i^{2D} dA & (4.76)\\
(R_{\mathrm{Z}})_i &= \int_A \left(\jmath \omega \mathrm{Jz} - \omega^2 \epsilon \mathrm{E}_{\mathrm{div},\mathrm{z}} \right) N_i^{2D} dA. & (4.77)
\end{aligned}
$$

The 2D scalar-vector basis functions N_i^{2D} can be given by equations (4.48) and (4.49). The 2D vector-valued basis functions w_i^{2D} and the rotations $\nabla \times w_i^{2D}$ can be expressed from an unit reference element with the local basis functions $\widehat{\boldsymbol{w}}_i^{2D}$ [70] [72] [77] by the transformations

$$
\begin{aligned}
w_i^{2D} &= (J^{-1})^{\mathrm{T}} \widehat{\boldsymbol{w}}_i^{2D} & (4.78)\\
\nabla \times w_i^{2D} &= \frac{1}{|J|} \nabla \times \widehat{\boldsymbol{w}}_i^{2D} & (4.79)
\end{aligned}
$$

After solving the system of the equations (4.58), the obtained divergence-free electric flux density ($\epsilon\underline{\mathbf{E}}_{\text{curl}}$) together with the curl-free electric field strength $\underline{\mathbf{E}}_{\text{div}}$ are used as proper boundary conditions [45] to determine the boundary contribution, i.e. $\int_{\partial V} \nu(\nabla \times \underline{\mathbf{E}}) \times \boldsymbol{w}_i^{3D} \cdot \mathbf{n}\, dA$, for the 3D impedance computation.

4.2.3.3 Benchmark Example

In order to validate the 2D FEM solver, an analytical accessible benchmark example is evaluated. Since the electric field strength $\underline{\mathbf{E}}$ on a 2D cut-plane can be obtained by using a 2D FEM solver, the longitudinal space charge impedance for a uniform circular beam with radius $a = 1$ cm in a homogeneous perfectly conductive cylindrical beam pipe with radius $b = 4$ cm and length $l = 1$ m (see Fig. 4.1) can be computed by (4.4) for arbitrary frequency and beam velocity.

On the other hand, this longitudinal space charge impedance can be computed analytically and is given by [26]

$$\underline{Z}_{||}(\omega) = \frac{-jl}{\pi a^2 \omega \epsilon_0} \left[1 - 2I_1^2(\frac{\omega}{\beta\gamma c_0}a) \left(K_1(\frac{\omega}{\beta\gamma c_0}a) + \frac{K_0(\frac{\omega}{\beta\gamma c_0}b)}{I_0(\frac{\omega}{\beta\gamma c_0}b)} I_1(\frac{\omega}{\beta\gamma c_0}a) \right) \right] \tag{4.80}$$

with $\gamma = \frac{1}{\sqrt{1-\beta^2}}$, where I_0 and K_0 are the 0th-order modified Bessel functions of the first and second kind, respectively. The symbols I_1 and K_1 represent the 1st-order modified Bessel functions of the first and second kind, respectively.

Fig. 4.4 and Fig. 4.5 show the obtained numerical results from the 2D FEM solver, the analytical results as well as the logarithmic relative differences from the numerical and analytical results. The logarithmic relative difference is calculated as

$$\text{relative difference} = \log_{10} \frac{|\mathrm{Z}_{||,\text{num}} - \mathrm{Z}_{||,\text{ana}}|}{\mathrm{Z}_{||,\text{ana}}} \tag{4.81}$$

The results from Fig. 4.4 and Fig. 4.5 indicate that the 2D FEM solver is applicable to a very wide frequency range from kHz to PHz at arbitrary beam velocity. With increasing number of triangular mesh cells, the difference between the obtained numerical calculation and the analytical results become smaller and a relative difference in the order of 10^{-2} is obtained on the specified meshes.

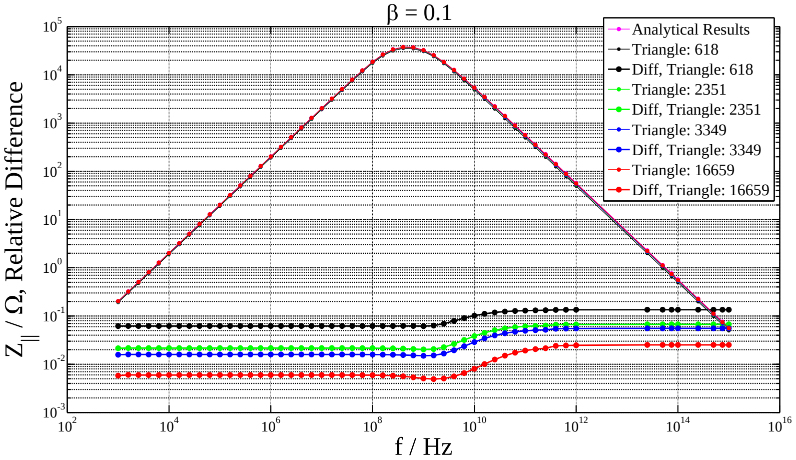

Figure 4.4: Longitudinal space charge impedance for $\beta = 0.1$ and the relative difference between the obtained numerical calculation and the analytical results.

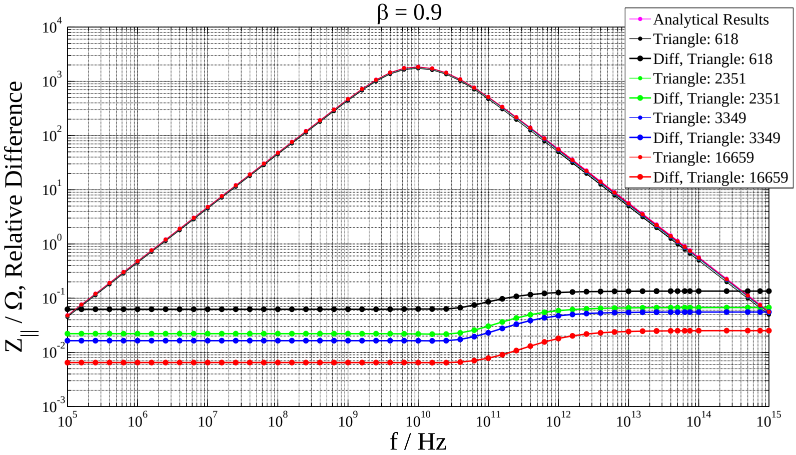

Figure 4.5: Longitudinal space charge impedance for $\beta = 0.9$ and the relative difference between the obtained numerical calculation and the analytical results.

4.2.4 Implementation

A descriptive sketch of the algorithm to calculate the longitudinal beam coupling impedance is given in the following overview:

Algorithm 1 Computation of the longitudinal beam coupling impedance

```
1: Geometric modeling of the 3D structure using the tetrahedral elements within
   CST MICROWAVE STUDIO [9]
2: Pass the mesh information to the FEM programm by means of ASCII and binary
   file transfer
3: Read the 3D stiffness and mass matrices assembled by the CEM3D solver
4: Extract the surface mesh information on the boundary of the structure
5: Setup the stiffness, mass matrices and source vector for 2D Poisson solver
6: Solve the 2D Poisson solver and calculate the $\underline{\mathbf{E}}_{\text{div}}$ components
7: Setup the stiffness, mass matrices and source vector for 2D Curl-Curl solver
8: Solve the 2D Curl-Curl solver and calculate the $\underline{\mathbf{E}}_{\text{curl}}$ components
9: Setup the stiffness, mass matrices and source vector for 3D Poisson solver
10: Solve the 3D Poisson solver and calculate the $\underline{\mathbf{E}}_{\text{div}}$ components
11: Calculate $\nabla \times \underline{\mathbf{E}}_{\text{curl}}$ on the boundary of the structure
12: Setup the vector $\boldsymbol{b}$ for the 3D Curl-Curl problem in (4.39)
13: Solve the 3D Curl-Curl problem and calculate the $\underline{\mathbf{E}}_{\text{curl}}$
14: Determine the total $\underline{\mathbf{E}}$ and the longitudinal beam coupling impedance $\underline{Z}_{||}$
```

The geometric modeling of the structure with the tetrahedral meshing is performed by CST MICROWAVE STUDIO [9]. Then, the mesh information is passed to the FEM program by means of ASCII and binary file transfer. In step 3, the 3D stiffness and mass matrices in equation (4.39) can be obtained directly from the CEM3D solver [47]. In order to describe the boundary conditions properly, the surface mesh information on the boundary of the structure is extracted and applied to set up the 2D Poisson and Curl-Curl solver. From the solutions of the 2D FEM solvers, the electric potential on the boundary is applied as Dirichlet boundary condition to describe the boundary terms in equation (4.17). Furthermore, the rotations of the electric field on the boundary can be determined and transfered as proper boundary condition to the 3D computational FEM solver by ASCII file to formulate the boundary terms in equation (4.36). The entire 2D and 3D FEM computations are implemented within MATLAB [78].

The 3D FEM solver is benchmarked for a uniform cylindrical (PEC) beam pipe with radius $b = 4$ cm and a length of $l = 0.02$m. Fig. 4.6 shows the obtained numerical results from the 3D FEM solver as well as the analytical results. Since the electric field is separately calculated by Helmholtz split, the longitudinal space charge impedance can be split into the divergence part Z_{div} and the curl part Z_{curl}.

The results from Fig. 4.6 indicate that at the relativistic velocity $\beta = 0.1$, the 3D FEM solver is inapplicable to calculate the space charge impedance in the beam pipe. The inaccurate and unsmooth curl part Z_{curl} leads to the improper longitudinal space charge impedance $Z_{||}$. The reason for the incorrect curl part Z_{curl} have to be investigated carefully.

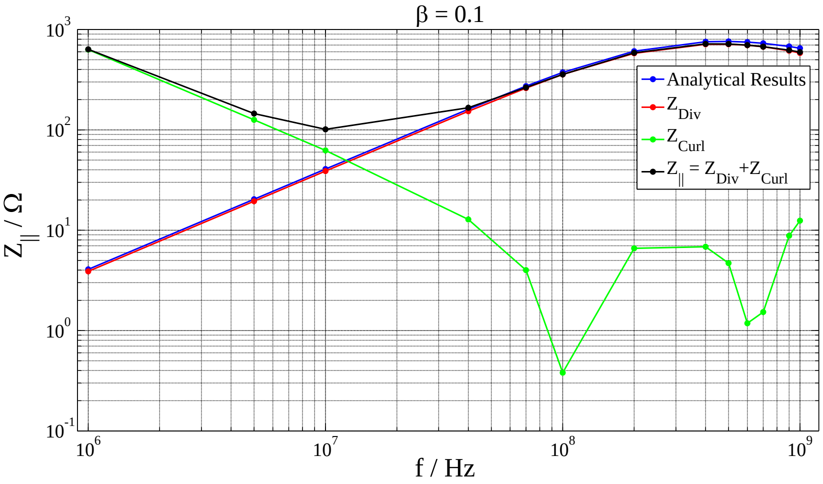

Figure 4.6: Longitudinal space charge impedance ($Z_{||} = Z_{\text{div}} + Z_{\text{curl}}$) for $\beta = 0.1$ together with its divergence part (Z_{div}) and curl part (Z_{curl}). The calculations are performed using 18853 first-order tetrahedral elements.

Although we cannot obtain the analytical solution of the electric field from the equation (4.15), the numerical reference electric field distribution in the uniform cylindrical beam pipe (see Fig. 4.7) can be obtained from the 2D FEM solver by using

$$\underline{E}(\varrho, \varphi, z) = \underline{E}_{2D}(\varrho, \varphi) e^{-j\omega z/\beta c_0} \tag{4.82}$$

where $\underline{\mathrm{E}}_{2D}$, which is calculated by the 2D FEM solver, describes the electric field distribution in an arbitrary cutplane within the structure. The coordinate z is the longitudinal distance from the arbitrary position inside the beam pipe to this boundary plane.

Fig. 4.8 shows the numerical results obtained from the 3D FEM solver. Compared to the reference results in Fig. 4.7, the electric fields in Fig. 4.8 are irregularly distributed. Moreover, the magnitude of the electric fields are much larger.

As already stated, the vectors on the right hand of the system equations (4.33) are composed of three parts: The current density $\underline{\mathbf{J}}$, the curl-free electric field $\underline{\mathbf{E}}_{\mathrm{div}}$ from the Poisson equation and the boundary term $(\nabla \times \underline{\mathrm{E}})$ from the 2D FEM solver. According to the property of the system equations, the entire solution $\mathbf{E}_{\mathrm{curl}}$ to the system (4.33) can be expressed by

$$\mathbf{E}_{\mathrm{curl}} = \mathbf{E}_{\mathrm{J}} + \mathbf{E}_{\mathrm{divP}} + \mathbf{E}_{\mathrm{BC}} \tag{4.83}$$

where $\mathbf{E}_{\mathrm{J}}$ is the solution to the system with only $\underline{\mathbf{J}}$ part, $\mathbf{E}_{\mathrm{divP}}$ the solution to the system with only $\underline{\mathbf{E}}_{\mathrm{div}}$ part, and $\mathbf{E}_{\mathrm{BC}}$ the solution to the system with $\nabla \times \underline{\mathbf{E}}$ part. The excitation source is an uniform cylindrical beam with radius $a = 1$ cm and its current density $\underline{\mathbf{J}}$ in frequency domain is defined by (4.3) together with (4.1). From the solution of each part we can find the reason for the inaccurate results.

Fig. 4.9 and Fig. 4.10 illustrate the numerical reference results obtained from 2D FEM solver. Fig. 4.9 corresponds to the $\mathbf{E}_{\mathrm{J}}$ part, while Fig. 4.10 corresponds to the $\mathbf{E}_{\mathrm{divP}}$ part. For the 2D FEM solver, the boundary part $\mathbf{E}_{\mathrm{BC}}$ vanishes. The results in Fig. 4.9 and Fig. 4.10 indicate that the magnitude of the electric field $\mathbf{E}_{\mathrm{J}}$ and $\mathbf{E}_{\mathrm{BC}}$ is almost equal. But the electric fields between the two parts point to the opposite direction. For this reason, the entire Electric field $\mathbf{E}_{\mathrm{curl}}$ is quite weak, which can be noticed in Fig. 4.7.

Fig. 4.11, Fig. 4.12 and Fig. 4.13, where the results are obtained from the 3D FEM solver, correspond to the $\mathbf{E}_{\mathrm{J}}$, $\mathbf{E}_{\mathrm{divP}}$ and $\mathbf{E}_{\mathrm{BC}}$, respectively. Compared to the results in Fig. 4.10, the results in Fig. 4.13 indicate the almost equal distribution and magnitude of the electric fields. Furthermore, it can be noticed that the magnitude of the electric fields in Fig. 4.11 and Fig. 4.12 is almost equal, while the electric fields between them point to the opposite direction.

The sum of $\mathbf{E}_{\mathrm{J}}$ and $\mathbf{E}_{\mathrm{BC}}$ $(\mathbf{E}_{\mathrm{J}} + \mathbf{E}_{\mathrm{BP}})$ are plotted in Fig. 4.14. According to the equation (4.83) and the reference results in Fig. 4.10, the electric fields in Fig. 4.14 should have an almost equal magnitude and should point in the opposite direction compared to $\mathbf{E}_{\mathrm{divP}}$ in Fig. 4.13. Fig. 4.14c and Fig. 4.14d indicate the incorrect results. The magnitude of the imaginary part of the electric field is much larger. In addition, the electric fields are irregularly distributed. The reason for the incorrect results is the numerical accuracy from the FEM algorithm.

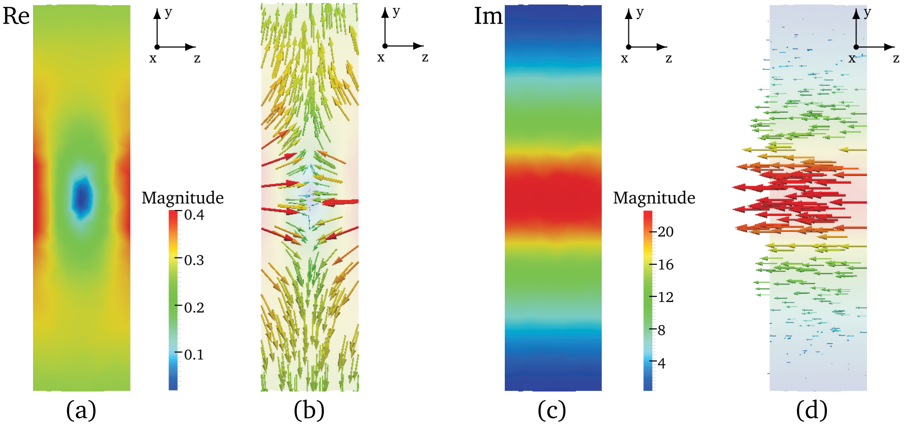

(a) (b) (c) (d)

Figure 4.7: The electric field distribution in a uniform cylinder beam pipe with the length of $l = 0.02$ m. (a) The magnitude of the real part of the electric field. (b) The real part of the electric field in vector plots. (c) The magnitude of the imaginary part of the electric field. (d) The imaginary part of the electric field in vector plots. The calculations are performed with 513 triangles by 2D FEM solver.

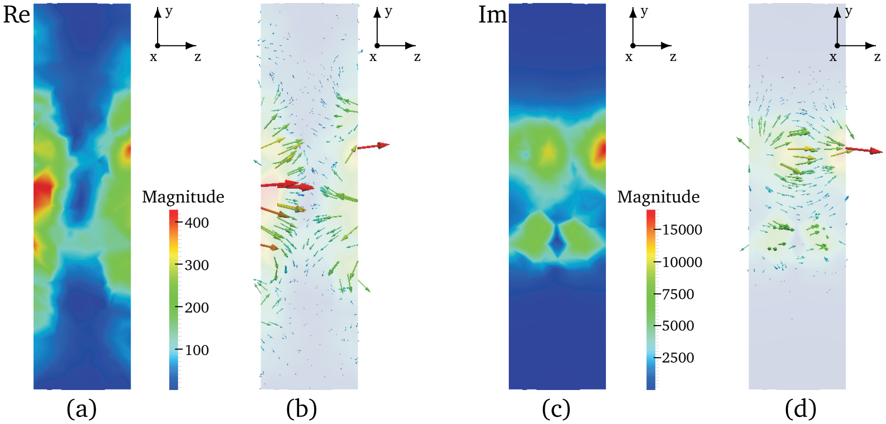

(a) (b) (c) (d)

Figure 4.8: The electric field distribution in a uniform cylinder beam pipe with the length of $l = 0.02$ m. (a) The magnitude of the real part of the electric field. (b) The real part of the electric field in vector plots. (c) The magnitude of the imaginary part of the electric field. (d) The imaginary part of the electric field in vector plots. The calculations are performed with 18583 tetrahedrons by 3D FEM solver.

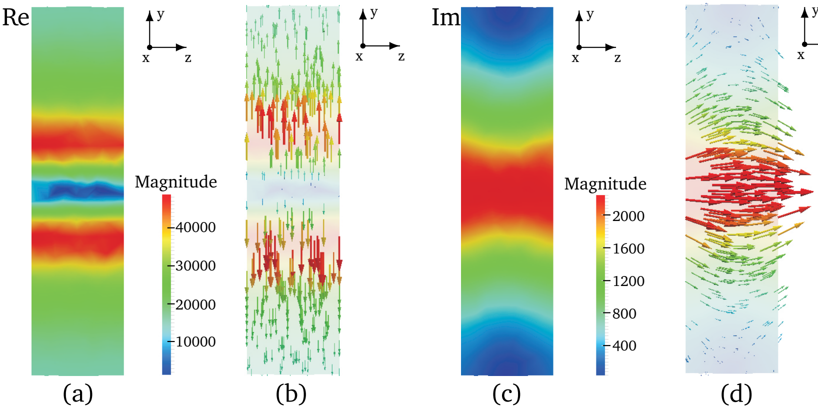

Figure 4.9: The electric field distribution obtained from the $\mathrm{E_J}$ part in a uniform cylinder beam pipe. (a) The magnitude of the real part of the electric field. (b) The real part of the electric field in vector plots. (c) The magnitude of the imaginary part of the electric field. (d) The imaginary part of the electric field in vector plots. The calculations are performed with 531 triangles by 2D FEM solver.

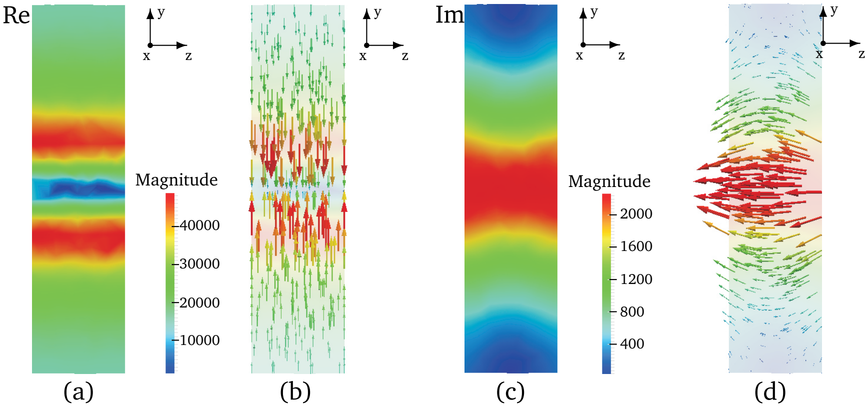

Figure 4.10: The electric field distribution from the $\mathrm{E_{divP}}$ part in a uniform cylinder beam pipe. (a) The magnitude of the real part of the electric field. (b) The real part of the electric field in vector plots. (c) The magnitude of the imaginary part of the electric field. (d) The imaginary part of the electric field in vector plots. The calculations are performed 531 triangles by 2D FEM solver.

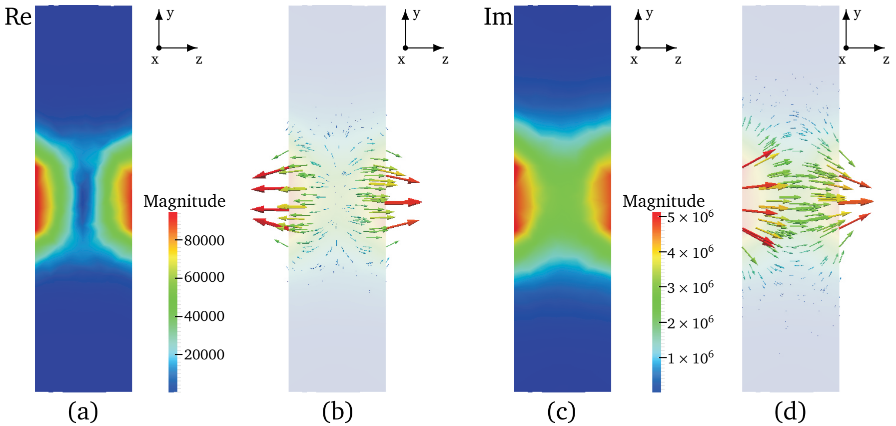

Figure 4.11: The electric field distribution from the $\mathbf{E}_\mathrm{J}$ part in a uniform cylinder beam pipe. (a) The magnitude of the real part of the electric field. (b) The real part of the electric field in vector plots. (c) The magnitude of the imaginary part of the electric field. (d) The imaginary part of the electric field in vector plots. The calculations are performed with 18583 tetrahedrons by 3D FEM solver.

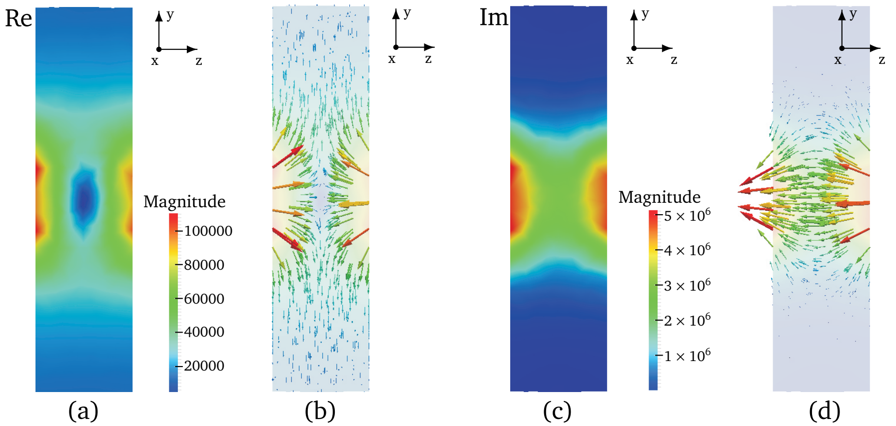

Figure 4.12: The electric field distribution from the $\mathbf{E}_\mathrm{BP}$ part in a uniform cylinder beam pipe. (a) The magnitude of the real part of the electric field. (b) The real part of the electric field in vector plots. (c) The magnitude of the imaginary part of the electric field. (d) The imaginary part of the electric field in vector plots. The calculations are performed with 18583 tetrahedrons by 3D FEM solver.

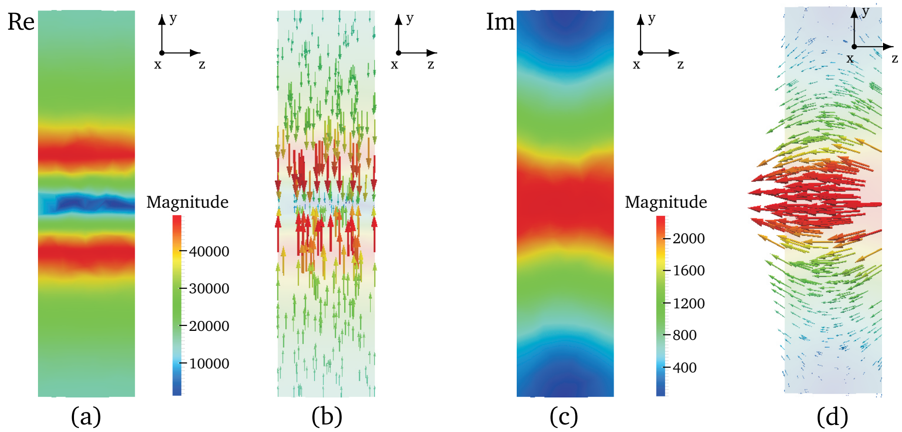

Figure 4.13: The electric field distribution from the $\mathbf{E}_{\mathrm{divP}}$ part in a uniform cylinder beam pipe. (a) The magnitude of the real part of the electric field. (b) The real part of the electric field in vector plots. (c) The magnitude of the imaginary part of the electric field. (d) The imaginary part of the electric field in vector plots. The calculations are performed with 18583 tetrahedrons by 3D FEM solver.

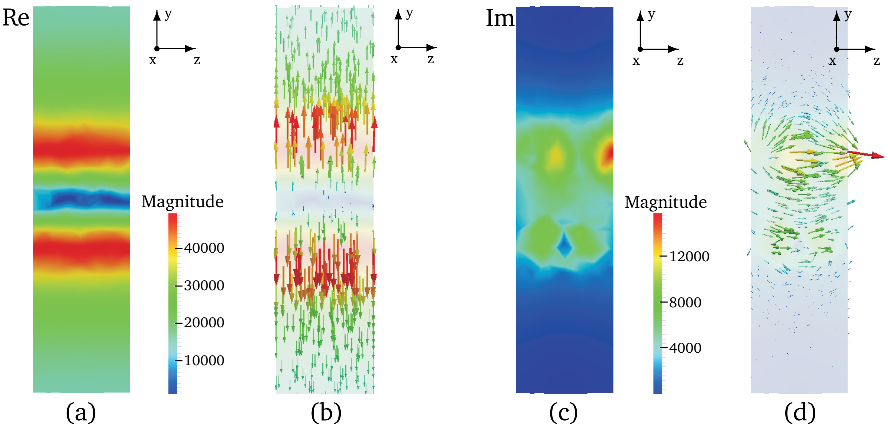

Figure 4.14: The electric field distribution from the sum of $\mathbf{E}_{\mathrm{J}}$ and $\mathbf{E}_{\mathrm{BP}}$ ($\mathbf{E}_{\mathrm{J}} + \mathbf{E}_{\mathrm{BP}}$) in a uniform cylinder beam pipe. (a) The magnitude of the real part of the electric field. (b) The real part of the electric field in vector plots. (c) The magnitude of the imaginary part of the electric field. (d) The imaginary part of the electric field in vector plots. The calculations are performed with 18583 tetrahedrons by 3D FEM solver.

In order to formulate the boundary condition, the field distributions are required for the surface integral over the triangles on the boundary of the beam pipe, while the other two terms for b_i in (4.33) are the volume integral over the tetrahedrons in the beam pipe. But the triangles on both boundary planes are not able to match the long homogeneous tetrahedrons correctly, such that a non-negligible numerical error arises and results in the incorrect $\mathbf{E}_{\text{curl}}$. In Fig. 4.11 and Fig. 4.12, the magnitude of $\mathbf{E}_{\text{J}}$ and $\mathbf{E}_{\text{BC}}$ is up to 5×10^6, while the magnitude of $\mathbf{E}_{\text{divP}}$ in Fig. 4.13 is up to 2×10^3. Therefore, for $\mathbf{E}_{\text{J}}$ and $\mathbf{E}_{\text{BC}}$ the relative error in order of at least 10^{-3} is required to get the accurate $\mathbf{E}_{\text{curl}}$ according to the equation (4.83). However, as shown in Fig. 4.5 and Fig. 4.6, with a extremely high mesh resolution (16659 triangles) a relative difference in order of 10^{-2} is present. Hence a very large number of tetrahedrons is required to achieve the relative error in order of 10^{-3} for $\mathbf{E}_{\text{J}}$ and $\mathbf{E}_{\text{BC}}$. It will lead to a extremely time-consuming and impractical numerical calculation work. For this reason, another efficient 3D algorithm should be developed to calculate the broadband impedance in the accelerating resonator properly.

5 Computation of the Narrow-band Impedance in Acceleration Resonators

As mentioned in chapter 1, the parasitic higher-order modes (HOMs) in the resonant cavity can lead to particle beam instabilities. For this reason, during the design phase of superconducting radio frequency (RF) accelerating cavities a challenging and difficult work is to determine the electromagnetic field distribution as well as the narrow-band impedance (shunt impedance) of HOMs inside the structure with the help of proper computer simulation. At the Computational Electromagnetics Laboratory (TEMF), two numerical eigenmode solvers for the calculations of the eigenmodes for the resonant cavity are available, one is based on real-valued analysis, which describes the entire electromagnetic field in the lossless acceleration structure, the other eigenmode solver is complex-valued to suitable for describing the dissipative acceleration structure. Both eigenmode solvers have been applied to the superconducting radio frequency (RF) accelerating cavities to determine the resonance frequency, the corresponding field distribution and the narrow-band impedance (shunt impedance) of eigenmodes.

5.1 Computation of the Shunt Impedance in the Superconducting Proton Linac (SPL) cavity

Firstly the real-valued eigenmode solver has been used to calculate the shunt impedance of eigenmodes in the Superconducting Proton Linac (SPL) cavity. The Superconducting Proton Linac (SPL) cavity is mainly designed and conducted by CERN and uses two families ($\beta = 0.65$ and $\beta = 1$) of elliptical five cell superconducting cavities. Both families operate at 704.4 MHz [83]. It is a part of the planned injector upgrade of the Large Hadron Collider (LHC). The SPL cavity is used to accelerate the ion beam from 160 MeV to 5GeV and served as a driver for neutrino facilities and radioactive beam facilities. The real-valued eigenmode solver can be run by using Finite Integration Technique (FIT) and Finite Element Method (FEM). In a two step process, the modeling and the field simulation of the

SPL cavity is done, afterwards the normalized shunt impedance (R/Q) can be computed from the acquired resonance frequency and corresponding field distribution of eigenmodes.

5.1.1 Field Simulation in Frequency Domain by Using Finite Integration Technique

For the field simulation by using Finite Integration Technique (FIT) the SPL cavity is modeled by CST MICROWAVE STUDIO® (CST MWS) [9]. The SPL cavity is composed of a 5-cell perfect conductive cavity and the input coupler (see Fig. 5.1). The perfect electric conductive boundary conditions are used to define the boundary conditions for the coaxial lines of the input coupler and both beam tubes, because the real-valued eigenmode solver does not consider the energy transfer from the RF source to the particle beam. Afterwards the frequency-domain field simulation with the Perfect Boundary Approximation (PBA) hexahedral discretization mesh is carried out with the eigenmode solver from CST MWS and it exports the frequency and the corresponding electromagnetic field distribution of eigenmodes [9]. Later, the normalized shunt impedance (R/Q) of individual eigenmode can be computed based on (2.34) and (2.38) by using the Template Based Post Processing from CST MWS.

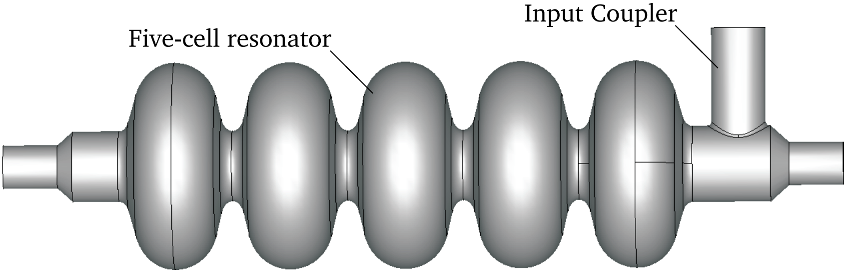

Figure 5.1: The Superconducting Proton Linac (SPL) cavity with beam tubes as well as the input coupler.

The accuracy of the real-valued eigenmode solver with hexahedral mesh cells is tested for the SPL cavity. For the frequency domain calculations several different discretization meshes have been used. According to the design frequency f_0 of the fundamental accelerating mode ($TM_{010,}\pi$) a logarithmic relative error can be calculated by,

$$\text{relative error} = \log_{10} \frac{|\mathrm{f}_{\text{numerical}} - \mathrm{f}_0|}{\mathrm{f}_0} \tag{5.1}$$

The convergence study based on the calculation of a relative error is shown in Fig. 5.2. With the increase of the hexahedral mesh cells, the difference between the eigenfrequency from the numerical calculation and the reference frequency becomes smaller and a relative error in order of 10^{-4} is obtained. The frequencies as well as the normalized shunt impedances of the modes in the fundamental passband are listed in Table 5.1.

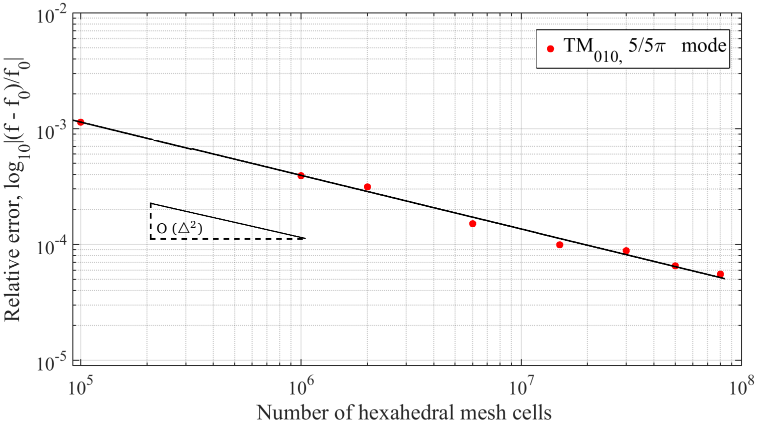

Figure 5.2: Relative error of the design frequency f_0 (704.4 MHz for the fundamental mode) to the numerical results f as a function of the number of hexahedral mesh cells for the SPL cavity with perfect electric conductive boundary conditions.

On the other hand, Fig. 5.2 indicates that, at least 20 million hexahedral grid points are required to acquire the relative error in order of 10^{-4}. The reason why a large number of hexahedral mesh cells is required is to represent the contours of the elliptical resonator of the SPL cavity precisely. Because the field simulation with hexahedral elements can be only run on a single workstation or computer, it is very time consuming to run field simulations with a large number of hexahedral elements. For example it took about 170 hours to run the computation task with 20 million hexahedral elements on a powerful single workstation (CPU: 8 processors (Intel Xeon X5472 ®3.00GHZ). DRAM: 64GB) for calculating the 5 monopole modes in fundamental passband for the SPL cavity. Therefore the field simulation with hexahedral elements is a demanding computation task. To solve this problem, a parallel real-valued eigenmode solver by using accurate curvilinear finite elements, which are able to capture the non-flat shape of typically applied superconducting resonator structures, is used [55].

	Hexahedral Elements (CST MWS)			Tetrahedral Elements (CEM3Dr)		
Mode	Meshcells / million	Frequency / MHz	R/Q / Ω	Meshcells / million	Frequency / MHz	R/Q / Ω
TM_{010}, 1/5 π	80	692.416	0.002	6.2	692.446	0.002
TM_{010}, 2/5 π	80	695.643	0.037	6.2	695.676	0.037
TM_{010}, 3/5 π	80	699.710	0.010	6.2	699.744	0.011
TM_{010}, 4/5 π	80	703.065	0.071	6.2	703.101	0.067
TM_{010}, 5/5 π	80	704.361	565.468	6.2	704.398	565.452

Table 5.1: Frequencies and R/Q of the monopole modes in the 1st monopole passband for different types of discretization. The calculations are performed on meshes with 80 million hexahedra and 6.2 million tetrahedrons.

5.1.2 Field Simulation in Frequency Domain by the Finite Element Method

As mentioned in the last subsection, the field simulation by using FIT on a single computer or workstation is a demanding computation task. Fortunately, at TEMF a parallel eigenmode solver based on real-valued higher-order finite element (FEM) analysis is available. The eigenmode solver has been used to compute the resonance frequency and the corresponding field distribution of eigenmodes in the SPL cavity. Firstly, for the FEM discretization, tetrahedral grids and higher-order curvilinear elements (Fig. 5.3) are applied to increase the accuracy of the geometrical approximation of the elliptical cavity.

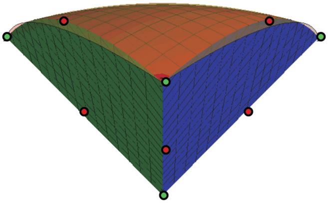

Figure 5.3: Curvilinear tetrahedral element. [55]

The geometric modeling of the accelerating structures with the tetrahedral meshing is performed within CST MICROWAVE STUDIO [9]. Perfect electric conductive boundary conditions are used to define the boundary conditions for the coaxial lines of the input coupler and both beam tubes. Afterwards, the mesh information is passed to the real-valued Computational Electromagnetics 3D solver (CEM3Dr) [55] to calculate the resonance frequencies and the corresponding field distributions of the eigenmodes, which are required for computing the shunt impedances of the eigenmodes.

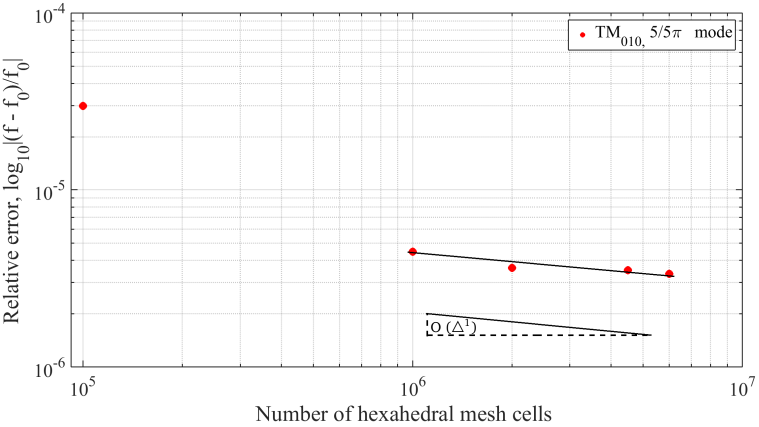

Figure 5.4: Relative error of the designed frequency f_0 (704.4 MHz for the fundamental mode) to the numerical results f as a function of the number of tetrahedral mesh cells for the SPL cavity with perfect electric conductive boundary conditions.

Similarly, the accuracy of the real-valued FEM eigenmode is tested for the SPL cavity. For the FEM field simulation different discretization meshes have been used and the relative error, given with (5.1) is shown in Fig. 5.4. As the number of tetrahedral mesh cells increases, the difference between the calculated eigenfrequency and the reference frequency becomes smaller and a relative error in order of 10^{-5} is reached. In addition, Fig. 5.4 shows a fast convergence. Since the FEM eigenmode solver can be run on a distributed memory architecture using MPI parallelization, a good computational performance can be achieved. For example it took about 100 minutes to run the computation task with 6 million tetrahedral elements on the powerful cluster TEMFCL2000 by using 20 nodes for calculating the 5 eigenmodes in the fundamental passband for the SPL cavity. Details of the cluster TEMFCL2000 are listed in Appendix A. The frequencies as well as the normalized shunt impedances (R/Q) of the modes in the fundamental passband are listed in Table 5.1.

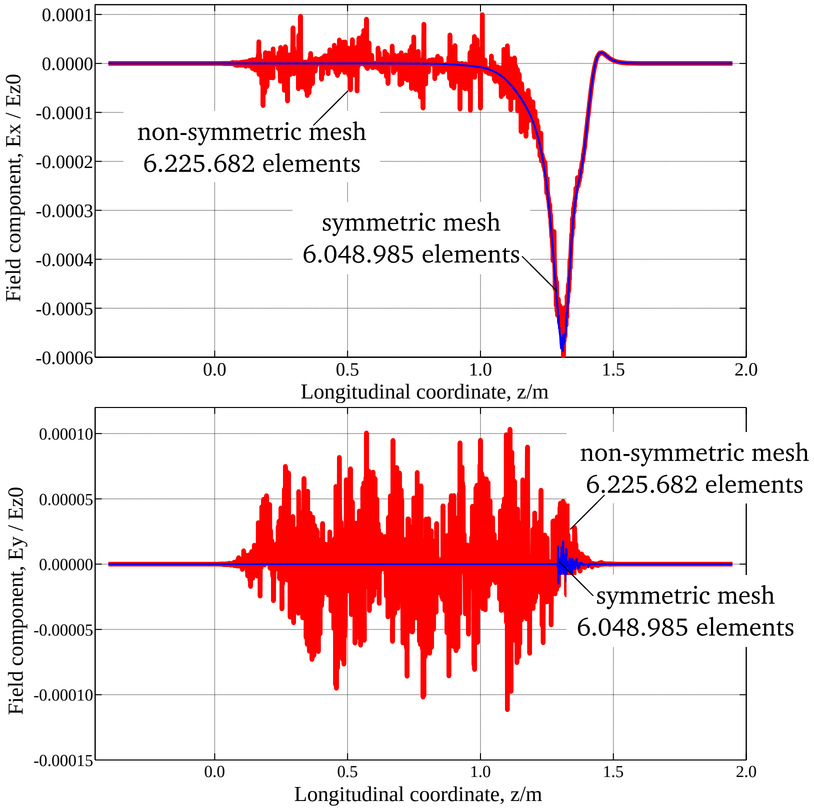

Figure 5.5: Horizontal and vertical component of the electric field strength relative to the absolute maximum of the longitudinal electric field strength Ez0 evaluated along the geometrical axis of the cavity. All calculations are performed by using non-symmetrical and symmetrical curvilinear tetrahedral meshes.

Apart from the eigenmode frequencies, the calculated electromagnetic field distribution demands also high precision in order to calculate the shunt impedance precisely. Due to the asymmetrical main input power coupler, a transverse electric field component is induced along the particle beam axis [55]. Its amplitude is up to four orders of magnitude smaller compared to the longitudinal components of the electric field strength (see Fig. 5.5). In addition, because of numerical errors introduced by the FEM algorithm, the artificial transverse field components along the particle beam axis can be observed in terms of oscillations [55].

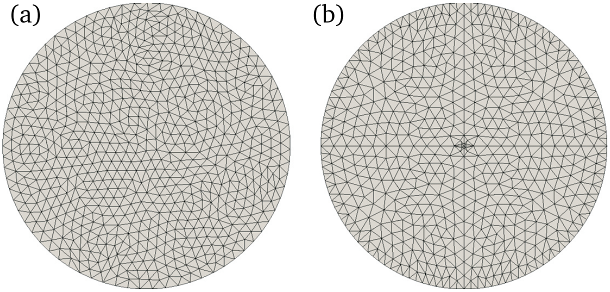

Figure 5.6: Cross section of a tetrahedral mesh in a plane normal to the longitudinal axis of the resonator for an unsymmetric mesh (a) and a symmetric mesh (b) [55].

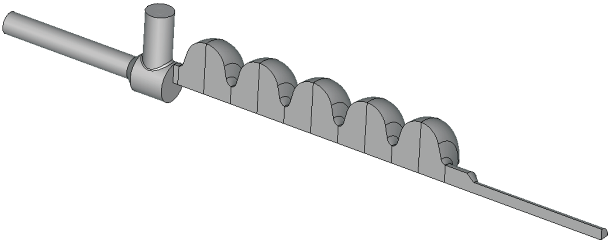

Figure 5.7: Geometrical model of the 5-cell SPL cavity used to set up a partially symmetric mesh.

The undesired oscillations cannot be completely suppressed but can be reduced substantially by using a symmetric mesh during the field simulation process. In Fig. 5.6 the unsymmetric and symmetric mesh are shown. For the SPL cavity with input coupler, at least in the cavity region a symmetric mesh should be generated. Fig. 5.7 shows a geometrical model of the SPL cavity, which is used to set up a partially symmetric mesh. At first an initial mesh is generated for 1/4 of the model (resonant region). In the next step, the generated tetrahedral elements are mirrored into the missing quadrants [55]. From Fig. 5.5 it can be noticed that the oscillation of the transverse components Ex and Ey in the resonant region has vanished if the field is evaluated with symmetric tetrahedral mesh cells. Further oscillations only appear in the beam pipe where the power coupler is assembled, because the mesh in this area is unsymmetric. Nevertheless, this oscillation has been reduced significantly. Moreover, quite smooth longitudinal components Ez, which are required to compute the shunt impedances of eigenmodes, are obtained (Fig. 5.8).

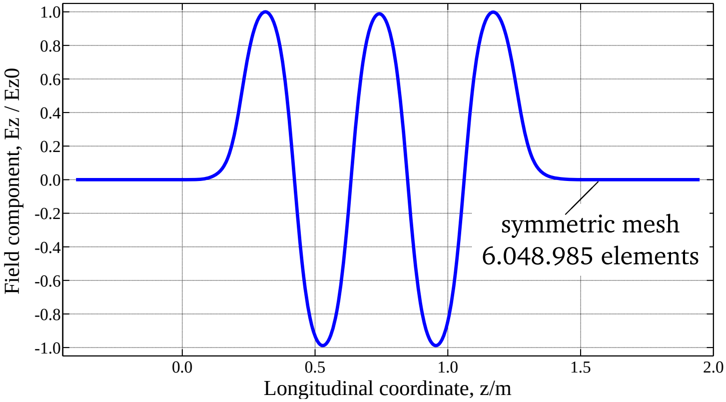

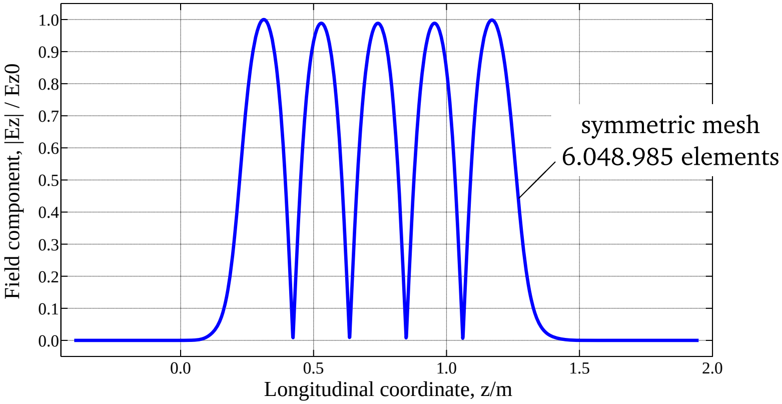

Figure 5.8: Longitudinal component of the electric field strength Ez relative to the absolute maximum of the longitudinal electric field strength Ez0 evaluated along the geometrical axis of the cavity. All calculations are performed by using symmetrical curvilinear tetrahedral elements.

5.1.3 Convergence of the hexahedral and the symmetric tetrahedral elements

In Fig. 5.9, the results for the monopole modes in the fundamental passband computed by using the PBA hexahedral and the symmetric curvilinear tetrahedral elements are compared. The frequencies in fundamental passband from 690 up to 705 MHz are given on the horizontal abscissa. The vertical coordinate represents the frequencies of the eigenmodes obtained from the real-valued eigenmode solver by using different hexahedral mesh cells and symmetric curvilinear tetrahedral mesh cells. Fig. 5.9 shows that, as the number of mesh cells increases, a convergence of the calculated frequencies to the design frequency is observed for the both mesh types. Additionally, the FEM eigenmode solver converges faster than the FIT eigenmode solver. Furthermore, due to the calculation time the parallel real-valued FEM eigenmode solver has proven to do the computation work for an elliptical lossless SPL cavity.

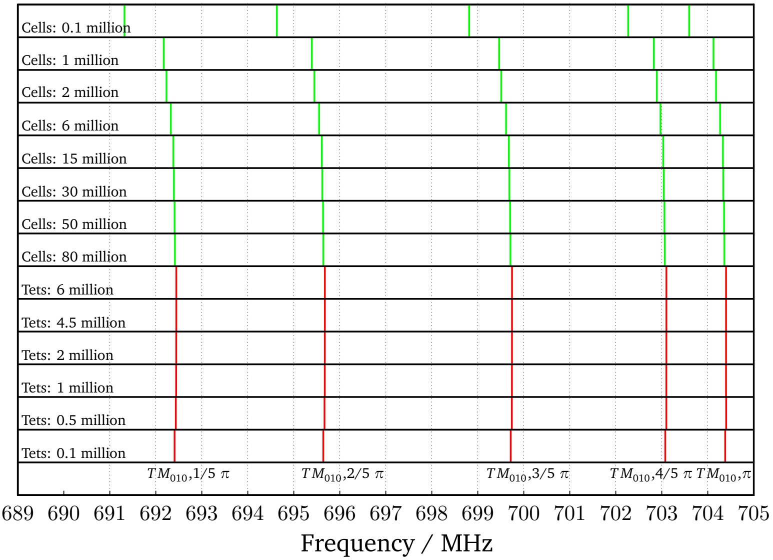

Figure 5.9: Convergence study showing a comparison between the eigenfrequencies calculated with the FIT eigenmode solver (green color) and the parallel real-valued FEM eigenmode solver (red color). For the FIT eigenmode solver eight different PBA hexahedral discretization meshes are used, meanwhile the FEM eigenmode solver exploits six different curvilinear symmetric tetrahedral discretization meshes.

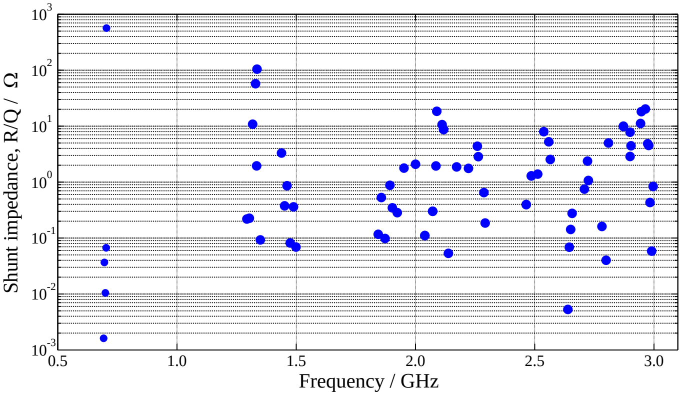

Figure 5.10: Normalized shunt impedances for the monopole modes in the SPL cavity up to 3 GHz. The blue points are obtained on a mesh with 6.2 million symmetric curvilinear tetrahedrons.

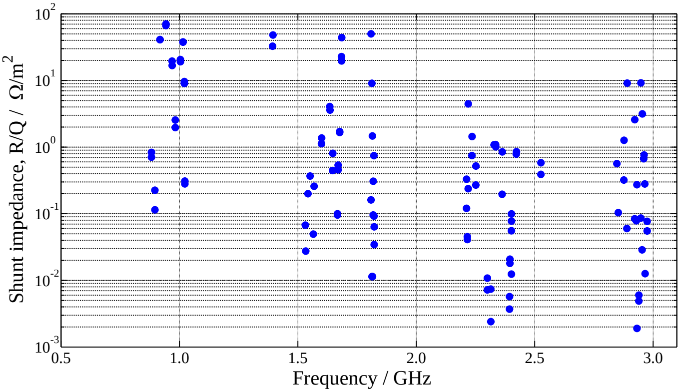

Figure 5.11: Normalized shunt impedances for the dipole modes in the SPL cavity up to 3 GHz. The blue points are obtained on a mesh with 6.2 million symmetric curvilinear tetrahedrons.

The real-valued eigenmode solver with symmetric curvilinear tetrahedral elements has a good performance for computing the eigenmodes in the lossless elliptical SPL cavity. Therefore this eigenmode solver are applied to the SPL cavity to determine the resonance frequency, the corresponding field distribution and the normalized shunt impedances (R/Q) for all monopole and dipole modes up to 3.0 GHz. In Fig. 5.10 and Fig. 5.11, the monopole modes in the fundamental passband and the higher-order modes with the their R/Q values in the SPL cavity are listed, respectively. Fig. 5.10 shows that the R/Q of the accelerating mode $TM_{010,}, \pi$ is about 500 Ω. The other $TM_{010,}, \pi$ modes have very low R/Q values. Some higher-order modes however still have large R/Q. These are cumbersome for the particle beam and must be effectively suppressed by higher-order mode couplers. All computed results have been transfered to CERN, such that the CERN research staffs can evaluate the dangerous modes and can further design the SPL cavity accordingly.

5.2 Computation of the Shunt Impedance in Acceleration Resonators under precise Consideration of Coupler Structures

A superconducting radio frequency (RF) cavity requires dedicated couplers to transfer energy from the RF source to the beam. Simultaneously, higher-order mode (HOM) couplers are installed to effectively suppress parasitic modes. As a consequence, the numerical eigenmode analysis based on real-valued variables is no longer suitable to describe the dissipative acceleration structure. At the Computational Electromagnetics Laboratory (TEMF) a parallel robust eigenmode solver to calculate the eigenmodes in the lossy acceleration structure is available. This eigenmode solver is based on complex-valued finite element analysis and utilizes basis functions up to the second order on curved tetrahedral elements to enable the high precision elliptical cavity simulations. In this section, firstly the algorithm of this eigenmode solver is briefly introduced. Afterward the application of this eigenmode solver is presented. Finally, the post-processing work is introduced.

5.2.1 Introduction of the Numerical Method

Because of the dissipative behavior of the couplers for the cavity, a complex-valued eigenmode solver is needed to describe the electromagnetic distribution properly [84]. Generally, Maxwell's equations are the mathematical foundation of the eigenmode analysis for resonating structures. To describe the electromagnetic field distribution inside elliptical RF accelerating cavities with high precision, the continuous Maxwell's equation can be discretized into a suitable matrix equation with the help of the finite element method [47]. The finite FEM discretization is based on a tetrahedral grid. Higher order curvilinear elements have been be applied to satisfy the demand for high precision modeling of the elliptical cavity [55]. The geometric modeling of the accelerating structures with the tetrahedral meshing is carried out within the CST MICROWAVE STUDIO [9]. In absence of any sources, the curl-curl equation (4.11) can be reduced to an eigenvalue formulation

$$\nabla \times \frac{1}{\mu} \nabla \times \underline{\mathbf{E}} \;=\; \omega^2 \epsilon \underline{\mathbf{E}} \tag{5.2}$$

which can be modified by using the material parameters according to (2.13) and (2.14). Then, we use higher oder Nédélec elements and Galerkin's approach to discretize the equation (5.2). The electric strength $\underline{\mathbf{E}} = \sum_j \alpha_j \boldsymbol{w}_j^{3D}$ can be expanded in terms of the reduced second order real-valued vector basis functions [85] with the complex-valued weighting coefficients (degrees of the freedom) α_i [86]. Following Galerkin's approach, the discrete eigenvalue formulation can be given by:

$$\boldsymbol{S}\boldsymbol{\alpha} \;=\; \omega^2 \boldsymbol{M}\boldsymbol{\alpha} \tag{5.3}$$

with the FEM stiffness matrix

$$S_{ij} \;=\; \int_V \frac{1}{\mu} (\nabla \times \boldsymbol{w}_i^{3D}) \cdot (\nabla \times \boldsymbol{w}_j^{3D}) dV \tag{5.4}$$

and the FEM mass matrix

$$M_{ij} \;=\; \int_V \epsilon \boldsymbol{w}_i^{3D} \cdot \boldsymbol{w}_j^{3D} dV \tag{5.5}$$

The eigenvector variable $\boldsymbol{\alpha}$ collects the unknown weighting coefficients α_j.

In addition, a partial integration of the curl-curl contribution results in a surface integral term according to (4.29)

$$\int_{\partial V} \frac{1}{\mu} (\mathbf{n} \times (\nabla \times \underline{\mathbf{E}})) \cdot \boldsymbol{w}_i^{3D} dA \tag{5.6}$$

with $\nabla \times \underline{\mathbf{E}} = -\jmath\omega\mu\underline{\mathbf{H}}$. Equation (5.6) contributes the boundary conditions of this numerical method [47]. Regarding cavity simulations in this section three kinds of boundary condition are used [47].

Firstly, the perfect electric conductive (PEC) boundary condition are used on the perfect conductive surface of the cavity, where the tangential electric field components are vanishing. Therefore the equation (5.6) does not contribute to the formulation of the PEC boundary condition.

Secondly, perfect magnetic conductive (PMC) boundary conditions are characterized by the vanishing tangential magnetic field components in the interface plane ($\mathbf{n} \times \mathbf{H} = 0$) which prevents the equation (5.6) to contribute to the formulation of the PMC boundary condition.

Finally, because the researched accelerator in this thesis are manufactured by superconducting materials, the dissipative behavior of the model does not arise from the material itself but is from the energy exchange along the HOM couplers, the power coupler as well as the beam tubes, if the resonance frequency is above the cutoff frequency of the corresponding waveguides. For this reason, the port boundary conditions are required. The port boundary condition models a true port interface accurately with the help of a two-dimensional (2D) modal expansion of the resulting electromagnetic field in the specified boundary plane of the waveguide. Once the frequency of the relevant eigenmodes in the waveguide is fixed, the corresponding modal field pattern in the port plane can be achieved from a 2D eigenvalue formulation [47]. With these modal field information, the resulting boundary can be evaluated by equation (5.6).

Afterwards, the resonance frequency of eigenmode and the field distribution in cavities can be obtained by iterative evaluation steps [47]. Due to the dissipative model, the obtained angular resonance frequency is complex.

$$\omega = \omega_{\text{real}} + \jmath\omega_{\text{imag}} \tag{5.7}$$

The real part ω_{real} represents the angular resonance frequency of eigenmode, while the imaginary part ω_{imag} describes the damping of the oscillation. The quality factor is specified by

$$Q = \frac{\omega_{\text{real}}}{2\omega_{\text{imag}}} \tag{5.8}$$

Due to the higher-order curvilinear FEM elements and the complex-valued variables, the solution of the complex-valued eigenmodes solver is much more time consuming. To achieve a good computational performance, a distributed memory architecture using MPI parallelization strategy has been utilized for the implementation [47].

Since the complex-valued eigenmode solver is suitable to describe the dissipative model, the eigenmode solver has been applied to the TESLA 1.3 GHz accelerating cavity (Fig. 5.12) to determine the characteristic values (resonance frequency and quality factor) for all modes in the 1st monopole passband [32]. The TESLA 1.3 GHz cavity is composed of a perfect conductive 9-cell cavity, the input coupler as well as the up- and downstream HOM couplers. Port boundary conditions are used to define the boundary conditions for the three couplers and both beam tubes. The penetration depth of the main input coupler is set to 8 mm.

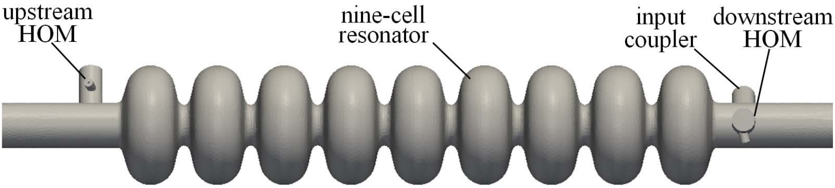

Figure 5.12: TESLA 9-cell 1.3 GHz superconducting RF cavity with beam tubes as well as the input coupler and two HOM couplers.

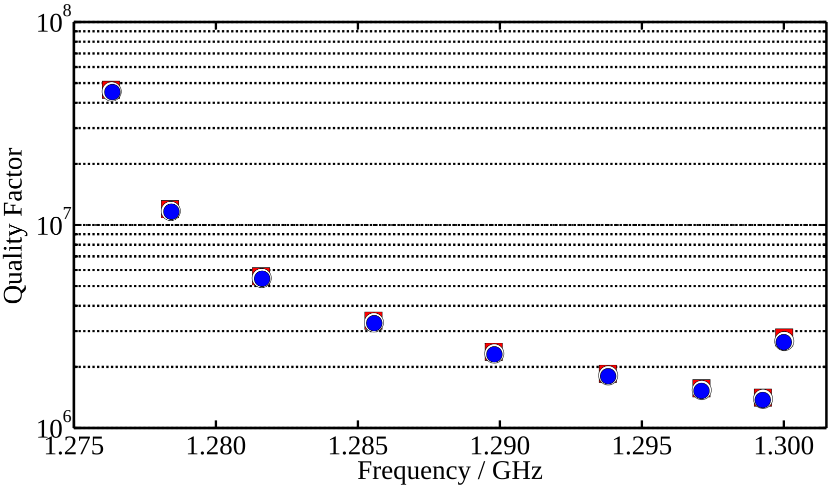

Figure 5.13: Quality factors versus frequencies for the monopole modes in the 1st monopole passband for different discretization. The calculations are performed on meshes with 315.885, 1.008.189 and 3.081.614 tetrahedrons indicated by red squared, white circled and blue data points.

The resonance frequency f as well as the quality factor Q of the eigenmodes can be determined simultaneously by the equations (5.7) and (5.8). In Fig. 5.13 the colored points indicate the accurate values of frequencies and quality factors (Q-value) for the monopole eigenmodes in the 1st monopole passband. The quality factor of accelerating mode $TM_{010,}\pi$ is about $2.7 \cdot 10^6$, while the largest quality factor of the other TM_{010} modes is about $4.5 \cdot 10^7$. Since the complex-valued eigenmode solver can perform the calculation of electromagnetic fields in the lossy model as required, the resonance frequency, the quality factor (Fig. 5.14) and the corresponding field distribution for 192 modes up to the 5th dipole passband (3.12 GHz) in TESLA 1.3 GHz cavity have been determined [32].

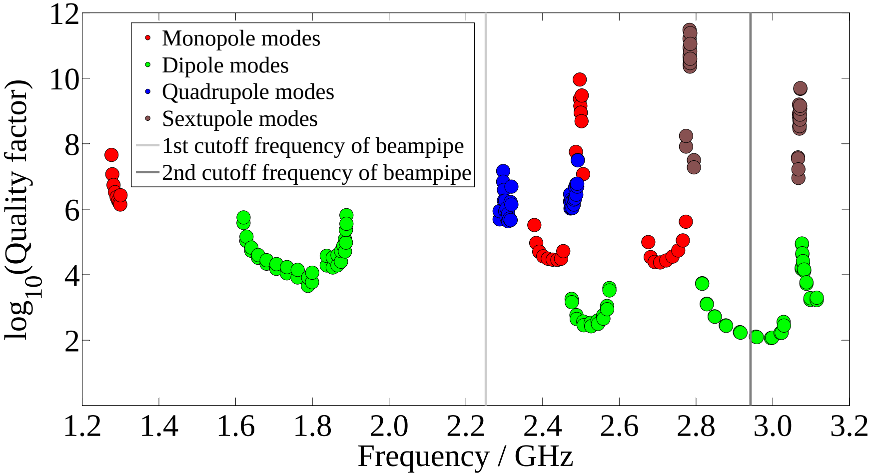

Figure 5.14: Quality factors versus frequencies for all eigenmodes in the TESLA 1.3 GHz cavity up to the 5th dipole passband (3.12 GHz). All calculations are performed on meshes with 3.081.614 tetrahedrons

According to Fig. 5.14 there are one monopole passband (9 monopole modes including the accelerating mode $TM_{010,}\pi$) and two dipole passbands (36 dipole modes) below the cutoff frequency of the beampipe. These modes cannot pass through the beampipe. Coupling of these modes to external devices can only occur with the help of the HOM couplers and the input power coupler. The largest quality factor of the dipole modes in the 1st and 2nd dipole passbands is about $8 \cdot 10^5$. Above the cutoff frequency of the beampipe and up to 3.12 GHz, there are three monopole passbands (27 monopole modes), three dipole passbands (50 dipole modes), two quadrupole passbands (36 quadrupole modes) and two sextupole passbands (36 sextupole modes). The modes from the 4th monopole passband have larger external Q-values (up to $1.33 \cdot 10^{10}$) than the modes from the other 4 monopole passbands, while the modes in the 3rd, 4th, and 5th dipole passbands have smaller Q-values than the modes in the 1st and 2nd dipole passband. It is a remarkable fact that the modes from the 1st sextupole passband have the largest Q-values. The largest value can reach to about 10^{11}. With the information of the resonance frequencies together with the corresponding field distribution, the shunt impedances for all 192 eigenmodes up to the 5th dipole passband (3.12 GHz) have been determined.

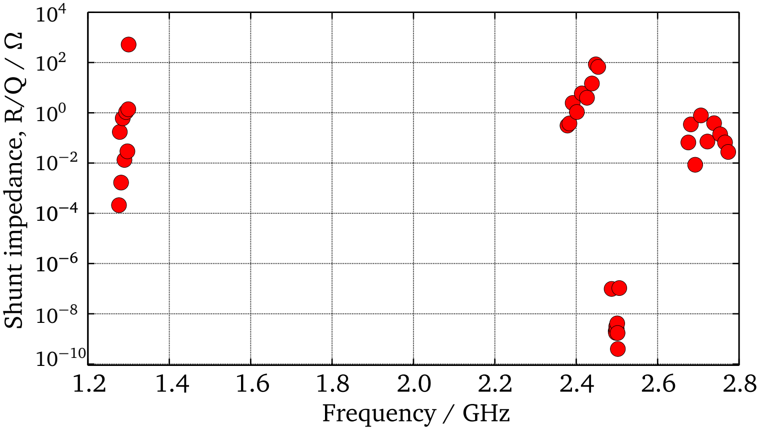

Figure 5.15: Normalized shunt impedances R/Q for the monopole modes in the TESLA 1.3 GHz cavity up to the 4th monopole passband (2.8 GHz). All calculations are performed on meshes with 3.081.614 tetrahedrons

The graphical representations of the parameter R/Q for all calculated monopole, dipole, quadrupole and sextupole modes are given in Fig. 5.15, Fig. 5.16, Fig. 5.17 and Fig. 5.18, respectively. Fig. 5.15 shows that besides the accelerating mode $TM_{010,}\pi$ the modes of the 2nd monopole passband, which are above the first cutoff frequency of the beam pipe, have large R/Q. The largest R/Q of the modes in the 2nd monopole passband can reach to about 100 Ω, while the R/Q of the accelerating mode $TM_{010,}\pi$ is about 100 Ω. The modes of the 3rd and 4th passbands have small R/Q values. Especially, the modes in the 3rd monopole passband are monopole TE-modes. Because of the vanishing longitudinal electric field components ($E_z = 0$) the R/Q of these are approximately zero. All modes of the 2nd to 4th passbands are above the first cutoff and below the second cutoff frequency.

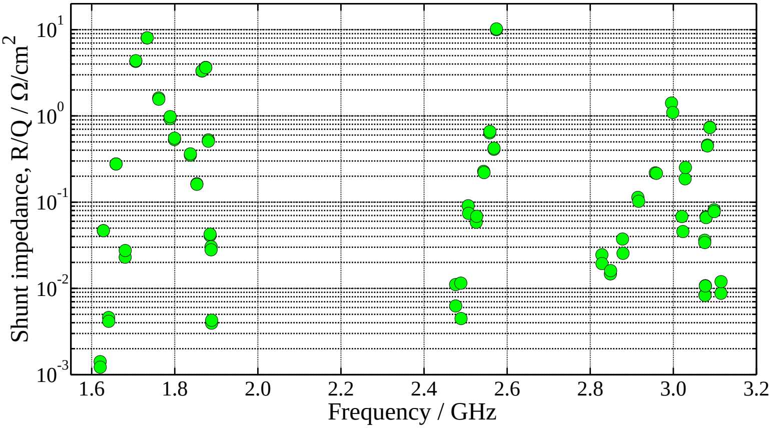

Figure 5.16: Normalized shunt impedances R/Q for the dipole modes in the TESLA 1.3 GHz cavity up to the 5th dipole passband (3.2 GHz). All calculations are performed on meshes with 3.081.614 tetrahedrons

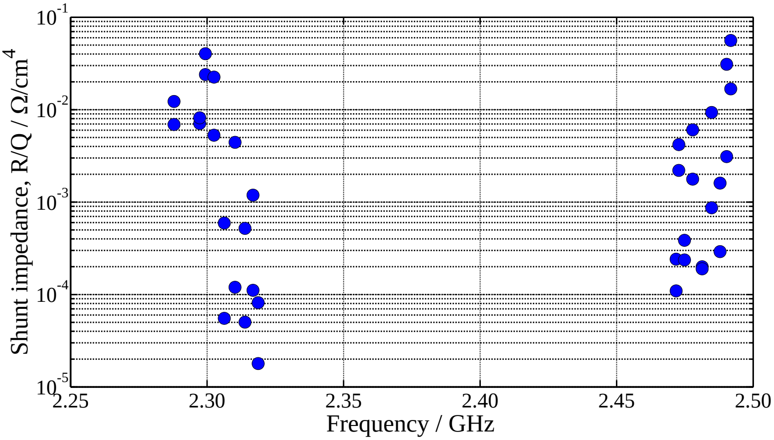

Figure 5.17: Normalized shunt impedances R/Q for the quadrupole modes in the TESLA 1.3 GHz cavity up to the 2nd quadrupole passband (2.5 GHz). All calculations are performed on meshes with 3.081.614 tetrahedrons

The modes of the first two dipole passbands are below the cutoff frequency of the beampipe. Most of these dipole modes have small transverse R/Q values. The mode with largest transverse R/Q in these two dipole passbands belongs to the 1st dipole passband (see Fig. 5.16). Meanwhile, the dipole modes with frequencies above the beam pipe cutoff frequencies have small R/Q values too. The mode with the largest transverse R/Q is found in the third dipole passband. The results of the R/Q calculations for quadrupole and sextupole modes are presented in Fig. 5.17 and Fig. 5.18, respectively. The first two quadrupole passbands lie between the first and second cutoff frequency of the beampipe, while the 1st sextupole passband is above the first cutoff frequency and 2nd sextupole passband above the second cutoff frequency. The normalized shunt impedances are small for all quadrupole and sextupole modes.

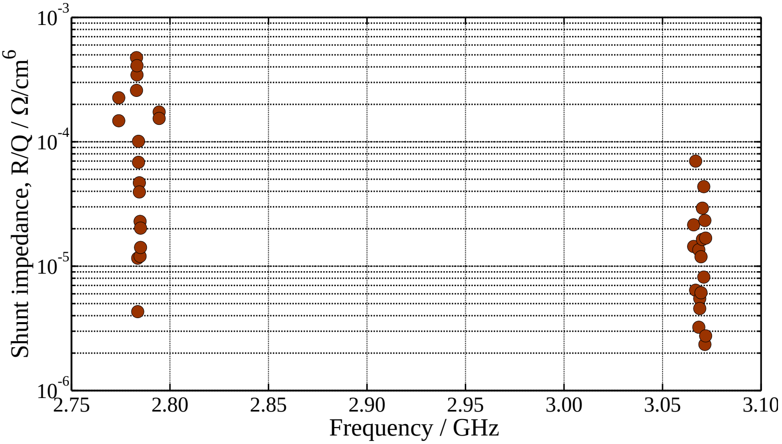

Figure 5.18: Normalized shunt impedances R/Q for the sextupole modes in the TESLA 1.3 GHz cavity up to the 2nd sextupole passband (3.1 GHz). All calculations are performed on meshes with 3.081.614 tetrahedrons

In summary, all these characteristic values together with corresponding field plots of all 192 eigenmodes up to the 5th dipole passband (3.12 GHz) has been transfered to DESY and will be published in a TESLA report at DESY, such that the dangerous modes can be mitigated in the design of the TESLA accelerating cavity properly.

5.2.3 Post-processing of the Simulation Results

After calculation of the eigenmodes there are some post-processing tasks to be done. Some post-processing routines have been developed to ease the necessary post-processing steps, while others have been developed to investigate the characteristics of the accelerators. In this subsection a dedicated algorithm for automatically identifying the eigenmode type in a batch mode operation is firstly introduced. Afterwards, we show an approach to smooth the electromagnetic field by using Kirchhoff's integral theorem, so that the shunt impedance of the eigenmode can be computed precisely. The 3rd post-processing task provides an alternative way to compute the Q-values of the eigenmodes with the visualization and post-processing software ParaView [87]. For the 4th task, a sensitivity analysis for the geometrical changes of the TESLA cavities is developed. The last post-processing job is to compare the calculated results from various eigenmode solvers.

5.2.3.1 Automatic Identification of Eigenmode Type

After determination of the resonance frequency and the corresponding field distribution of each eigenmode, it is very hard and inconvenient to manually identify each eigenmode type. For this reason a dedicated algorithm has been developed to automatically identify the eigenmode type in a batch mode operation. The first step of the algorithm is to sample the longitudinal components Ez of an eigenmode along a circle in the individual cell (Fig. 5.19). The radius of the circle has to be selected properly to avoid incorrect identification of the eigenmode type because the magnitude of Ez in the vicinity of the particle beam axis for some higher-order modes may be too weak. Afterwards the mode type can be automatically identified according to the number of zero crossings (red points in Fig. 5.20) for the sampled Ez along the circle. For example four zero crossings refers to a quadrupole mode in Fig. 5.20.

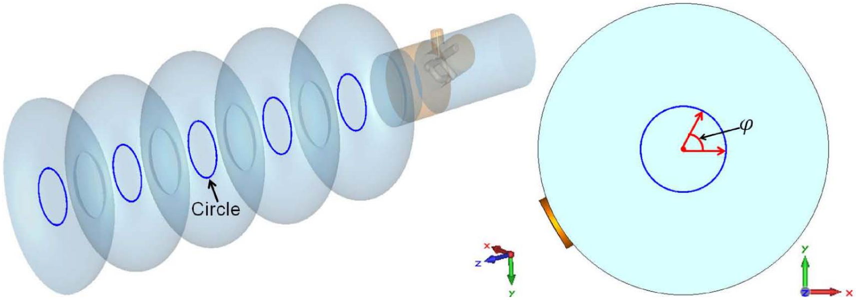

Figure 5.19: Sample path of the electric field strength **E** along a circle.

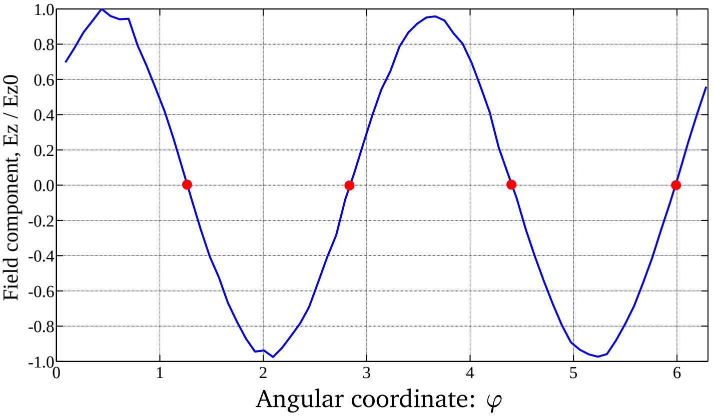

Figure 5.20: Longitudinal component of the electric field strength Ez relative to the absolute maximum of the longitudinal electric field strength Ez0 along the specified circular sample path.

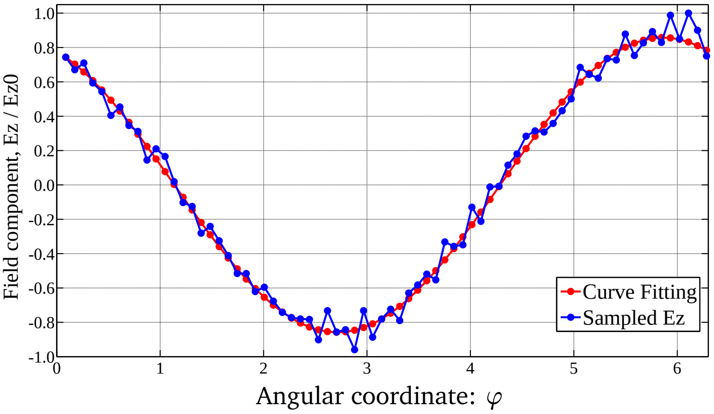

Figure 5.21: Longitudinal component of the electric field strength Ez relative to the absolute maximum of the longitudinal electric field strength Ez0 along the specified circular sample path and its curve fitting.

Fig. 5.21 states the unsmooth curve for the sampled component Ez of a dipole eigenmode. Under such situation the number of the zero crossings may be wrongly counted because of the zigzagged oscillations, so that the eigenmode type cannot be identified properly. For this reason an efficient algorithm has been developed. The principle of the algorithm is the custom parametric fitting [88]. As shown in Fig. 5.21, a trigonometric function can be utilized to fit the curves to the data of the sampled field component Ez. The function is given by

$$y = a\,sin(2\pi bx + c) \tag{5.9}$$

where the coefficients a, b and c are estimated by using Nonlinear Least Squares (Curve Fitting) procedure in MATLAB [78]. After rounding the value of the coefficients b to the nearest integers, the type of the eigenmode can be identified. In Fig. 5.21, the coefficient b from the fitting results is 0.997. The corresponding rounding value is 1, which obviously refers to a dipole mode. The advantage of this algorithm lies in the fact that the eigenmode type can be identified properly in spite of the zigzag formed field components Ez.

5.2.3.2 Field reconstruction

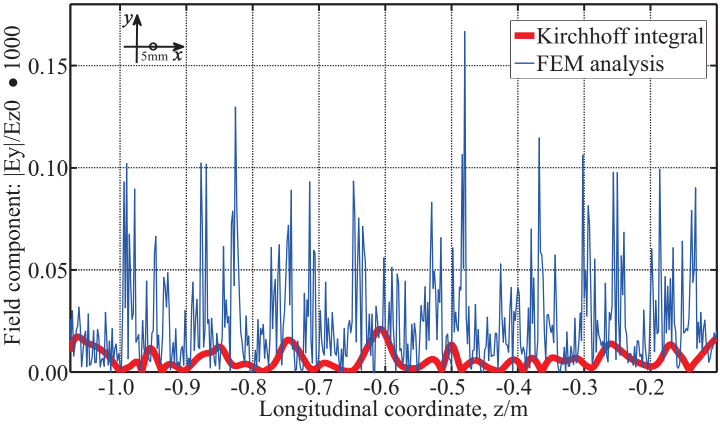

Figure 5.22: Evaluation of the transverse electric field components Ey off axis (x = 5mm). The field components Ey are normalized to the maximum longitudinal field value Ez0. All calculations are performed on symmetrical meshes with 2.997.778 curvilinear tetrahedrons.

As mentioned in section 2.3, the knowledge of the field components in the vicinity of the particle beam axis is required to determine the shunt impedance of the eigenmodes. But as shown in Fig. 5.22 for the $TM_{010,}\pi$ mode, the specified unsmooth transverse electric field components Ey off axis (x = 5 mm) for example, which have been directly calculated by complex-valued FEM analysis, are certainly up to four orders of magnitude smaller than the maximum longitudinal field value Ez0, but should be continuous and smooth due to the homogeneous vacuum condition inside the cavity.

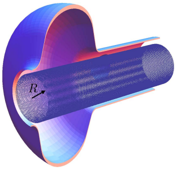

Figure 5.23: Closed surface inside the cavity used for field reconstruction.

In order to calculate the shunt impedance of the eigenmode with higher precision, the field components can be supplementarily smoothed on a physically motivated basis by using Kirchhoff's integral theorem [89]. Kirchhoff's integral theorem states that the electric field strength $\mathbf{E}_P$ at an arbitrary position p inside a closed surface can be determined once the field components $\mathbf{E}$ and $\mathbf{B}$ on a surface $\mathbf{A}$ are available (Fig. 5.23) [89]:

$$\mathbf{E}_P = \frac{1}{4\pi}\int_A \left(\mathbf{E}\frac{\partial G}{\partial \mathbf{n}} - G\frac{\partial \mathbf{E}}{\partial \mathbf{n}}\right)\cdot d\mathbf{A} \quad \text{with} \quad G = \frac{e^{jkR}}{R}, \quad k = \frac{2\pi f}{c_0} \tag{5.10}$$

where R is the distance from the position p to the surface element $d\mathbf{A}$ and vector $\mathbf{n}$ is the unit vector normal to the surface element $d\mathbf{A}$. Note that the electric field strength $\mathbf{E}$ satisfies

$$\nabla \times \mathbf{E} = -\jmath\omega\mathbf{B} \tag{5.11}$$

With equation (5.11), (5.10) can be written in the form

$$\mathbf{E}_P = \frac{1}{4\pi}\int_A \left((\mathbf{n}\times \jmath\omega\mathbf{B})G - (\mathbf{n}\times\mathbf{E})\times\nabla G - (\mathbf{n}\cdot\mathbf{E})\nabla G)\right)\cdot d\mathbf{A} \tag{5.12}$$

After determination of the resonance frequency and the corresponding field distribution of the eigenmode with the complex-valued eigenmode solver, we can use the equation (5.12) to reconstruct the electric field in the vicinity of the particle beam axis. Fig. 5.22 indicates a noticeable improvement. Although due to the numerical errors the roughness of the transverse electric field components Ey cannot be completely suppressed, the field components Ey by using Kirchhoff's integral are much more smooth than the field components from standard FEM analysis, so that the shunt impedance of the eigenmode can be calculated more precisely.

5.2.3.3 Computation of Quality Factor with ParaView

As already stated in section 2.3.3, the definition of the quality factor Q is given by

$$Q = \frac{\omega U}{P} \tag{5.13}$$

where ω is the angular frequency and U is the energy stored in the eigenmode. For the calculation with the real-valued and the complex-valued eigenmode solver, the eigenmodes are scaled such that U becomes 1. P represents the power loss of the eigenmode. Due to the infinite conductivity of the cavity wall, the power loss occurs only on the boundary of the waveguides (input coupler, HOM couplers and the beam pipes). The power loss on a cylindrical waveguide boundary is given by a surface integral:

$$P = \int_{A_{port}} \mathbf{S} \cdot d\mathbf{A} \tag{5.14}$$

where $\mathbf{S}$ is the Poynting vector defined by [90]

$$\mathbf{S} = \frac{1}{2} \underline{\mathbf{E}} \times \underline{\mathbf{H}}^* \tag{5.15}$$

where $\underline{\mathbf{E}}$ represents the electric field strength on the boundary of the waveguide and $\underline{\mathbf{H}}$ is the magnetic field strength on the boundary of the waveguide.

Since the complex-valued eigenmode solver provides the frequency and the corresponding field distribution of the eigenmode, the power loss of the eigenmode for each waveguide of the cavity can be calculated with (5.14) and (5.15). Eventually from the (5.13), the Q-value of the eigenmode in the dissipative cavity can be given by

$$Q = \frac{\omega U}{\sum_{i=1}^{n} P_i} \tag{5.16}$$

where P_i is the power loss for the single waveguide of the cavity. With summing up the power loss P_i we can get the total power loss of the eigenmode. We can compute the power loss with (5.14) and (5.15) by using ParaView [87]. ParaView is a powerful data analysis and visualization application software, which can quickly build electromagnetic field visualizations and analyze their data using qualitative and quantitative techniques [87]. Firstly all field data are imported in ParaView. Afterward, the field information on the boundary of each coupler and beampipe is collected by ParaView filters. By using the ParaView calculator, the Poynting vector on the boundary of the waveguide is computed. Finally, the corresponding power loss is automatically given by the Paraview filter.

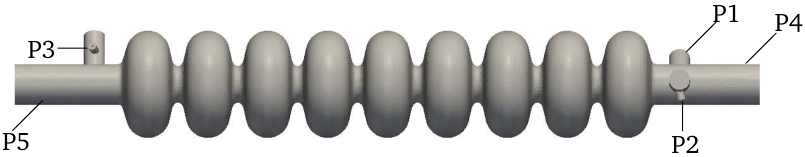

Figure 5.24: TESLA 9-cell 1.3 GHz superconducting RF cavity with beam tubes as well as the input coupler and two HOM couplers. P1: Input coupler, P2: Downstream HOM coupler, P3: Upstream HOM coupler, P4: Downstream beampipe, P5: Upstream beampipe.

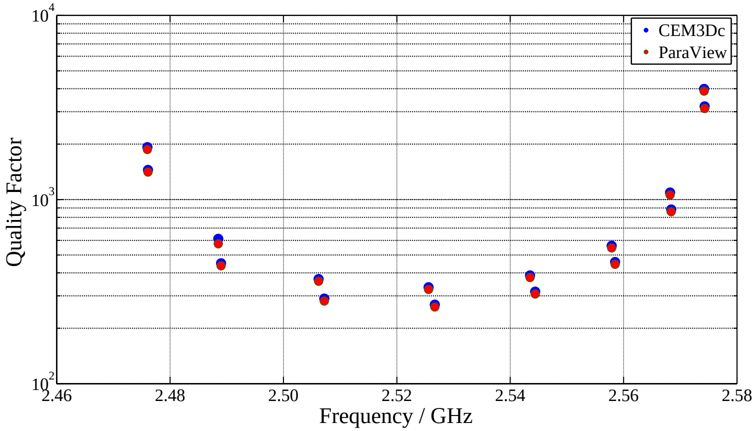

Figure 5.25: Quality factors versus frequencies for the dipole modes in the 3rd dipole passband. The calculations are performed by the complexed-valued eigenmode solver (CEM3Dc) and ParaView indicated by red and blue data points.

The approach is validated by computing the Q-values for all modes of the 3rd dipole passband in TESLA 1.3 GHz cavity (Fig. 5.24). The Q-values of these dipole modes calculated by complex-valued eigenmode solver and ParaView are plotted in Fig. 5.25. Fig. 5.25 shows that both approaches give similar Q-values. But the advantage of ParaView approach lies in its ability to present the power loss of eigenmodes for each single waveguide of the cavity. A complete list of all modes in 3rd dipole passband, their power loss for each waveguide and the Q-values calculated by the complex-valued eigenmode solver and ParaView are compiled in Table 5.2. Table 5.2 states that the power loss from both beam pipes ports is much larger than that from the couplers, because the modes in 3rd dipole passband are lying above the cutoff frequency of beampipe, so that they can couple well to the input and HOM couplers. In addition the power loss for the HOM couplers shows that the HOM couplers of the TESLA 1.3GHz cavity can effectively suppress the eigenmodes of 3rd dipole passband.

	f / GHz	P1 / W	P2 / W	P3 / W	P4 / W	P5 / W	Q / Paraview	Q / CEM3Dc
Mode 1	2.4760	1.04×10^4	2.98×10^5	2.33×10^4	3.09×10^6	4.66×10^6	1.93×10^3	1.87×10^3
Mode 2	2.4761	5.05×10^5	2.06×10^5	8.92×10^5	3.91×10^6	5.23×10^6	1.45×10^3	1.41×10^3
Mode 3	2.4885	2.71×10^4	3.14×10^4	7.02×10^4	1.03×10^7	1.51×10^7	6.12×10^2	5.75×10^2
Mode 4	2.4890	1.63×10^6	6.45×10^5	2.68×10^6	1.30×10^7	1.68×10^7	4.51×10^2	4.37×10^2
Mode 5	2.5062	4.51×10^4	1.45×10^6	1.20×10^5	1.75×10^7	2.35×10^7	3.70×10^2	3.60×10^2
Mode 6	2.5072	2.62×10^6	1.03×10^6	3.78×10^6	2.15×10^7	2.54×10^7	2.90×10^2	2.81×10^2
Mode 7	2.5256	6.30×10^4	1.58×10^6	1.52×10^5	2.11×10^7	2.46×10^7	3.34×10^2	3.25×10^2
Mode 8	2.5267	3.03×10^6	1.22×10^6	3.59×10^6	2.56×10^7	2.57×10^7	2.69×10^2	2.61×10^2
Mode 9	2.5435	7.86×10^4	1.37×10^6	1.52×10^5	2.04×10^7	1.93×10^7	3.87×10^2	3.77×10^2
Mode 10	2.5444	2.84×10^6	1.20×10^6	2.59×10^6	2.44×10^7	1.96×10^7	3.16×10^2	3.07×10^2
Mode 11	2.5579	8.14×10^4	9.54×10^5	1.19×10^5	1.57×10^7	1.18×10^7	5.61×10^2	5.46×10^2
Mode 12	2.5585	2.15×10^6	9.78×10^5	1.48×10^6	1.88×10^7	1.17×10^7	4.58×10^2	4.45×10^2
Mode 13	2.5682	6.03×10^4	4.83×10^5	6.81×10^4	8.75×10^6	5.42×10^6	1.09×10^3	1.06×10^3
Mode 14	2.5684	1.18×10^6	5.82×10^5	6.52×10^5	1.05×10^7	5.34×10^6	8.83×10^2	8.59×10^2
Mode 15	2.5742	2.51×10^4	1.23×10^5	2.22×10^4	2.51×10^6	1.38×10^6	3.99×10^3	3.88×10^3
Mode 16	2.5743	3.31×10^5	1.78×10^5	1.61×10^5	3.00×10^6	1.37×10^6	3.21×10^3	3.12×10^3

Table 5.2: Frequencies, power loss P_i for each waveguide and Q-values of the dipole modes in the 3rd dipole passband for TESLA 1.3 GHz cavity. The Q-values are calculated by using the complex-valued eigenmode solver and the application software ParaView.

5.2.3.4 Sensitivity Analysis

In practice, undesired changes to the geometry of the cavity can occur, as an example, the small defects can appear during the manufacturing process of the cavity, which can lead to the change of the eigenmode characteristics. For this reason it is essential to analyze the sensitivity of the eigenmodes according to geometrical changes of the cavity. The eigenmodes below the first cutoff frequency of the beampipe with large Q-value and shunt impedance *R* are studied, because these modes with large Q-values and *R* can cause the instabilities of the particle beam. To satisfy these requirements the monopole mode 2 and mode 9 in the 1st monopole passband, dipole mode 17 and mode 18 in 2nd dipole passband are picked out for the sensitivity analysis. To realize the geometrical modification of the cavity, the geometrical parameter of the single cavity cell can be changed in CST MICROWAVE STUDIO (Fig. 5.26). Afterwards, the frequencies, Q-values and the corresponding shunt impedances *R* of these eigenmodes are calculated by the complex-valued eigenmode solver. A graphical representation of these results together with the those calculated with original geometry of cavity are given in Fig. 5.27 and Fig. 5.28.

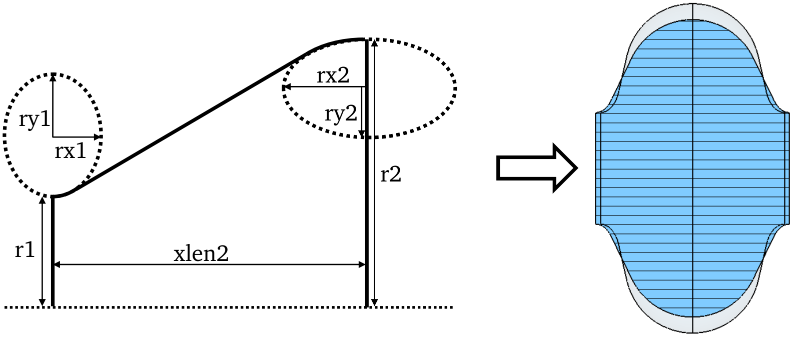

Figure 5.26: Parameter definition and geometry modification of the single TESLA 1.3 GHz cavity cell [9]

Fig. 5.27 states that the change of the geometrical parameter r2 and xlen2 can result in significant modifications of characteristics of mode 9 in the 1st monopole passband. For instance, in the middle cell or one of the end cells of the cavity r2 is set to be 1 mm larger than the designed r2, while xlen2 is set to be 1 mm smaller than the designed value, the corresponding calculated Q-value and *R* are much larger than those with the original geometry. Moreover the frequency of mode 9 is significantly changed. Because mode 9 is the accelerating mode, these large modifications can lead to improper particle beam acceleration. However, for the same geometrical change, the modification of Q-value and *R* for the monopole mode 2 is not significant. Only if the geometrical change are applied simultaneously to the four cells of the cavity, the modification of *R* is significant.

Fig. 5.28 depicts the obvious characteristics modification for the dipole modes 17 and 18 in 2nd dipole passband as well. With the geometry modifications of

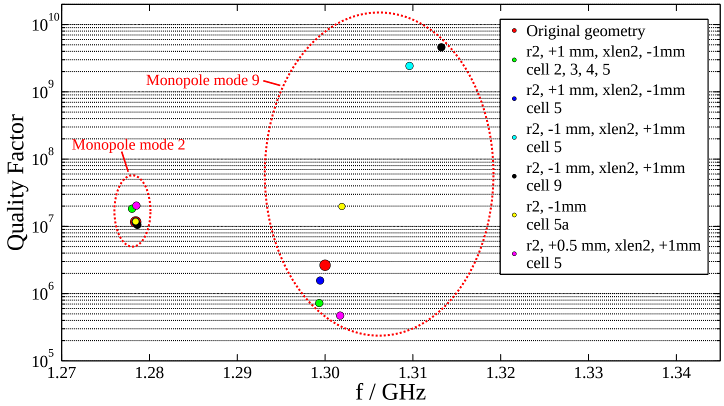

(a) Quality factors versus frequencies for the mode 2 and mode 9 in the 1st monopole passband for different geometry modifications of the TESLA 1.3 GHz cavity.

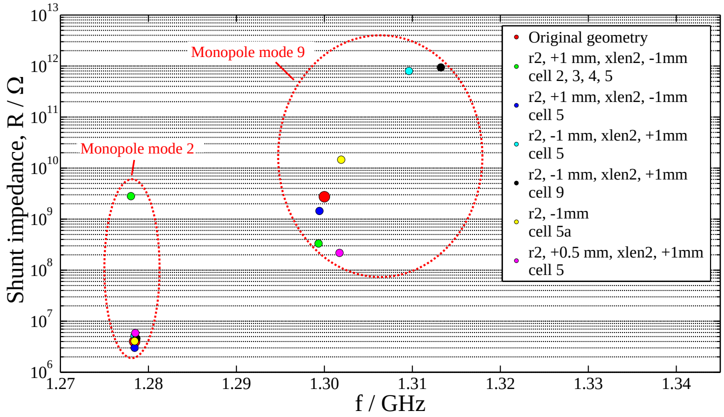

(b) Shunt impedances R versus frequencies for the mode 2 and mode 9 in the 1st monopole passband for different geometry modifications of the TESLA 1.3 GHz cavity.

Figure 5.27: Quality factors and shunt impedances R of the mode 2 and mode 9 in the 1st monopole passband which have been calculated for the sensitivity analysis plotted versus the frequencies of the modes.

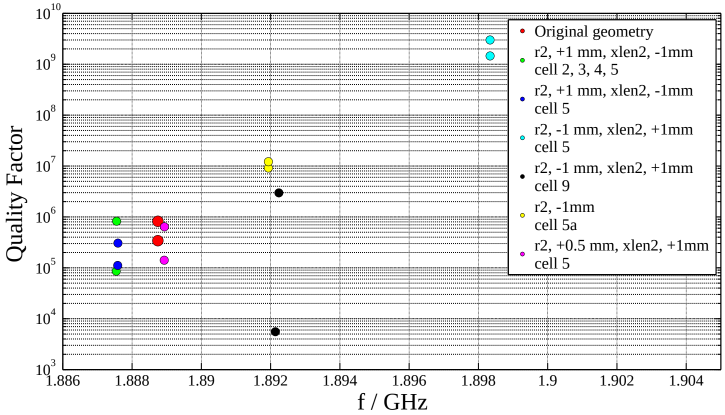

(a) Quality factors versus frequencies for the mode 17 and mode 18 in the 2nd dipole passband for different geometry modifications of the TESLA 1.3 GHz cavity.

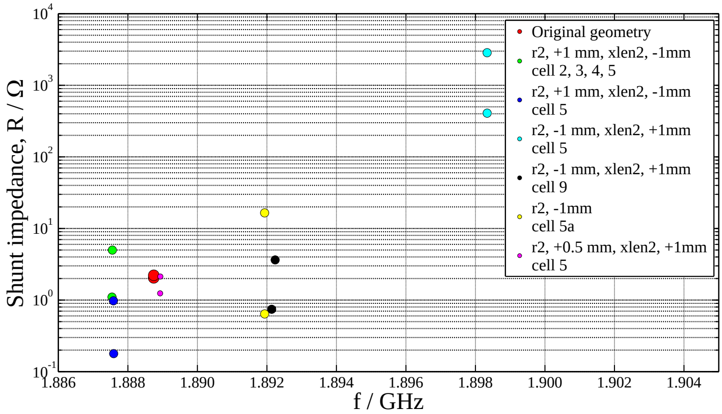

(b) Shunt impedances R versus frequencies for the mode 17 and mode 18 in the 2nd dipole passband for different geometry modifications of the TESLA 1.3 GHz cavity.

Figure 5.28: Quality factors and shunt impedances R of the mode 17 and mode 18 of the 2nd dipole passband which have been calculated for the sensitivity analysis plotted versus the frequencies of the modes.

the single cavity cell, not only the frequencies but also the Q-values and R of both modes are modified significantly. Especially, the cyan circled data points indicate that the Q-values of mode 17 and 18 can reach to about 10^9, if the shape of the middle cell of the cavity has been modified. The large Q-values for both dipole modes state that they do not couple well to the HOM couplers anymore. They can lead to particle beam instabilities. In summary, Fig. 5.27 and Fig. 5.28 imply that the eigenmodes with higher Q-values and R are not stable, if an undesired deviation of the cavity shape occurs. Such small undesired geometrical modifications have to be avoided to preserve the stability of the particle beam.

5.2.3.5 Comparison of the Results

In recent decades, research staffs from all over the world have been engaged in computations of the eigenmodes in the acceleration resonators by using various eigenmode solvers. The computed results have been published in scientific journals or reports. In this subsection the comparison of the results from various eigenmode solvers are introduced.

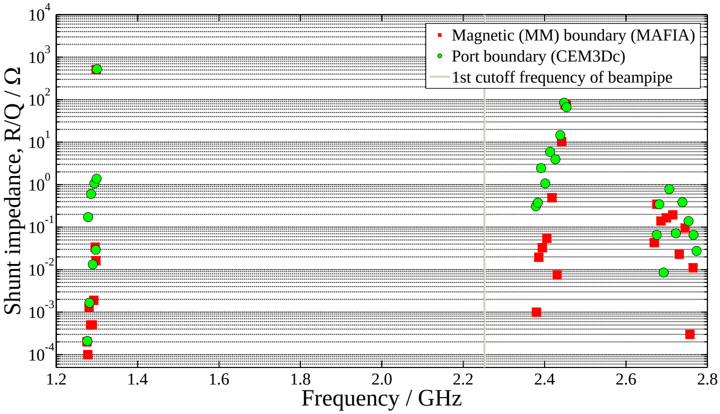

Figure 5.29: The normalized shunt impedances R/Q of the monopole modes which have been calculated for the 9-cell TESLA 1.3 GHz cavity plotted versus the frequencies of the modes. The red squares denote the modes obtained with magnetic (MM) boundary conditions from the MAFIA calculations [32]. The results obtained with port boundary conditions from CEM3Dc calculations are marked by green circles.

First of all, a graphic representation of the figure of merit R/Q for calculated monopole and dipole modes in the TESLA 1.3 GHz cavity using the electromagnetic field solver MAFIA based on real-valued finite integration technique (FIT) as well as CEM3Dc analysis, is given in Fig. 5.29 and Fig. 5.30 [32]. For the MAFIA calculations the EE and MM boundary conditions are applied to the three couplers and both beam tubes, while the port boundary conditions are used for three couplers and both beam tubes. Due to the lossless structures for the MAFIA calculations the corresponding Q-values of eigenmodes are extremely large, which can lead to extremely large shunt impedances R. Therefore the R/Q of the calculated modes from both eigenmode solver are compared. For the MAFIA calculations the 9-cell symmetric cavity (with symmetric end cells) without any couplers are applied [32], while a 9-cell cavity (with unsymmetrical end cells) with HOM couplers and input coupler is used for the CEM3Dc calculations. According to Fig. 5.29, a comparison between the MAFIA calculations and CEM3Dc calculations indicates larger R/Q from CEM3Dc calculations for most monopole modes in the 2nd and 4th monopole passbands (2.3 to 2.8 GHz). This has to be primarily attributed to different boundary conditions, mesh types and applied geometry models.

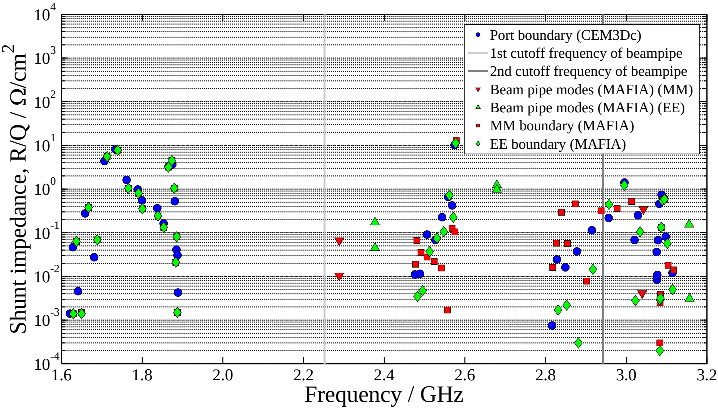

Figure 5.30: The parameter R/Q of the dipole modes calculated for the 9-cell TESLA 1.3 GHz cavity plotted versus the frequencies of the modes. The red squares and downward-pointing triangles denote the modes obtained with magnetic (MM) boundary conditions from the MAFIA calculations while the green diamonds and upward-pointing triangles correspond to the modes obtained with electric (EE) boundary conditions from the MAFIA calculations [32]. The results obtained with port boundary conditions from CEM3Dc calculations are marked by blue circles.

The results in Fig. 5.30 state that, above the cutoff frequencies of the beampipe the beampipe modes can be calculated by using EE or MM boundary conditions from MAFIA calculations (Up- and downward-pointing triangles). But theses beam-pipe modes cannot be found by the CEM3Dc analysis anymore, because the CEM3Dc eigenmode solver applies the proper boundary conditions. In addition, the different boundary conditions, mesh types and applied geometry models result in the different f and R/Q of the dipole modes in Fig. 5.30.

Secondly, the R/Q of the calculated dipole modes up to 9.9 GHz in the third harmonic superconducting cavity (3.9 GHz), by using CST MWS based on real-valued FIT analysis as well as CEM3Dc analysis, is graphically presented in Fig. 5.31 [6]. At this time the third harmonic cavity is made up of a 9-cell cavity without HOM couplers and the input coupler. EE and MM boundary conditions are applied to the both beam pipes for CST MWS calculations, while port boundary conditions are used to model the infinite beam tubes for CEM3Dc calculations.

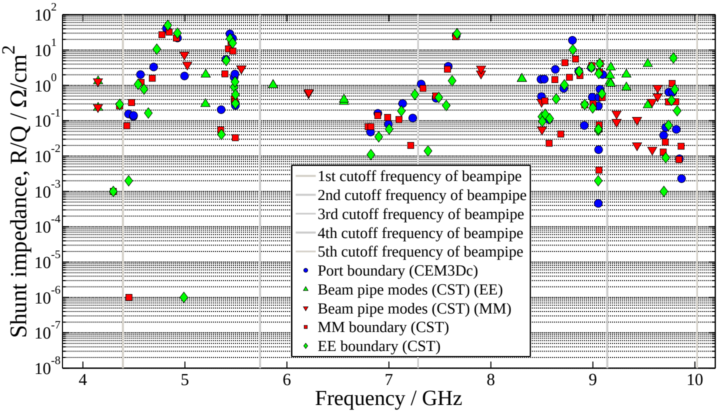

Figure 5.31: The parameter R/Q of the dipole modes calculated for the third harmonic superconducting cavity (3.9 GHz) plotted versus the frequency of the modes. The red squares and downward-pointing triangles denote the modes obtained with MM boundary conditions from the CST MWS calculations while the green diamonds and upward-pointing triangles correspond to modes obtained with EE boundary conditions from the CST MWS calculations [6]. The results obtained with port boundary conditions from CEM3Dc calculations are marked by blue circles.

The results in Fig. 5.31 show that the R/Q of dipole modes obtained with port boundary conditions from CEM3Dc calculations differ from those calculated with CST MWS calculations due to the different boundary conditions and mesh types.

For example, in the band 8.4 to 9.2 GHz the R/Q of the most modes obtained from CEM3Dc calculations are larger than those from CST MWS calculations. In addition some beam pipe modes (the up- and downward pointing triangles in frequency range between 5.8 and 6.6 GHz) obtained from CST MWS calculations cannot be found by CEM3Dc analysis anymore.

To get the knowledge of the influence of boundary conditions at the beam tubes, we compare the calculated HOM modes above the cutoff frequency of the beam tubes from CEM3Dc eigenmode solver by using different boundary conditions at the beam tubes (Fig. 5.32). Because of the port boundary condition, the Q-values of the eigenmodes can be computed properly. Therefore, the quality factors and the shunt impedances R computed by using different boundary conditions at the beam tubes are compared. According to (2.25), the integration path of the electric field should be chosen carefully in order to calculate the shunt impedance for different boundary conditions properly. As already stated before, above the cut-off frequency of the beam pipes, the eigenmodes in the cavity can pass through the beam pipes. For this reason, the integration path for the port boundary conditions is different from that for the idealized PEC and PMC boundary conditions. In this thesis, the length of integration path for all boundary conditions is equal to the length of the cavity. The beam pipes are not taken into account for the integration path in (2.25).

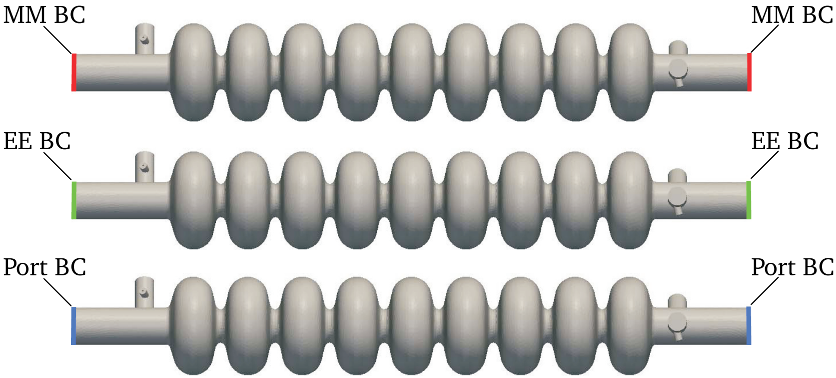

Figure 5.32: TESLA 9-cell 1.3 GHz superconducting RF cavity with beam tubes using perfect electric boundary condition (EE BC), perfect magnetic boundary condition (MM BC) and port boundary condition (Port BC). Main input and HOM couplers always modeled using port BC.

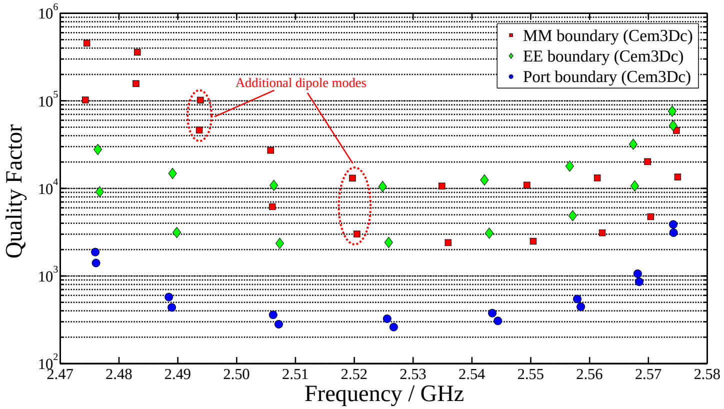

(a) Quality factor

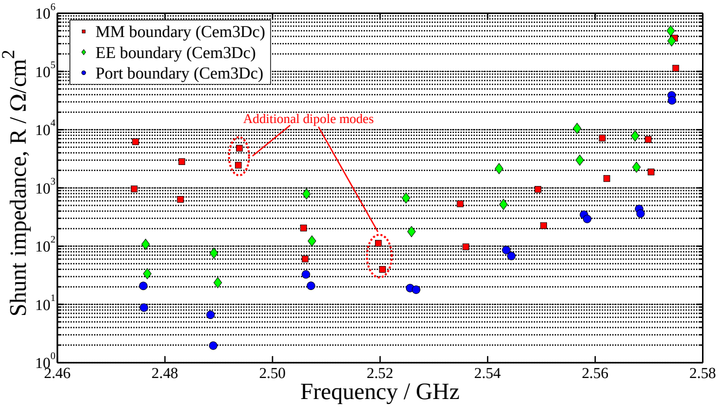

(b) Shunt impedance

Figure 5.33: The parameter quality factor (a) and shunt impedances R (b) of the dipole modes in 3rd dipole passband calculated for TESLA 1.3 GHz cavity plotted versus the frequency of the modes. The red squares denote the modes obtained with MM boundary conditions at both beam tubes from the CEM3Dc calculations while the green diamonds correspond to dipole modes obtained with EE boundary conditions at both beam tubes from the CEM3Dc calculations. The results obtained with port boundary conditions from CEM3Dc calculations are marked by blue circles. Main input and HOM couplers always modeled using port boundary conditions.

First of all, the dipole modes of 3rd dipole passband in the TESLA 1.3 GHz cavity are calculated with different boundary conditions by using CEM3Dc eigenmode solver. The main input and HOM couplers are always modeled using port boundary conditions, whereas the perfect electric (EE), perfect magnetic (MM) and port boundary condition are applied at both beam tubes, respectively.

A graphical representation of Q-values for all calculated dipole modes is given in Fig. 5.33, while the calculated results of shunt impedance R are plotted in Fig. 5.33a. The results in Fig. 5.33a indicate the smaller Q-values calculated by using port boundary conditions in comparison with those calculated by using EE and MM boundary conditions. The reason for that is that port boundary conditions can properly describe the coupling of the modes above the beam pipe cutoff frequency to the beam pipe [47]. As stated in section 2.3, the smaller Q-values lead to smaller shunt impedances R of the eigenmodes as illustrated in Fig. 5.33b. In addition, there are four additional dipole modes for the MM boundary condition as shown in Fig. 5.33. The corresponding field patterns are not identical with those of the modes calculated with EE or port boundary conditions.

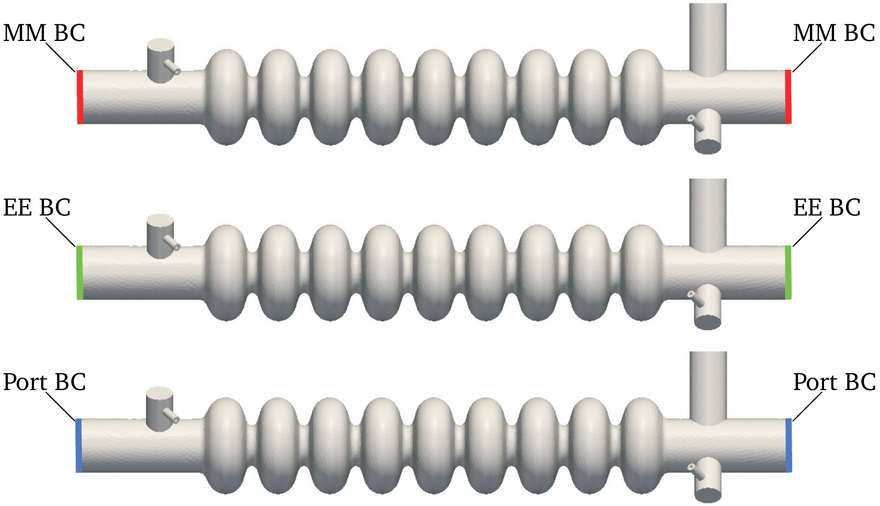

Figure 5.34: The third harmonic superconducting cavity (3.9 GHz) with beam tubes using perfect electric boundary condition (EE BC), perfect magnetic boundary condition (MM BC) and port boundary condition (Port BC). Main input and HOM couplers always modeled using port BC.

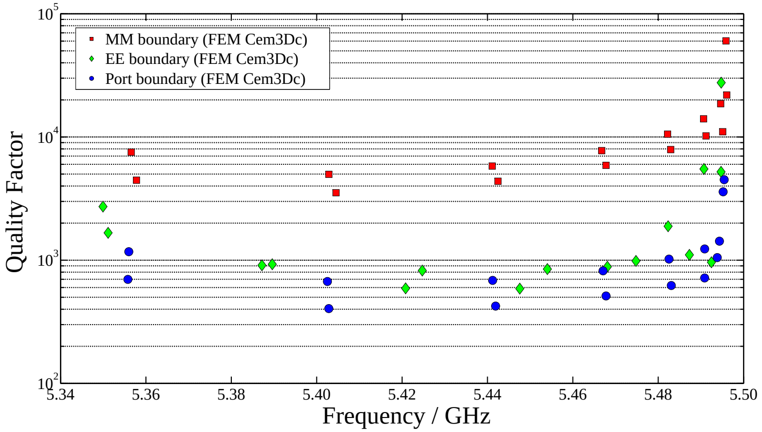

(a) Quality factor

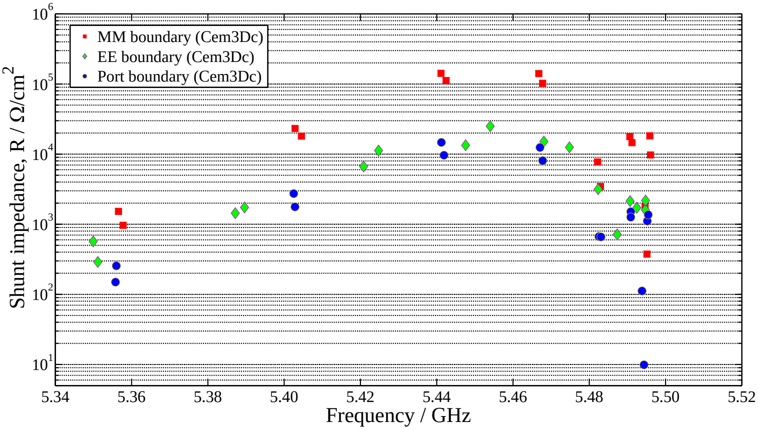

(b) Shunt impedance

Figure 5.35: The quality factor (a) and shunt impedances R (b) of the dipole modes in the 2nd dipole passband calculated for the third harmonic superconducting cavity (3.9 GHz) plotted versus the frequency of the modes. The red squares denote the modes obtained with MM boundary conditions at both beam tubes from the CEM3Dc calculations while the green diamonds correspond to dipole modes obtained with EE boundary conditions at both beam tubes from the CEM3Dc calculations. The results obtained with port boundary conditions from CEM3Dc calculations are marked by blue circles. Main input and HOM couplers always modeled using port boundary conditions.

Similarly, the dipole modes of the 2nd dipole passband for the third harmonic superconducting cavity (3.9 GHz) are calculated with different boundary conditions by using CEM3Dc eigenmode solver. For this case the third harmonic superconducting cavity is composed of a perfect conductive 9-cell cavity, the input coupler as well as the up- and downstream HOM couplers (Fig. 5.34). The main input and HOM couplers are always modeled using port boundary conditions, whereas the perfect electric (EE), perfect magnetic (MM) and port boundary condition are applied at both beam tubes, respectively (Fig. 5.34).

A graphical representation of Q-values for all calculated dipole modes is given in Fig. 5.35a, while the calculated results of shunt impedance R are plotted in Fig. 5.35b. The comparisons from Fig. 5.35 indicate the same outcome as that from the TESLA 1.3 GHz cavity. The Q-values and R calculated with port boundary conditions are smaller than those calculated with EE and MM boundary conditions, since port boundary condition enable the correct treatment of the interactions between the eigenmodes above the beam pipe cutoff frequency and the beam pipes [47].

In brief, the results in Fig. 5.33 and Fig. 5.35 show that, various boundary conditions at the beam tubes can lead to different calculated characteristic values (frequency, quality factor and shunt impedance) of the eigenmodes. Above the cut-off frequency of the beam pipes, the smaller Q-values of the eigenmodes can be obtained with the port boundary conditions. Then, the shunt impedances R of the eigenmodes can be achieved according to (2.37). Due to the smaller Q-values, the shunt impedances R calculated by using port boundary conditions are smaller than those calculated by using EE or MM boundary conditions. This means that, the wake amplitudes excited by those dipole modes obtained with port boundary conditions are lower than those obtained with idealized (PEC and PMC) boundary conditions. The Fig. 5.33 and Fig. 5.35 indicate that the port boundary condition is able to properly formulate the necessary energy exchange in the port plane of the beam pipes.

6 Summary and Outlook

6.1 Summary

The impedance is an important characteristic value, which can affect the stability of the particle beam in the accelerator. Therefore, it should be studied properly during the design phase of the accelerator. For a accelerator composed of the resonant cavities and the corresponding components (beam pipes and couplers), the narrow-band impedances refer to the shunt impedances of the eigenmodes in the resonant cavities, while the broadband impedances, which forms a broad and smooth spectrum, describes the interaction of the particle beam in the accelerating components with their environment. With the broadband- together with narrow-band impedances, the electromagnetic interaction between the particle beam and the accelerators can be described completely in a very wide frequency range.

In this thesis, a dedicated numerical solver based on the Finite Element Method (FEM) has been developed to calculate the broadband impedance for given accelerating components. Afterwards, the narrow-band impedances in the acceleration resonators have been computed with various numerical techniques.

Firstly, a 3D numerical solver based on the Finite Element Method (FEM) has been developed to compute the longitudinal low frequency impedance in frequency domain for particular accelerating components. The major challenge during the code development is given by the proper formulation of the boundary conditions. For this purpose, a 2D FEM solver has been implemented. To develop the 2D and 3D FEM solvers, the Helmholtz split together with the lowest order scalar and vectorial basis functions are used. Due to the inevitable numerical errors occurring in the evaluation of the formulation for the boundary conditions as well as the improper match between the triangles on both boundary planes of the beam pipe and the long homogeneous tetrahedrons in the beam pipe, the developed 3D FEM solver is not applicable to determine the broadband impedances in accelerating components.

Secondly, various accelerator components haven been analyzed via an employment of different numerical approaches to calculate the shunt impedances of the eigenmodes. Specifically, hundreds of eigenmodes in the Superconducting Proton Linac (SPL) cavity, the TESLA 1.3 GHz accelerating cavity as well as the third harmonic 3.9 GHz superconducting cavity have been numerically calculated. Based on the obtained characteristic values of the eigenmodes, those cavities together with the corresponding attached components, e.g. the input and HOM couplers, can be designed properly. The numerical simulations have been performed by frequency-domain eigenmode solvers, which are based on the Finite Integration Technique (FIT) with hexahedral elements and the Finite Element Method (FEM) with higher-order curvilinear elements.

In chapter 5, the numerical simulations with the perfect electric boundary condition have been performed in frequency domain for the SPL cavity by the use of the eigenmode solver based on the Finite Integration Technique (FIT) contained in CST Microwave Studio®. As a result, the eigenfrequencies together with the shunt impedances can be derived. Afterwards, a parallel real-valued CEM3Dr eigenmode solver based on the Finite Element Method (FEM) with higher-order curvilinear elements on symmetric meshes has been applied to the SPL cavity. Hereby, the perfect electric boundary condition has been used to define the structure. The application of symmetric higher-order curvilinear elements cannot only increase the demand for high precision modeling of the elliptical cavity but suppresses also the artificial transverse electric field oscillations efficiently. The obtained numerical results have been compared to the FIT simulations. The comparison indicates, that the CEM3Dr eigenmode solver convergences faster than the FIT eigenmode solver. On the other hand, under precise consideration of the coupler structure a complex-valued CEM3Dc eigenmode solver based on the Finite Element Method (FEM) with higher-order curvilinear elements has been applied to the TESLA 1.3 GHz and the third harmonic 3.9 GHz superconducting cavity to compute the eigenfrequencies, quality factor and the shunt impedances of the eigenmodes. At this time, the port boundary conditions, which can describe the energy transfer between the cavity and its waveguides, e.g. input couplers, HOM couplers and beam pipes, are applied. The CEM3Dc solver is able to deal with higher mesh resolution by using the distributed memory architecture with Message Passing Interface (MPI) parallelization strategy in order to achieve a good performance with respect to simulation time. After that, the electromagnetic field inside the cavity can be smoothed on a physically motivated basis using Kirchhoff's integral theorem in order to calculate the shunt impedance of the eigenmodes with higher precision. To ensure the validity and the high precision of the CEM3Dc eigenmode solver, the obtained results are compared with the other results, which were determined either by the solver contained in MAFIA or the eigenmode solver contained in CST Microwave Studio® as well as the CEM3Dr eigenmode solver with perfect electric and magnetic boundary condition at the both beam pipes. Hereby, the comparisons show that the complex-valued eigenmode solver enable the correct treatment of the interactions between the eigenmodes and the dedicated input coupler, HOM couplers as well as the beam pipes. For post-processing of the simulation results, a dedicated algorithm, which enable the automatic identification of the eigenmode type in a batch mode operation, has been developed. Moreover, the quality factor of the eigenmodes can be computed properly with the visualization and post-processing software ParaView. Finally, the sensitivity of the eigenmodes according to geometrical changes of the TESLA cavity has been analyzed. Hereby, the findings imply that the eigenmodes with higher quality factors and large shunt impedances are sensitive to undesired changes of the cavity shape. To preserve the stability of the particle beam, the geometrical modifications must minimized. In conclusion, the available eigenmode solvers based on FIT and FEM techniques are able to accurately compute the narrow-band impedances (shunt impedances) of the eigenmodes in the acceleration resonators, while parallel implementations of eigenmode solvers can save much computational time. Finally, the results indicate that these numerical approaches are applicable to different accelerating components and they are accurate and reliable tools for supporting the design of accelerators.

6.2 Outlook

Although the thesis already provides applicable and valid approaches for the accurate determination of shunt impedances in the acceleration resonators, there are several ideas or applications for future work available.

In order to determinate the broadband impedance in the accelerating components correctly, we could utilize higher-order basis functions on tetrahedral elements to develop the 3D FEM solver. In this way, the proposed Helmholtz split is not required, such that the observed numerical problems can be avoided. Additionally, a distributed memory architecture by using MPI parallelization strategy can be utilized for the implementation to achieve a good computational performance.

Also, as future application work, the complex-valued FEM eigenmode solver (CEM3Dc) could be applied to an entire TESLA module with eight 1.3 GHz accelerating cavities to determine the narrow-band impedance (shunt impedance) of the occurring eigenmodes.

Appendix A

Hardware Information of the computer clusters TEMFCL2000

	TEMFCL2000
System	Windows Server 2008 R2 HPC
Size	172 Nodes
Node	12 cores
	24 GB of RAM memory
Core	Intel Xeon X5650 3.0 GHz
Network	QDR-Infiniband-Lanes

Table A.1: Hardware information for the computer clusters TEMFCL2000, which are owned by the Computational Electromagnetics Laboratory (TEMF) at Technical University (TU) of Darmstadt.

Appendix B

Geometrical Parameters of the cell of the SPL, TESLA 1.3 GHz, and third harmonic 3.9 GHz cavity.

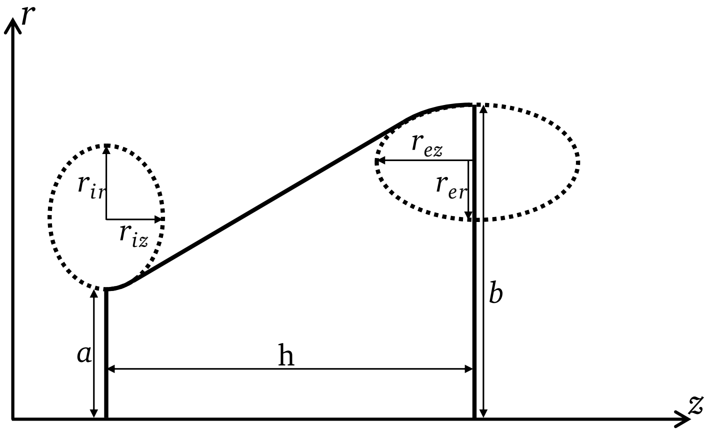

Figure B.1: Parameter definition and geometry modification of a cavity cell.

Superconducting Proton Linac (SPL) Cavity

	mid-cell	end-cell 1	end-cell 2 (Coupler)
Iris radius a / mm	64.6	65	70
Equator radius b / mm	190.786	190.786	190.786
Half cell length h / mm	106.47	103.07	103.07
Equator horizontal axis, r_{ez} / mm	77.5	74.45	74.45
Equator vertical axis, r_{er}	77.5	83.27	76.89
Iris horizontal axis, r_{iz} / mm	22.1	18.5	18.5
Iris vertical axis, r_{ir} / mm	35.1	24.9	24.9

Table B.1: Geometric parameter of the cell of a SPL cavity.

TESLA 1.3 GHz Accelerating Cavity

	mid-cell	end-cell 1	end-cell 2
Iris radius a / mm	35.0	39.0	39.0
Equator radius b / mm	103.3	103.3	103.3
Half cell length h / mm	57.65	55.71	56.85
Equator horizontal axis, r_{ez} / mm	42.19	40.49	42.19
Equator vertical axis, r_{er}	42.19	40.49	42.19
Iris horizontal axis, r_{iz} / mm	12.0	10.0	9.0
Iris vertical axis, r_{ir} / mm	19.0	13.5	12.8

Table B.2: Geometric parameter of the cell of a TESLA 1.3 GHz cavity.

Third Harmonic 3.9GHz Superconducting Cavity

	mid-cell	end-cell 1	end-cell 2
Iris radius a / mm	15.0	20.0	20.0
Equator radius b / mm	35.787	35.787	35.787
Half cell length h / mm	19.2167	19.2167	19.2167
Equator horizontal axis, r_{ez} / mm	13.6	14.4	14.4
Equator vertical axis, r_{er}	15.0	15.0	15.0
Iris horizontal axis, r_{iz} / mm	4.5	4.5	4.5
Iris vertical axis, r_{ir} / mm	6.0	6.0	6.0

Table B.3: Geometric parameter of the cell of a third harmonic 3.9 GHz cavity.

List of Figures

Acronyms and Symbols

Acronyms

2D	Two Dimensional
3D	Three Dimensional
CEM	Computational Electromagnetics
CEM3D	Computational Electromagnetics 3D solver
CEM3Dc	Computational Electromagnetics 3D solver complex-valued
CEM3Dr	Computational Electromagnetics 3D solver real-valued
CERN	European Organization for Nuclear Research
CST MWS	CST Microwave Studio®
DESY	German Electron Synchrotron (German: Deutsches Elektronen-Synchrotron)
DRAM	Dynamic Random-access Memory
EE	Perfect Electric Conductive Boundary Conditions at the both beam pipes
FD	Frequency Domain
FDTD	Finite Difference Time Domain
FEM	Finite Element Method
FIT	Finite Integration Technique
MAFIA	MAFIA™ Software Package
MGE	Maxwell's Grid Equations
MM	Perfect Magnetic Conductive Boundary Conditions at the both beam pipes

MPI	Message Passing Interface
PBA	Perfect Boundary Approximation
PEC	Perfect Electric Conductive
PMC	Perfect Magnetic Conductive
RF	Radio Frequency
SPL	Superconducting Proton Linac
TD	Time Domain
TEMF	Computational Electromagnetics Laboratory

Roman and Greek Letters

$\mathbf{A}$	System matrix	
$\mathbf{A}$, A	Area in $\mathbb{R}^3$	
$\hat{A}$	2D scalar valued curl-operator	
A_{ij}, $\boldsymbol{A}$	FEM stiffness matrix	
$A(i,\ j,\ k)$	Primary elementary surfaces	
$\widetilde{A}(i,j,k)$	Dual elementary surfaces	
a	Geometrical parameter of cavity cell: iris radius	mm
a	Radius of the particle beam	
a	Unknown coefficient	
$\mathbf{a}$	Vector	
a_j	Unknown coefficient	
a_i	Parameter coefficient	
$\mathbf{B}$, $\underline{\mathbf{B}}$	Magnetic flux density and complex amplitude	T
$\hat{B}$	2D vector valued curl-operator	
B_{ij}, $\boldsymbol{B}$	FEM mass matrix	
$B_{\epsilon,ij}$, $\boldsymbol{B}_{\epsilon}$	Boundary term	
b	Geometrical parameter of cavity cell: equator radius	mm
b	Source function	
b	Unknown coefficient	
b	Radius of a cylindrical beam pipe	
$\mathbf{b}$	Vector	

b_i	Parameter coefficient	
b_i, $\boldsymbol{b}$	Source vector	
$\hat{\hat{\mathbf{b}}}$, $\underline{\hat{\hat{\mathbf{b}}}}$	Vector collecting the discrete magnetic fluxes and complex amplitude	
$\hat{\hat{b}}(i,j,k)$	Discrete magnetic flux density	
c	Unknown coefficient	
$\mathbf{C}$, $\tilde{\mathbf{C}}$	Discrete curl operator for primary and dual grid	
$\boldsymbol{c}$	Weighting coefficient vector	
c_0	Speed of the light	m/s
c_i	Parameter coefficient	
c_i	Weighting coefficient	
$\mathbf{D}$, $\underline{\mathbf{D}}$	Electric flux density and complex amplitude	$\mathrm{C/m^2}$
d_i	Parameter coefficient	
d_i	Weighting coefficient	
dA, $d\mathbf{A}$	Infinitesimal area element, scalar and oriented	
ds, $d\mathbf{s}$	Infinitesimal path element, scalar and oriented	
dV	Infinitesimal volume element	
$\boldsymbol{d}$	Weighting coefficient vector	
$\hat{\hat{\mathbf{d}}}$, $\underline{\hat{\hat{\mathbf{d}}}}$	Vector collecting the discrete electric fluxes and complex amplitude	
E	Total number of edges	
$\mathbf{E}$, $\underline{\mathbf{E}}$	Electric field strength and complex amplitude	V/m
$\mathbf{E}_\perp$	Transversal component of the electric field	
$\mathrm{E_z}$	Longitudinal component of the electric field	
$\boldsymbol{e}$	Solution vector	
$\boldsymbol{e}_x$	x-coordinate in Cartesian coordinate system	m
$\boldsymbol{e}_y$	y-coordinate in Cartesian coordinate system	m
$\boldsymbol{e}_z$	z-coordinate in Cartesian and cylinder coordinate system	m
$\hat{\mathbf{e}}$, $\underline{\hat{\mathbf{e}}}$	Vector collecting the discrete electric voltages and complex amplitude	
$\hat{e}(i,j,k)$	Discrete electric voltage	
F	Operator	
F	Total number of facets	
f_s	Function	
f	Frequency	Hz
G	Primary grid	
$\tilde{G}$	Dual grid	
g	Function	
$\mathbf{H}$, $\underline{\mathbf{H}}$	Magnetic field strength and complex amplitude	A/m
h	Geometrical parameter of cavity cell: half cell length	mm
h	Function	

$\widehat{\mathbf{h}}$, $\underline{\widehat{\mathbf{h}}}$	Vector collecting the discrete magnetic voltages and complex amplitude	
I_0	The 0 order modified Bessel functions of first kind	
I_1	The 1 order modified Bessel functions of first kind	
$\hat{\mathrm{I}}$	Unit matrix of size 2	
$i,\ l,\ k\ m\ n$	indices	
$\mathbf{J}$, $\underline{\mathbf{J}}$	Current density and complex amplitude	$\mathrm{A/m^2}$
$\mathbf{J}_F$	Surface current density	
$J_{2D},\ J_{3D}$	Jacobian matrix	
$\widehat{\widehat{\mathbf{j}}}$	Vector collecting the currents	
K_0	The 0 order modified Bessel functions of second kind	
K_1	The 1 order modified Bessel functions of second kind	
k	Wavenumber	$\mathrm{m^{-1}}$
k_n	Loss parameter	
L	Operator	
$L(i,\ j,\ k)$	Primary elementary edges	
$\widetilde{L}(i,j,k)$	Dual elementary edges	
$\mathbf{M}_\epsilon$	Permittivity matrix	
$\mathbf{M}_\mu$	Permeability matrix	
$\mathbf{M}_\kappa$	Conductivity matrix	
$M_{ij},\ \boldsymbol{M}$	FEM mass matrix	
N	Total number of nodes	
$N_i,\ \widehat{N}_i$	Nodal function	
n	Positive integer	
$\mathbf{n}$	Unit normal vector	
P	Total power loss	W
p	Generic point in three dimensional space	
$P(i,\ j,\ k)$	Primary elementary points	
$\widetilde{P}(i,j,k)$	Dual elementary points	
Q	Quality factor	
q	Electric charge	
$\mathbf{q}$	Vector collecting the electric charges	
R	Residual	
R	Shunt impedance	
R	Distance	m
R/Q	Normalized shunt impedance	
$\mathbf{R}$	Source term	
R_{sur}	Surface resistivity	Ω
$\mathbf{r}$	Position vector in $\mathbb{R}^3$	m
r	r-coordinate in cylinder coordinate system	m
r1	Geometrical parameter of cavity cell: iris radius	mm
r2	Geometrical parameter of cavity cell: equator radius	mm

r_{er}, ry2	Geometrical parameter of cavity cell: equator vertical axis	mm
r_{ez}, rx2	Geometrical parameter of cavity cell: equator horizontal axis	mm
r_{ir}, ry1	Geometrical parameter of cavity cell: iris vertical axis	mm
r_{iz}, rx1	Geometrical parameter of cavity cell: iris horizontal axis	mm
$\mathbf{S}$	Poynting vector	$\mathrm{W/m^2}$
$\mathbf{S}$, $\widetilde{\mathbf{S}}$	Discrete divergence operator for primary and dual grid	
S_{ij}, $\boldsymbol{S}$	FEM stiffness matrix	
T	Total number of tetrahedrons	
T	Unknown function	
$\widetilde{T}$	Approximation solution	
t	Time	s
$\mathbf{t}$	Unit tangential vector	
U	Stored energy	J
U_n	Energy unit	J
$\triangle U_n$	Dissipated energy per cycle	J
u	Unknown function	
u_i	Weighting residual	
$\boldsymbol{u}$	Function	
u_1	u_1-coordinate in Cartesian coordinate system	m
u_2	u_2-coordinate in Cartesian coordinate system	m
u_3	u_3-coordinate in Cartesian coordinate system	m
V	Volume in $\mathbb{R}^3$	
V	Primary elementary volumes	
V	Voltage	V
$\widetilde{V}$	Dual elementary volumes	
$\boldsymbol{W}$	Wake potential	V
$\boldsymbol{W}_{\|\|}$	Longitudinal wake potential	V
$\boldsymbol{W}_{\perp}$	Transverse wake potential	V
$\boldsymbol{w}_i$, $\widehat{\boldsymbol{w}}_i$	Nédélec edge function	
$\boldsymbol{w}_j$	Basis function	
xlen2	Geometrical parameter of cavity cell: half cell length	mm
x	Generic point of the domain Ω	
x	x-coordinate in Cartesian coordinate system	m
y	y-coordinate in Cartesian coordinate system	m
Z, $\underline{Z}$	Impedance	Ω
z	z-coordinate in Cartesian and cylinder coordinate system	m
$\hat{Z}$	Hodge operator	
α	Weighting coefficient	
$\boldsymbol{\alpha}$	Weighting coefficient vector	
β	Relativistic velocity	
γ	Lorentz factor	

ϵ	Permittivity	As/Vm
ϵ_r	Relative permittivity	As/Vm
ϵ_0	Permittivity of vacuum	As/Vm
κ	Electric conductivity	S/m
μ	Permeability	Vs/Am
μ_r	Relative permeability	Vs/Am
μ_0	Permeability of vacuum	Vs/Am
ρ	Electric charge density	$\mathrm{C/m^3}$
σ	Surface charge density	
$\boldsymbol{\upsilon}$	Velocity	m/s
φ	φ-coordinate in cylinder coordinate system	
ϱ	ϱ-coordinate in cylinder coordinate system	
ψ	Function	
ω	Angular frequency	$\mathrm{s^{-1}}$
Ω	Spatial domain	
Φ ,$\underline{\Phi}$, $\underline{\Psi}$	Electric potential and complex amplitude	V

General Mathematical Symbols

$\mathbb{R}$	Real numbers
$*$	Complex conjugate of a complex number
T	Transpose operator of a matrix
$\jmath$	Imaginary unit
δ	Dirac distribution
δ	δ function distribution
Θ	Heaviside step function
∇	Nabla operator
∂	Partial derivative operator

Bibliography

[1] D. Davidson, *Computational Electromagnetics for RF and Microwave Engineering*. Cambridge University Press, 2010. (Cited on page 1.)

[2] M. Baylac, F. Gerigk, E. Benedico Mora, F. Caspers, S. Chel, J. De Conto, R. Duperrier, E. Froidefond, R. Garoby, K. Hanke, C. Hill, M. Hori, J. Inigo-Golfin, K. Kahle, T. Kroyer, D. Küchler, J. B. Lallement, M. Lindroos, A. M. Lombardi, A. López Hernández, M. Magistris, T. K. Meinschad, A. Millich, E. Noah Messomo, C. Pagani, V. Palladino, M. Paoluzzi, M. Pasini, P. Pierini, C. Rossi, J. P. Royer, M. Sanmartí, E. Sargsyan, R. Scrivens, M. Silari, T. Steiner, J. Tückmantel, D. Uriot, and M. Vretenar, "Conceptual design of the SPL II: A high-power superconducting H- linac at CERN," research report, - , 2006. LPSc-acc. (Cited on page 1.)

[3] B. Aune, R. Bandelmann, D. Bloess, B. Bonin, A. Bosotti, M. Champion, C. Crawford, G. Deppe, B. Dwersteg, D. A. Edwards, H. T. Edwards, M. Ferrario, M. Fouaidy, P.-D. Gall, A. Gamp, A. Gössel, J. Graber, D. Hubert, M. Hüning, M. Juillard, T. Junquera, H. Kaiser, G. Kreps, M. Kuchnir, R. Lange, M. Leenen, M. Liepe, L. Lilje, A. Matheisen, W.-D. Möller, A. Mosnier, H. Padamsee, C. Pagani, M. Pekeler, H.-B. Peters, O. Peters, D. Proch, K. Rehlich, D. Reschke, H. Safa, T. Schilcher, P. Schmüser, J. Sekutowicz, S. Simrock, W. Singer, M. Tigner, D. Trines, K. Twarowski, G. Weichert, J. Weisend, J. Wojtkiewicz, S. Wolff, and K. Zapfe, "Superconducting tesla cavities," *Phys. Rev. ST Accel. Beams*, vol. 3, p. 092001, Sep 2000. (Cited on pages 2 and 104.)

[4] M. Altarelli, R. Brinkmann, M. Chergui, W. Decking, B. Dobson, S. Dusterer, G. Grubel, W. Graeff, H. Graafsma, J. Hajdu, J. Marangos, J. Pfluger, H. Redlin, D. Riley, I. Robinson, J. Rossbach, A. Schwarz, K. Tiedtke, T. Tschentscher, I. Vartaniants, H. Wabnitz, H. Weise, R. Wichmann, K. Witte, A. Wolf, M. Wulff, and M. Yurkov, *XFEL: The European X-Ray Free-Electron Laser : Technical design report*. Hamburg: DESY, 2006. (Cited on page 3.)

[5] S. Schreiber, B. Faatz, J. Feldhaus, K. Honkavaara, R. Treusch, M. Vogt, *et al.*, "Status of the fel user facility flash," in *Proceedings of FEL*, vol. 11, 2011. (Cited on page 3.)

[6] P. Zhang, N. Baboi, and R. M. Jones, “Eigenmode simulations of third harmonic superconducting accelerating cavities for flash and the european xfel,” *arXiv preprint arXiv:1206.2782*, 2012. (Cited on pages 3, 91, and 112.)

[7] T. Weiland, “A discretization model for the solution of Maxwell’s equations for six-component fields,” *Archiv Elektronik und Uebertragungstechnik*, vol. 31, pp. 116–120, 1977. (Cited on pages 3 and 17.)

[8] U. van Rienen, *Numerical Methods in Computational Electrodynamics: Linear Systems in Practical Applications*. Lecture Notes in Computational Science and Engineering, Springer Berlin Heidelberg, 2012. (Cited on pages 3 and 18.)

[9] “CST STUDIO SUITE®.” `https://www.cst.com`. CST Computer Simulation Technology AG, Bad Nauheimer Str. 19, Darmstadt, Germany. (Cited on pages 3, 53, 62, 65, 72, 86, and 110.)

[10] J. D. Jackson, *Classical electrodynamics*. New York, NY: Wiley, 3rd ed. ed., 1999. (Cited on page 5.)

[11] S. Schnepp, *Space-Time Adaptive Methods for Beam Dynamics Simulations*. PhD thesis, TU Darmstadt, April 2009. (Cited on page 5.)

[12] R. Becker and F. Sauter, *Einführung in die Maxwellsche Theorie, Elektronentheorie, Relativitätstheorie*. Theorie der Elektrizität / Richard Becker, Teubner, 1957. (Cited on page 6.)

[13] T. Weiland and R. Wanzenberg, “Wake fields and impedances,” p. 54 p, May 1991. (Cited on pages 7, 8, 9, 12, 13, and 17.)

[14] R. Hampel, *A Directionally Dispersion-free Algorithm for the Calculation of Wake Potentials*. PhD thesis, TU Darmstadt, March 2009. (Cited on pages 7, 18, 24, and 104.)

[15] T. Weiland, “Comment on wake field computation in time domain,” *Nuclear Instruments and Methods in Physics Research*, vol. 216, no. 1-2, pp. 31–34, 1983. (Cited on page 8.)

[16] P. Huray, *Maxwell’s Equations*. Wiley, 2011. (Cited on page 9.)

[17] W. F. O. Müller, *Untersuchungen zu Moden höherer Ordnung in konstanten und variierten Beschleunigerstrukturen für zukünftige lineare Kollider*. PhD thesis, Universität Frankfurt am Main, December 2000. (Cited on pages 9 and 12.)

[18] O. D. Jefimenko, “Presenting electromagnetic theory in accordance with the principle of causality,” *European Journal of Physics*, vol. 25, no. 2, p. 287, 2004. (Cited on page 9.)

[19] O. Napoly, Y. H. Chin, and B. Zotter, “A generalized method for calculating wake potentials,” *Nuclear Instruments and Methods in Physics Research Section A: Accelerators, Spectrometers, Detectors and Associated Equipment*, vol. 334, no. 2, pp. 255 – 265, 1993. (Cited on page 9.)

[20] W. K. H. Panofsky and W. A. Wenzel, “Some considerations concerning the transverse deflection of charged particles in radio-frequency fields,” *Review of Scientific Instruments*, vol. 27, no. 11, pp. 967–967, 1956. (Cited on page 9.)

[21] P. Hülsmann, *Theoretische und experimentelle Untersuchungen zur Bestimmung der transversalen Shuntimpedanz und Güte an störmodenbedämpften Beschleunigerresonatoren für lineare Kollider und Hochstrombeschleuniger in mittleren und hohen Energiebereichen*. PhD thesis, Universität Frankfurt am Main, 1992. (Cited on page 9.)

[22] A. W. Chao, *Physics of Collective Beam Instabilities in High Energy Accelerators*. Wiley Series in Beam Physics and Accelerator Technology, Wiley-VCH; 1 edition (January 15, 1993), 1993. (Cited on page 10.)

[23] A. Chao, *Handbook of Accelerator Physics and Engineering*. Handbook of Accelerator Physics and Engineering, World Scientific, 1999. (Cited on page 10.)

[24] S. Heifets, K. Ko, C. Ng, X. Lin, A. Chao, G. Stupakov, M. S. Zolotorev, J. Seeman, U. Wienands, C. Perkins, M. E. Nordby, E. F. Daly, N. R. Kurita, D. Wright, E. Henestroza, G. R. Lambertson, J. Corlett, J. Byrd, M. S. Zisman, T. Weiland, W. Stoeffl, and C. Belser, “Impedance study for the PEP-II B-factory,” p. 90 p, Mar 1995. (Cited on page 10.)

[25] A. W. Chao, “Coherent instabilities of a relativistic bunched beam,” tech. rep., Stanford Linear Accelerator Center, CA (USA), 1982. (Cited on page 10.)

[26] A. M. Al-khateeb, O. Boine-Frankenheim, I. Hofmann, and G. Rumolo, “Analytical calculation of the longitudinal space charge and resistive wall impedances in a smooth cylindrical pipe,” *Phys. Rev. E*, vol. 63, p. 026503, Jan 2001. (Cited on pages 10 and 51.)

[27] U. Niedermayer and O. Boine-Frankenheim, "Analytical and numerical calculations of resistive wall impedances for thin beam pipe structures at low frequencies," *Nuclear Instruments and Methods in Physics Research Section A: Accelerators, Spectrometers, Detectors and Associated Equipment*, vol. 687, pp. 51–61, 2012. (Cited on page 10.)

[28] R. Gluckstern, "Analytic methods for calculating coupling impedances," CERN Accelerator School, 2000. (Cited on pages 11 and 38.)

[29] J. Harlow, *Electric Power Transformer Engineering, Third Edition*. The electric power engineering handbook, CRC Press, 2012. (Cited on page 12.)

[30] H. Padamsee, T. Hays, and J. Knobloch, *RF Superconductivity for Accelerators*. Wiley-VCH; 2nd edition, 2008. (Cited on page 12.)

[31] P. Schmüser, "Basic principles of rf superconductivity and superconducting cavities," 2006. (Cited on pages 13 and 14.)

[32] R. Wanzenberg, "Monopole, dipole and quadrupole passbands of the TESLA 9-cell cavity," Tech. Rep. DESY-TESLA-2001-33, DESY, Hamburg, Sep 2001. (Cited on pages 14, 74, 75, 89, 90, and 111.)

[33] T. Weiland, "Finite integration method and discrete electromagnetism," in *Computational Electromagnetics*, pp. 183–198, Springer, 2003. (Cited on page 17.)

[34] M. C. T. Weiland, "Discrete electromagnetism with the finite integration technique," *Progress In Electromagnetics Research*, vol. 32, pp. 65–87, 2001. (Cited on page 17.)

[35] U. van Rienen and T. Weiland, "Triangular discretization method for the evaluation of rf-fields in cylindrically symmetric cavities," *Magnetics, IEEE Transactions on*, vol. 21, pp. 2317–2320, Nov 1985. (Cited on page 17.)

[36] *Skriptum zum Verfahren und Anwendungen der Feldsimulation*. Technische Universität Darmstadt, 2013. (Cited on pages 17 and 35.)

[37] K. Klopfer, *Computation of Complex Eigenmodes for Resonators Filled With Gyrotropic Materials*. PhD thesis, TU Darmstadt, 2014. (Cited on page 19.)

[38] T. Weiland, "On the numerical solution of Maxwell's equations and applications in the field of accelerator physics," *Part. Accel.*, vol. 15, pp. 245–292. 38 p, Jan 1984. (Cited on pages 19 and 22.)

[39] X. Wang, *Wave Propagation in Liquid-Crystal Materials*. PhD thesis, TU Darmstadt, Darmstadt, April 2014. (Cited on page 19.)

[40] M. Clemens and T. Weiland, “Discrete electromagnetics: Maxwell’s equations tailored to numerical simulations,” *Int. Compumag Soc. Newsletter*, vol. 8, pp. 13–20, 2001. (Cited on page 22.)

[41] T. Weiland, “On the unique numerical solution of Maxwellian eigenvalue problems in three dimensions,” *Part. Accel.*, vol. 17, pp. 227–242. 24 p, Nov 1984. (Cited on page 22.)

[42] R. Harrington, *Time-Harmonic Electromagnetic Fields*. IEEE Press Series on Electromagnetic Wave Theory, Wiley, 2001. (Cited on page 24.)

[43] I. Zagorodnov, R. Schuhmann, and T. Weiland, “A uniformly stable conformal fdtd-method in cartesian grids,” *International Journal of Numerical Modelling: Electronic Networks, Devices and Fields*, vol. 16, no. 2, pp. 127–141, 2003. (Cited on page 25.)

[44] T. Banova, *Systematic Data Extraction in High-Frequency Electromagnetic Fields*. PhD thesis, TU Darmstadt, July 2014. (Cited on pages 25, 29, 35, and 42.)

[45] J. Jian Ming, “Finite element method in electromagnetics,” 2002. (Cited on pages 26, 28, and 51.)

[46] *Lecture Notes: Finite Element Method in Electromagnetics*. Technische Universität Darmstadt, 2011. (Cited on pages 27, 29, 32, and 34.)

[47] W. Ackermann, T. Weiland, *et al.*, “High precision cavity simulations,” *MOADI1*, 2012. (Cited on pages 28, 33, 35, 53, 71, 72, 73, 94, and 96.)

[48] J. L. Volakis, A. Chatterjee, and L. C. Kempel, *Finite element method electromagnetics: antennas, microwave circuits, and scattering applications*, vol. 6. John Wiley & Sons, 1998. (Cited on pages 29 and 38.)

[49] A. Logg, K.-A. Mardal, and G. N. Wells, eds., *Automated Solution of Differential Equations by the Finite Element Method*, vol. 84 of *Lecture Notes in Computational Science and Engineering*. Springer, 2012. (Cited on pages 31 and 42.)

[50] H. Rathod and S. Kilari, “General complete lagrange family for the cube in finite element interpolations,” *Computer Methods in Applied Mechanics and Engineering*, vol. 181, no. 1-3, pp. 295 – 344, 2000. (Cited on page 31.)

[51] D. B. Davidson, "An evaluation of mixed-order versus full-order vector finite elements," *Antennas and Propagation, IEEE Transactions on*, vol. 51, no. 9, pp. 2430–2441, 2003. (Cited on pages 32 and 42.)

[52] R. Abdul-Rahman and M. Kasper, "Orthogonal hierarchical nédélec elements," *Magnetics, IEEE Transactions on*, vol. 44, no. 6, pp. 1210–1213, 2008. (Cited on pages 32 and 42.)

[53] J.-C. Nédélec, "Mixed finite elements in $\mathbb{R}^3$," *Numerische Mathematik*, vol. 35, no. 3, pp. 315–341, 1980. (Cited on pages 33 and 39.)

[54] A. Schneebeli, "An H (curl; Ω)-conforming FEM: Nédélec's element of the first type, tech," 2003. (Cited on pages 33 and 49.)

[55] W. Ackermann, G. Benderskaya, and T. Weiland, "State of the art in the simulation of electromagnetic fields based on large scale finite element eigenanalysis," *International COMPUMAG Society Newsletter*, no. 17(2), pp. 3–12, 2010. (Cited on pages 33, 43, 64, 65, 66, 67, 72, 107, and 108.)

[56] M. N. Sadiku, *Numerical techniques in electromagnetics*. CRC press, 2000. (Cited on pages 34, 39, and 45.)

[57] T. Chung, "Finite element analysis in fluid dynamics," *NASA STI/Recon Technical Report A*, vol. 78, p. 44102, 1978. (Cited on page 34.)

[58] A. Ern and J.-L. Guermond, "Evaluation of the condition number in linear systems arising in finite element approximations," *ESAIM: Mathematical Modelling and Numerical Analysis*, vol. 40, no. 01, pp. 29–48, 2006. (Cited on page 35.)

[59] Y. Saad, *Iterative Methods for Sparse Linear Systems*. Philadelphia, PA, USA: Society for Industrial and Applied Mathematics, 2nd ed., 2003. (Cited on page 35.)

[60] G. V. Stupakov, "Wake and impedance," in *AIP CONFERENCE PROCEEDINGS*, pp. 205–230, IOP INSTITUTE OF PHYSICS PUBLISHING LTD, 2001. (Cited on page 37.)

[61] U. Niedermayer and O. Boine-Frankenheim, "Numerical Calculation of Beam Coupling Impedances in the Frequency Domain using FIT," Tech. Rep. EuCARD-CON-2012-017, 2012. (Cited on page 37.)

[62] A. M. Al-khateeb, O. Boine-Frankenheim, R. W. Hasse, and I. Hofmann, “Longitudinal impedance and shielding effectiveness of a resistive beam pipe for arbitrary energy and frequency,” *Physical Review. E, Statistical Physics, Plasmas, Fluids, and Related Interdisciplinary Topics*, vol. 71, no. 2, 2005. (Cited on page 37.)

[63] L. Andersen and J. Volakis, “Hierarchical tangential vector finite elements for tetrahedra,” *Microwave and Guided Wave Letters, IEEE*, vol. 8, pp. 127–129, Mar 1998. (Cited on page 39.)

[64] I. Tsukerman, “Symbolic algebra as a tool for understanding edge elements,” *Magnetics, IEEE Transactions on*, vol. 39, pp. 1111–1114, May 2003. (Cited on page 39.)

[65] J. Webb and B. Forgahani, “Hierarchal scalar and vector tetrahedra,” *Magnetics, IEEE Transactions on*, vol. 29, pp. 1495–1498, Mar 1993. (Cited on page 39.)

[66] L. Zhong, S. Shu, G. Wittum, and J. Xu, “Optimal error estimates for Nedelec edge elements for time-harmonic Maxwell’s equations,” *J. Comput. Math*, vol. 27, no. 5, pp. 563–572, 2009. (Cited on page 39.)

[67] G. B. Arfken and H. J. Weber, *Mathematical Methods for Physicists*. Academic Press, 2013. (Cited on pages 39 and 45.)

[68] A. Dziekonski, P. Sypek, A. Lamecki, and M. Mrozowski, “Finite element matrix generation on a GPU,” *Progress In Electromagnetics Research*, vol. 128, pp. 249–265, 2012. (Cited on pages 40 and 43.)

[69] G. H. Golub and J. H. Welsch, “Calculation of Gauss quadrature rules,” *Mathematics of Computation*, vol. 23, no. 106, pp. 221–230, 1969. (Cited on pages 40 and 47.)

[70] F.-J. Sayas, “A gentle introduction to the finite element method,” (Cited on pages 40, 43, 47, and 50.)

[71] T. Rahman and J. Valdman, “Fast MATLAB assembly of FEM matrices in 2d and 3d: Nodal elements,” *Applied Mathematics and Computation*, vol. 219, no. 13, pp. 7151 – 7158, 2013. {ESCO} 2010 Conference in Pilsen, June 21-25, 2010. (Cited on pages 41 and 47.)

[72] M. E. Rognes, R. C. Kirby, and A. Logg, “Efficient assembly of H(div) and H(curl) conforming finite elements,” *SIAM Journal on Scientific Computing*, vol. 31, no. 6, pp. 4130–4151, 2009. (Cited on pages 41, 43, 47, and 50.)

[73] D. Jerison and C. E. Kenig, “The inhomogeneous dirichlet problem in lipschitz domains,” *Journal of functional analysis*, vol. 130, no. 1, pp. 161–219, 1995. (Cited on page 41.)

[74] V. Ganzha and E. Vorozhtsov, *Numerical Solutions for Partial Differential Equations: Problem Solving Using Mathematica*. Symbolic & Numeric Computation, Taylor & Francis, 1996. (Cited on page 41.)

[75] K. Morgan, “The finite element method in partial differential equations,” *International Journal for Numerical Methods in Engineering*, vol. 11, no. 11, 1977. (Cited on page 41.)

[76] I. N. Bronstein, K. A. Semendjajew, and G. Musiol, *Taschenbuch der Mathematik*. Deutsch (Harri), Aug. 2005. (Cited on page 41.)

[77] I. Anjam and J. Valdman, “Fast MATLAB assembly of FEM matrices in 2d and 3d: Edge elements,” *CoRR*, vol. abs/1409.4618, 2014. (Cited on pages 43 and 50.)

[78] “MATLAB R2014a.” The MathWorks Inc., Natick, MA, 2014. (Cited on pages 43, 53, and 81.)

[79] A. H.-D. Cheng and D. T. Cheng, “Heritage and early history of the boundary element method,” *Engineering Analysis with Boundary Elements*, vol. 29, no. 3, pp. 268 – 302, 2005. (Cited on page 45.)

[80] U. Niedermayer, O. Boine-Frankenheim, and H. De Gersem, “Space charge and resistive wall impedance computation in the frequency domain using the finite element method,” *Phys. Rev. ST Accel. Beams*, vol. 18, p. 032001, Mar 2015. (Cited on page 45.)

[81] P. Abbott, “Tricks of the trade,” *Mathematica journal*, no. 8, pp. 516–522, 2002. (Cited on page 47.)

[82] U. Niedermayer, O. Boine-Frankenheim, and O. Boine-Frankenheim, “Beam Coupling Impedance Simulation in the Frequency Domain for the SIS100 Synchrotron,” p. TUPRI045, 2014. (Cited on page 47.)

[83] O. Brunner, S. Calatroni, E. Ciapala, M. Eshraqi, R. Garoby, F. Gerigk, A. Lombardi, R. Losito, V. Parma, C. Rossi, J. Tuckmantel, M. Vretenar, U. Wagner, and W. Weingarten, “Assessment of the basic parameters of the CERN Superconducting Proton Linac,” *Phys. Rev. ST Accel. Beams*, vol. 12, p. 070402, Jul 2009. (Cited on page 61.)

[84] L.-Q. Lee, Z. Li, C. Ng, and K. Ko, “Omega3P: A Parallel Finite-Element Eigenmode Analysis Code for Accelerator Cavities,” 2009. (Cited on page 71.)

[85] R. D. Graglia, A. F. Peterson, and F. P. Andriulli, “Curl-conforming hierarchical vector bases for triangles and tetrahedra,” *IEEE Transactions on Antennas and Propagation*, vol. 59, no. 3, pp. 950–959, 2011. (Cited on page 72.)

[86] P. Ingelstrom, “A new set of H (curl)-conforming hierarchical basis functions for tetrahedral meshes,” *Microwave Theory and Techniques, IEEE Transactions on*, vol. 54, no. 1, pp. 106–114, 2006. (Cited on page 72.)

[87] “ParaView 3.14.1 64 bit.” Kitware Inc.Sandia National Laboratories, New Mexico PO Box 5800 Albuquerque, NM 87185, UNITED STATES. (Cited on pages 79 and 84.)

[88] C. Daniel and F. S. Wood, *Fitting Equations to Data: Computer Analysis of Multifactor Data*. New York, NY, USA: John Wiley & Sons, Inc., 2nd ed., 1999. (Cited on page 81.)

[89] H. J. Pain, *The Physics of Vibrations and Waves*. John Wiley & Sons, Ltd, 2005. (Cited on page 82.)

[90] G. Lehner, “Elektromagnetische Feldtheorie: für Ingenieure und Physiker,” 2006. (Cited on page 83.)

Acknowledgments

At the end of this dissertation, I would like to express my gratitude to everyone, who helped and supported me during my PHD work. Particularly, I would like to thank

- Prof. Dr.-Ing. Thomas Weiland for the scientific supervision and giving me the opportunity to work at the institute.
- Prof. Dr.-Ing. Harald Klingbeil for agreeing to act and reviewing my dissertation as co-referee.
- Prof. Dr.-Ing. Herbert De Gersem for the kindly contributing in the reviewing of manuscript for my dissertation.
- Dr.-Ing. Wolfgang Ackermann for the great scientific guidance and for his carefully reviewing and correcting of manuscripts for the papers and my dissertation.
- Dr. phil. nat. Wolfgang F.O. Müller for the great scientific guidance and for his carefully reviewing and correcting of manuscripts for the papers.
- all my present and former colleagues for the valuable support and providing me the pleasant and friendly atmosphere in the last six years.
- my dear friends, Enchun Xiong, Jiale Yin, Peiqing Li, Xiao Liu, Yi Li, Shihong Zhang and Dong Xue.

At last, I want to express my deep thanks to my parents and my wife Mrs. Yuanyuan Cai for their unconditional support.

Thanks to all of you!

Curriculum Vitae

Personal Data:

Name:	Cong Liu
Date of birth:	09.07.1980
Place of birth:	Shanghai, China

Education

1992 - 1995	Yongji junior middle school in Shanghai, China
1995 - 1998	Anshan senior middle school in Shanghai, China
1998 - 2002	Bachelor in physics, Shanghai University, Shanghai, China Specialisation: Optoelectronics
2003 - 2009	Dipl.-Ing. in Electrical Engineering and Information Technology, University of Bremen, Bremen, Germany Specialisation: Microelectronics and Microsystems Engineering
2010 - 2015	Dr.-Ing. at Computational Electromagnetics Laboratory, Technical University of Darmstadt, Darmstadt, Germany